ANALYSIS OF WACSIS DATA USING A DIRECTIONAL HYBRID WAVE MODEL

A Dissertation

by

SHAOSONG ZHANG

Submitted to the Office of Graduate Studies of
Texas A&M University
in partial fulfillment of the requirements for the degree of

DOCTOR OF PHILOSOPHY

December 2005

Major Subject: Civil Engineering

ANALYSIS OF WACSIS DATA USING A DIRECTIONAL HYBRID WAVE MODEL

A Dissertation

by

SHAOSONG ZHANG

Submitted to the Office of Graduate Studies of
Texas A&M University
in partial fulfillment of the requirements for the degree of

DOCTOR OF PHILOSOPHY

Approved by:

Chair of Committee,	Jun Zhang
Committee Members,	Billy Edge
	Moo-hyun Kim
	Guy Battle
Head of Department,	David V. Rosowsky

December 2005

Major Subject: Civil Engineering

ABSTRACT

Analysis of WACSIS Data Using a Directional

Hybrid Wave Model. (December 2005)

Shaosong Zhang, B.S.; M.S., Tianjin University, China

Chair of Advisory Committee: Dr. Jun Zhang

This study focuses on the analysis of measured directional seas using a nonlinear model, named Directional Hybrid Wave Model (DHWM). The model has the capability of decomposing the directional wave field into its free wave components with different frequency, amplitude, direction and initial phase based on three or more time series of measured wave properties. With the information of free waves, the DHWM can predict wave properties accurately up to the second order in wave steepness. In this study, the DHWM is applied to the analyses of the data of Wave Crest Sensor Inter-comparison Study (WACSIS). The consistency between the measurements collected by different sensors in the WACSIS project was examined to ensure the data quality. The wave characteristics at the locations of selected sensors were predicted in time domain and were compared with those recorded at the same location. The degree of agreement between the predictions and the related measurements is an indicator of the consistency among different sensors.

To analyze the directional seas in the presence of strong current, the original DHWM was extended to consider the Doppler effects of steady and uniform currents on the directional wave field. The advantage of extended DHWM originates from the use of the intrinsic frequency instead of the apparent frequency to determine the corresponding wavenumber and transfer functions relating wave pressure and velocities to elevation.

Furthermore, a new approach is proposed to render the accurate and consistent estimates of the energy spreading parameter and mean wave direction of directional seas based on a cosine-2s model. In this approach, a Maximum Likelihood Method (MLM) is employed. Because it is more tolerant of errors in the estimated cross spectrum than a Directional Fourier Transfer (DFT) used in the conventional approach, the proposed approach is able to estimate the directional spreading parameters more accurately and consistently, which is confirmed by applying the proposed and conventional approach, respectively, to the time series generated by numerical simulation and recorded during the WACSIS project.

ACKNOWLEDGMENTS

I would like to express my gratitude to Dr. Jun Zhang, my advisor, for his continuous encouragement, guidance and support throughout my PhD study. Sincere thanks are expressed to Dr. Billy Edge, Dr. Moo-Hyun Kim and Dr. Guy Battle for serving as my committee members.

I also would like to thank Dr. George Forristall and Dr. Marc Prevosto for providing the access to the WACSIS database.

Finally, thanks to the Offshore Technology Research Center for the financial support.

TABLE OF CONTENTS

Page

CHAPTER Page

Page

LIST OF FIGURES

FIGURE Page

FIGURE Page

FIGURE Page

LIST OF TABLES

CHAPTER I

INTRODUCTION

1.1 Backgrounds

Field measurements are important for the verification of wave theories and calibration of hindcast model (Wyatta et al., 2003, Forristall et al., 2004). The accuracy of the measurements is essential for data analysis. Because there is no absolute reference to benchmark the measurements, the inter-comparison between different measurements is important for acquiring and validating the field data. In WACSIS project, the sea-state parameters estimated from the time series recorded by different sensors are compared with each other to ensure the data quality (Barstow et. al., 2004). Forristall et al. (2004) compared the crest height distributions derived from different measurements with those derived from second order simulations to examine the quality of field data. Moreover, the inter-comparison is also an efficient way to evaluate the performance of new technology applied to field measurement (Strong et al. 2000).

The comparison between sea-state parameters is not a complete examination of data quality. For example, the agreement between energy spectra estimated from different sensors cannot validate whether or not the phase information is accurately recorded by either one. The consistency between the time series recorded by different instruments can provide us the highest level of confidence on data quality. Barstow et al. (2004) compared time series of highest four individual crests recorded by two instruments, Marex radar and EMI laser, to ensure the confidence of the measurements. It should be indicated that these two instruments were deployed in very close locations, which make the direct and simultaneous comparison possible. To conduct the inter-comparison

---

This dissertation follows the style and format of the *Journal of Physical Oceanography*.

between the time series of different wave properties recorded at different locations, deterministic analyses are necessary. In deterministic analyses, the information of free wave components, including the frequency, amplitude, direction of propagation and initial phase is obtained after the nonlinear effects are decoupled from the measured wave properties. The time series of wave properties at a given location can be deterministically predicted by superposing the contributions from all free waves and their bound waves. The predicted time series is then compared with that recorded at the same location. Such inter-comparison is seldom found in the literatures due to the complicacy of deterministic analysis of directional wave fields. Sand (1984) decomposed the directional wave field based on the pith/roll buoy measurements and current meter/wave gauge measurements using linear wave theory. He assumed that there are two free wave components at each frequency and they travel at different directions and have the phase difference of $\pi/2$. In his method, the estimated wave direction relies on the initial phase of measured time series, which obviously contradicts to the reality. Skourup and Sterndorff (2002) introduced a deterministic model for the reproduction of measured wave time series in a wave flume. Based on the measured long-crested surface elevation time series at one location, the elevation time series and the kinematics can be predicted at another location. But they did not solve the divergence problem which occurs when the wave properties resulting from nonlinear interactions are comparable with or larger than the corresponding linear ones. In their model, when the amplitude of a wave component in 2^{nd} order spectrum exceeds the amplitude of the wave components in the measured spectrum, then the first order component is artificially set to zero and the 2^{nd} order component is set equal to the measured spectrum component to avoid the divergence problem. Zhang et al. (1999a&b) developed a Directional Hybrid Wave Model (DHWM) for the deterministic decomposition of directional waves accurate up to second order in wave steepness. Two different perturbation methods are adopted in DHWM to avoid the divergence problem. Using the decomposed free-wave components, accurate prediction of wave kinematics, pressure, and elevation can be made.

The DHWM is robust for the engineering applications, such as the determination of the initial and boundary conditions for a variety of numerical wave tanks. But the original version of DHWM does not consider the effects of ocean currents. It is well known that when a wave train propagates over a uniform and steady current, it experiences the Doppler frequency shift. The Doppler shift is purely an effect of the measurement frame and does not include the wave-current physical interactions. The fixed instruments measure the apparent frequency only. But the dispersion relationship relates the wavenumber to the intrinsic frequency. Thus, to properly analyze the directional waves in presence of current, the Doppler shift must be accounted for. Forristall and Ward (1978), Nakagawa et al. (1996) and Steele (1997) showed that the energy spectra, directional spreading and mean wave direction could be altered by the Doppler effect. Therefore, the nonlinear DHWM needs to be extended for the analysis of the directional waves in the presence of strong current.

To obtain the information about the mean wave direction and energy spreading is a key issue of the analysis of directional waves. This information is crucial to the applications of oceanography, coastal and ocean engineering (Forristall and Ewans, 1998), such as the estimations of wave loads on offshore or coastal structures and the sediment transport in a surf zone. A simple wave model, known as a cosine-2*s* model, has been widely used to describe wave energy spreading in a uni-modal wave field where water waves at the same frequency spread around only one main direction although at different frequencies the main wave directions may be different (Hwang and Wang, 2000). A cosine-2s model defines the spreading function by,

$$D(\theta) = \kappa \cos^{2s}\left(\frac{\theta - \theta_M}{2}\right) \tag{1.1}$$

where κ is a normalization factor,

$$\kappa = \frac{2^{2s-1}}{\pi}\frac{\Gamma^2(s+1)}{\Gamma(2s+1)}, \tag{1.2}$$

$\Gamma(x)$ is the Gamma function, θ_M the mean wave direction and s the directional spreading parameter. Both θ_M and s are a function of the wave frequency f. The spreading parameter s and the mean wave direction θ_M are related to the first harmonic through

$$s_1 = \frac{r_1}{1-r_1} \tag{1.3}$$

$$\theta_{M1} = \tan^{-1}\frac{B_1}{A_1} \tag{1.4}$$

$$r_1 = \sqrt{A_1^2 + B_1^2} \tag{1.5}$$

or to the second harmonic through

$$s_2 = \frac{1+3r_2+\sqrt{1+14r_2+r_2^2}}{2(1-r_2)} \tag{1.6}$$

$$\theta_{M2} = \tan^{-1}\frac{B_2}{A_2} \tag{1.7}$$

$$r_2 = \sqrt{A_2^2 + B_2^2} \tag{1.8}$$

where A_n and $B_n\,(n=1\&2)$ are the angular Fourier coefficients of $D(\theta)$ and can be estimated from the cross spectra of the measurements using the Direct Fourier Transfer (DFT) method (Longuet-Higgins et al., 1963). This approach is referred as the conventional approach in the following text and has been widely used to determine the mean wave direction θ_M and spreading parameter s. For example, wave data recorded by

NDBC buoys are routinely processed using this approach (Earle, 1996). Ideally, if the directional spreading in ocean waves truly follows a cosine-2s model and the first two angular Fourier coefficients can be accurately computed based on the cross spectra free from errors, then the spreading parameter and mean wave direction estimated, respectively, based on the first and second Fourier coefficient should be identical, i.e., $s_1 = s_2$ and $\theta_{M1} = \theta_{M2}$. Our tests conducted in this study show that even if a homogenous wave field is numerically generated following a cosine-2s model and based on linear wave theory the estimated cross spectra involve random errors resulting from the 'interaction' term (Jefferys 1987). For field measurements, much more uncertainties exist in cross spectra estimation, such as measurements noises and the nonlinear effects, just to name a few. It can be seen from Eqs. (1.3) and (1.6) that s_1 and s_2 are sensitive to errors in estimating the cross spectra. A small error in estimating the cross spectra may be greatly amplified and result in an extremely large error in estimating the spreading parameter as well as significant inconsistency between estimated s_1 and s_2. The reported significant differences between s_1 and s_2 estimated from field data can be found in Hasselmann et al. (1980), Ewing and Laing (1987), Wang and Freise (1997) and the database of NDBC (http://www.ndbc.noaa.gov/rmd.shtml).

1.2 Objectives

From the introduction of pertinent studies on the directional waves, it is noted that the DHWM has the capability of filling the gap that there is no reliable nonlinear deterministic analysis method for examining the quality of field measurements. For the analysis of directional waves on strong currents, it needs to be extended to account for the effects of Doppler frequency shift. Moreover, the estimation of wave energy spreading properties using the conventional approach is not stable. It could be improved with an alternative approach. Therefore, the objectives of this study are:

1) Conducting deterministic analysis to examine the consistency of field measurements of different type of sensors or same type of sensors at different locations using a Directional Hybrid Wave Model;

2) Extending a Directional Hybrid Wave Model to allow for the deterministic analysis of directional waves in the presence of strong current; and

3) Developing a new scheme to estimate the directional energy spreading that is less sensitive to the errors in the estimated cross spectra.

CHAPTER II

DIRECTIONAL HYBRID WAVE MODEL*

2.1 Mode Coupling Method and Phase Modulation Method

2.1.1 Background

Ocean waves are often modeled by a superposition of many monochromatic waves with different frequencies, amplitudes and directions. The basic wave components are known as free waves, whose frequency and wavelength obey the dispersion relationship. Due to the nonlinear nature of surface water waves, free waves interact with each other when they travel in the same area. Based on their effects on wave characteristics, wave-wave interactions are classified into strong and weak interactions. The phenomena of strong interactions are observable soon after the free waves start to interact, while those of weak interactions become substantial only after hundreds of wave periods (Phillips, 1979 and Su & Green, 1981). Weak interactions, also known as resonance wave interactions, may occur when the frequencies and wavelengths of interacting free waves satisfy the resonance condition. Resonance interactions result in energy transfer among free waves of different frequencies (Phillips, 1960, and Hasselmann, 1962) and hence are crucial to long duration or distance wave energy evolution in the air-sea interactions (Komen et al., 1994). Strong interactions among free waves change the resultant wave characteristics, which is often quantified in terms of bound (or force) waves. Different from free waves, the wavelength and frequency of a bound wave do not obey the dispersion relationship. Although bound waves are observable immediately after the interactions start, they disappear after the interacting waves no longer overlap (Yuen & Lake, 1982). Hence, in the studies of the evolution of wave characteristics in a short duration or distance (a few typical wave periods or wavelengths), we focus on strong interactions while neglect weak interactions.

---

* Parts of this Chapter are copied from class notes of OCEN689 at TAMU (Zhang, 2005).

Most analytic and numerical studies on the evolution of a nonlinear wave train in space and time are based on the information of the free (linear) waves consisting of the wave train. The wave characteristics are the superposition of those of free wave components and the nonlinear interaction among them. In reality, measured wave properties, such as wave elevation, pressure and kinematics, do not directly divulge the information of free waves but the resultant of all free waves and their interactions (bound waves). Linear decomposition of a measured wave field considers all waves (including bound waves) as free waves, which may result in significant errors in many applications, such as prediction of wave kinematics and estimation of energy loss due to wave breaking, especially when waves are steep (Spell et al., 1996, Meza et al., 2000). To estimate the wave characteristics accurately, the bound waves need to be excluded from the resultant wave field, but the computation of bound waves needs the information of free waves. Hence, nonlinear decomposition is accomplished through iterative procedures. To reach accurate results for the decomposition, perturbation solutions for computing bound waves or strong interactions must converge. In this Chapter, we introduce two different types of perturbation methods, known as Mode Coupling Method (MCM) and Phase Modulation Method (PMM), used in Directional Hybrid Wave Model (DHWM).

The majority of perturbation methods for computing strong interactions belong to the school of conventional perturbation methods. MCM or Stokes expansion methods may be the most widely used one (West et al., 1974). A common thread linking all conventional perturbation methods is their solution characterized by linear phase and exponential (or hyperbolic) function for modeling the velocity potential and elevation of free and bound waves. In a conventional method, the phase of a free or bound wave is linear in the horizontal coordinates and time (only constant wavenumber and frequency are allowed). Linear phase allows relatively simple algebraic manipulation in deriving solutions and provides direct relation to the Fast Fourier Transfer (FFT) of wave records. However, the conventional solution may result in slow convergence or even divergence

if truncated at certain orders in wave steepness, which will be elaborated in the following text.

A modulated phase involving non-constant wavenumber was employed for studying the variation of the elevation of a short wave riding on a wave of drastically longer wavelength by Phillips (1981), and the numerical calculation by Longuet-Higgins (1987). A complete solution in phase modulation formulation truncated at third order was derived using a conformal mapping approach for the strong interaction between a periodic short and long wave (Zhang et al., 1993). Owing to the explicit use of modulated phase in the solution, the related perturbation method was given the name, Phase Modulation Method (PMM). In principle, a PMM solution differs from that of a conventional perturbation method in two major aspects. First, it employs a nonlinear phase for a modulated wave so that its modulated wavenumber and frequency can be directly accounted by the phase. Secondly, a PMM solution for the potential of a modulated wave is constructed differently from that of a conventional method. Although the former remains the product of two functions, it is no longer formulated according to a variable separation method for solving the Laplace equation as used in a conventional method. The advantage of a PMM solution is to render convergent solution while the corresponding conventional solution may fail. The disadvantage is that its derivation is more complicated and lengthy than in a conventional method, especially when conformal mapping approaches are used. Hence, in quantifying strong interactions in an irregular wave field of a broad-banded spectrum, the PMM was used as a complementary method to the MCM, providing convergent solutions for the strong wave interactions where the latter fails (Zhang et al., 1996 & 1999a).

For an irregular wave field, the linear solution of a single wave is viewed as a general solution at first order because the total first-order solution for an irregular wave field is the superposition of the linear solution for each free wave involved in this wave field. A second-order general solution involves at most two distinct free waves. The second

harmonic of a free wave is a special case resulting from the interaction with itself. Noticing that the DHWM is truncated up to second order in wave steepness, so only the solution involving a pair of free wave components is discussed in the following text.

2.1.2 Governing Equation for Surface Gravity Waves

Cartesian coordinates are defined such that the plane of *x*-*o*-*y* is coincident with the still water level (SWL) and the *z*-axis points upward. Assuming that water is incompressible and flow is irrotational, the velocity potential satisfies the Laplace equation:

$$\nabla^2\phi = 0\,. \tag{2.1}$$

When water is deep or its depth, *h,* is uniform, then the bottom boundary condition for the potential is

$$\nabla\phi \to 0 \quad z \to -\infty\,, \tag{2.2}$$

or

$$\frac{\partial\phi}{\partial z} = 0 \quad \text{at } z = -h\,. \tag{2.3}$$

In the absence of wind and neglecting surface tension and Coriolis force, the dynamic and kinematic boundary conditions at the free surface are given by:

$$\frac{\partial\phi}{\partial t} + g\eta + \frac{1}{2}\left|\nabla\phi\right|^2 = C(t) \qquad \text{at } z = \eta\,, \tag{2.4}$$

$$\frac{\partial\phi}{\partial z} - \frac{\partial\eta}{\partial t} - \nabla_h\phi\cdot\nabla_h\eta = 0 \qquad \text{at } z = \eta\,, \tag{2.5}$$

where η is the surface elevation, $C(t)$ the Bernoulli constant to be chosen so that $z = 0$ located at the SWL and g the gravitational acceleration. Notations ∇ and ∇_h stand for the

gradient and horizontal gradient operators, respectively. In the absence of lateral physical constraints, a periodic lateral boundary condition for waves is invoked.

2.1.3 Solution Using MCM

The Mode Coupling Method (MCM), also known as Stokes Expansion, is applied to solve Eqs. (2.1) – (2.5) for deep or intermediate water depth conditions. In MCM, ϕ, η and C are expressed as the perturbation series:

$$\phi = \phi^{(1)} + \phi^{(2)} + \phi^{(3)} + \cdots + \phi^{(j)} + \cdots \tag{2.6}$$

$$\eta = \eta^{(1)} + \eta^{(2)} + \eta^{(3)} + \cdots + \eta^{(j)} + \cdots \tag{2.7}$$

$$C = C^{(1)} + C^{(2)} + C^{(3)} + \cdots + C^{(j)} + \cdots \tag{2.8}$$

The *(j)* indicates the order of perturbation. Using the Taylor expansion, the free surface boundary conditions, i.e. Eqs. (2.4) – (2.5), are expanded at the still water level ($z = 0$). And then Eq. (2.6) is substituted into the Laplace equation and boundary conditions. The equations are sorted and grouped according to the order of general wave steepness, defined as $a_i k_j$, i may or may not equal to j. the hierarchy equations are solved sequentially from lower to higher order until the required accuracy is reached. The details can be found in Longuet-Higgins & Stewart (1960) and are omitted here.

Eqs. (2.9) and (2.16) are the second-order solutions for two interacting free waves. They represent the general solution for ϕ and η at second order because the total second-order solution for a wave field is equal to a double summation of this second-order general solution over all possible pairs of free waves in the wave field.

$$\phi^{(1)} = \sum_{j=1}^{2} \frac{a_j g}{\sigma_j} \frac{\cosh\left[k_j (h+z)\right]}{\cosh(k_j h)} \sin\psi_j \tag{2.9}$$

$$\phi^{(2)} = \sum_{j=1}^{2} \frac{3}{8} \frac{a_j^2 \sigma_j \cosh\left[2k_j(h+z)\right]}{\sinh^4\left(k_j h\right)} \sin 2\psi_j$$
$$+ \frac{a_1 a_2 \sigma_2}{2} A_{(-)} \frac{\cosh\left[\left|\overrightarrow{k_1} - \overrightarrow{k_2}\right|(h+z)\right]}{\cosh\left(\left|\overrightarrow{k_1} - \overrightarrow{k_2}\right| h\right)} \sin\left(\psi_1 - \psi_2\right) \tag{2.10}$$
$$+ \frac{a_1 a_2 \sigma_2}{2} A_{(+)} \frac{\cosh\left[\left|\overrightarrow{k_1} + \overrightarrow{k_2}\right|(h+z)\right]}{\cosh\left(\left|\overrightarrow{k_1} + \overrightarrow{k_2}\right| h\right)} \sin\left(\psi_1 + \psi_2\right)$$

where,

$$A_{(\mp)} = \mp \frac{k_2\left[2\lambda\left(1 \mp \lambda\right)\left(\Gamma\alpha_1\alpha_2 \pm 1\right) \mp \lambda^3\left(\alpha_1^2 - 1\right) + \alpha_2^2 - 1\right]}{k_2\left(1 \mp \lambda\right)^2 - \alpha_2\left|\overrightarrow{k_1} \mp \overrightarrow{k_2}\right| \tanh\left(\left|\overrightarrow{k_1} \mp \overrightarrow{k_2}\right| h\right)} \tag{2.11}$$

$$\alpha_j = \coth(k_j h), \quad j = 1, 2 \tag{2.12}$$

$$\psi_j = \overrightarrow{k_j} \cdot \overrightarrow{X} - \sigma_j t + \delta_j \tag{2.13}$$

$$\Gamma = \cos\left(\theta_1 - \theta_2\right) \tag{2.14}$$

$$\lambda = \frac{\sigma_1}{\sigma_2} \tag{2.15}$$

$a_j, \sigma_j, k_j, \theta_1$, and ψ_j are the wave amplitude, frequency, wavenumber, wave direction and linear phase, respectively. By default, $\sigma_2 > \sigma_1$.

$$\eta^{(1)} = \sum_{j=1}^{2} a_j \cos\psi_j \tag{2.16}$$

$$\eta^{(2)} = \sum_{j=1}^{2} \frac{a_j^2 \sigma_j^2}{4g} \left[2 + \frac{3\cosh(2k_j h)}{\sinh^4(k_j h)} - \frac{1}{\sinh^2(k_j h)} \right] \cos 2\psi_j$$
$$+ \frac{a_1 a_2 k_2}{2\alpha_2} \left[-(1-\lambda) A_{(-)} + M_{(-)} \right] \cos(\psi_1 - \psi_2) \qquad (2.17)$$
$$+ \frac{a_1 a_2 k_2}{2\alpha_2} \left[(1+\lambda) A_{(+)} + M_{(+)} \right] \cos(\psi_1 + \psi_2)$$

where,

$$M_{(\mp)} = \lambda^2 + 1 - \lambda(\Gamma \alpha_1 \alpha_2 \pm 1) \qquad (2.18)$$

In using MCM, there is a weakly nonlinear assumption that all general wave steepness must be much smaller than unity, $a_i k_j \ll 1$, to assure the convergence of Eq. (2.6). This requirement may be satisfied in a wave field of a relatively narrow banded spectrum. However, in the case of a wave field of a broad-banded spectrum one or several wave steepnesses may be close to or even greater than unity. For example, if $a_1 k_1 = 0.12$ and the wavelength ratio is $k_1 / k_2 = 1/9$, $a_1 k_1 = 1.08$. Thus, certain second- and high-order solutions related to these wave steepnesses may not be much smaller than lower-order solutions. Under this circumstance, truncated MCM solutions converge slowly or even diverge.

The above convergence difficulty may be eased and eventually overcome if the perturbed solution is truncated at orders high enough. However, not only high-order solutions for multiple interacting free waves become extremely lengthy and complicated, but also new types of convergence difficulties may occur (Zhang, 2005) and the details are omitted here because we only discuss the solutions up to second order.

2.1.4 Solution Using PMM

A periodic wave train is steady in the coordinates moving at its phase velocity. Using conformal mapping approach, the physical fluid domain of a steady periodic wave train can be mapped onto a rectangular domain whose coordinates respectively correspond to streamlines and equal-potentials of the wave train in the physical domain. The solution for a periodic wave train is first derived in the mapping domain and then converted to the form in the physical fluid domain (Schwartz, 1974, Cokelet, 1977). This approach was extended to study the interaction between a co-linear weakly nonlinear short-wave and long-wave train in deep water (Zhang et al., 1993) and in intermediate water depth (Chen and Zhang, 1998). The short-wave solution expressed in the physical domain (Cartesian coordinates) clearly shows that the amplitude and phase of its elevation are modulated along the long-wave surface and more importantly reveals its potential function being modulated both vertically and horizontally.

The solutions derived using conformal mapping approaches provided valuable knowledge on the physical interpretation and structure of a PMM solution. One of the important findings is that the solutions derived respectively using a MCM and PMM are identical up to a truncated order when both are convergent and converted to the same format of functions. This finding laid a solid foundation for the development of a new approach, known as solution-matching approach (Zhang, 2005). It directly renders a PMM solution in the Cartesian coordinates based on the matching with the corresponding MCM solution, thus avoiding lengthy procedures of conformal mapping.

There are three steps in the solution-matching approach to derive a PMM solution. First, a general PMM solution with unknown modulation functions is proposed for a modulated wave. The constraints on these modulation functions are obtained to satisfy the Laplace equation. Secondly, taking the advantages of the fact that an expanded PMM solution is identical to the corresponding MCM solution up to a truncated order, the unknown modulation functions are determined by matching them. The finally task is to

examine whether or not the PMM solution derived through matching satisfies the Laplace equation, bottom and free-surface boundary conditions for the short-wave train and more importantly to show that it is convergent when the corresponding MCM solution diverges.

Following the procedure above, The PMM solution for a short wave modulated by a long wave is:

$$\phi_3^{(1)} = \frac{a_3 g}{\sigma_3} \widetilde{V}\left(z,x,y,t\right) \widetilde{H}\left(x,y,t,z\right) \tag{2.19}$$

$$\eta_3^{(1)} = a_3 \left[1 + f_a\left(x,y,t\right)\right] \cos \widetilde{\widetilde{\psi}}_3 \tag{2.20}$$

where,

$$\widetilde{V}(z,x,y,t) = \exp\left[k_3 (z + f_k\left(x,y,z,t\right)\right] \tag{2.21}$$

$$\widetilde{H}(x,y,t,z) = \sin \widetilde{\psi}_3 \tag{2.22}$$

$$\widetilde{\psi}_3 = \psi_3 + k_3 f_{\psi,\phi}(x,y,z,t) \tag{2.23}$$

$$\widetilde{\widetilde{\psi}}_3 = \widetilde{\psi}_3\Big|_{z=\eta_l} + k_3 f_{\psi,\eta}(x,y,t) \tag{2.24}$$

$$f_k = a_1 \cos\psi_1 \left[B_{(-)} e^{\left(\left|\bar{k}_3 - \bar{k}_1\right| - k_3\right)z} - B_{(+)} e^{\left(\left|\bar{k}_3 + \bar{k}_1\right| - k_3\right)z} \right] \tag{2.25}$$

$$f_{\psi,\phi} = -a_1 \sin\psi_1 \left[B_{(-)} e^{\left(\left|\bar{k}_3 - \bar{k}_1\right| - k_3\right)z} + B_{(+)} e^{\left(\left|\bar{k}_3 + \bar{k}_1\right| - k_3\right)z} \right] \tag{2.26}$$

$$f_a = a_1 k_3 \cos\psi_1 \left[\left(B_{(-)} - B_{(+)}\right) - \lambda \left(B_{(-)} + B_{(+)}\right) - \lambda \alpha_1 \Gamma + \lambda^2 + 1 \right] \tag{2.27}$$

$$f_{\psi,\eta} = -a_1 \sin\psi_1 \left[\left(B_{(-)} + B_{(+)}\right) - \lambda \left(B_{(-)} - B_{(+)}\right) - \lambda \right] \tag{2.28}$$

$$B_{(-)} = \frac{\lambda\left(1-\lambda\right)\left(1+\alpha_1\Gamma\right) - \frac{\lambda^3}{2}\left(\alpha_1^2 - 1\right)}{\left(1-\lambda\right)^2 - \sqrt{1 - 2\lambda^2 \Gamma \alpha_1 + \lambda^4 \alpha_1^2}} \tag{2.29}$$

$$B_{(+)} = \frac{\lambda(1+\lambda)(1-\alpha_1\Gamma) - \frac{\lambda^3}{2}\left(\alpha_1^2 - 1\right)}{(1+\lambda)^2 - \sqrt{1+2\lambda^2\Gamma\alpha_1 + \lambda^4\alpha_1^2}} \tag{2.30}$$

The short wave is denoted by subscript '3' and the long wave by '1'.

The details of matching procedures and the proof of the above solution satisfying the free-surface boundary conditions were given in Zhang (2005) and are omitted here. As shown in the above equations, a PMM solution involves a modulated phase. More significantly, the modulated 'horizontal' and 'vertical' functions ($\widetilde{H}$ and $\widetilde{V}$) are different from the conventional vertical and horizontal functions in a MCM solution. The former are NOT based on a variable separation method for solving the Laplace equation. The modulated 'vertical' function, $\widetilde{V}$, depends dominantly on the vertical coordinate but also weakly on the two horizontal coordinates and time as indicated by the modulation function, f_k. The exponential index of $\widetilde{V}$ is no longer a linear function of *z*. The modulated 'horizontal' function, $\widetilde{H}$, depends dominantly on the two horizontal coordinates and time and weakly on the vertical coordinate. While the modulation of elevation amplitude is explicitly described by f_a, the modulation of potential amplitude is implicitly involved in f_k. In general, the modulated phase of the short-wave elevation is slightly different from that of the potential at undisturbed long-wave surface and the difference is denoted by $k_3 f_{\psi,\eta}$. $f_k, f_{\psi,\phi}, f_a$ and $f_{\psi,\eta}$ depend on the characteristics of the long-wave train and hence vary slowly in space and time in comparison with the phase of the short-wave train.

To describe the physics clearly, we can simply Eqs. (2.25) – (2.28) for unidirectional wave in deep water case. Notice that in deep water, $\alpha_j = \coth\left(k_j h\right) = 1$

$$f_k = -a_1 e^{-k_1 z} \cos\psi_1 \tag{2.31}$$

$$f_{\psi,\phi} = a_1 e^{-k_1 z} \sin\psi_1 \tag{2.32}$$

$$f_a = \varepsilon_1 \cos\psi_1 \tag{2.33}$$

$$f_{\psi,\eta} = 0 \tag{2.34}$$

When $z \to -\infty$, the term, $a_1 e^{-k_1 z} \cos\psi_1$ involved in f_k, seems to grow infinitely, which violates the bottom boundary condition. However, it should be noticed that $\exp[k_3(z + f_k)] \downarrow 0$ in the range $k_3|z| \sim O(1)$ (where $k_1|z| \ll O(1)$ because $k_1 \ll k_3$). The reason for imposing the limit on the depth range $k_3|z| \sim O(1)$ is that the short-wave potential is trivial far beyond that range. Eq. (2.33) clearly represents the modulation by first harmonics of the long wave.

When $k_3 \gg k_1$ and $k_3 a_1 \sim O(1)$, it was shown in Section 2.1.3 that the corresponding MCM solution is divergent. Hence, we examine the convergence of the PMM solution under this scenario. First, the perturbed solution decays with the increase in perturbation orders. Secondly, noticing that $f_a \sim O(\varepsilon_1)$, the modulation of the amplitude of short-wave elevation is of order $O(\varepsilon_1)$, which is an order smaller than the short-wave amplitude. Although the modulation in the phases of the potential and elevation can be of order $a_1 k_3 \sim O(1)$, the order of the short-wave amplitude remains unchanged because the phase modulation is contained in a sine or cosine operator (Eq. (2.23)). In addition, all modulation functions are convergent, namely, the modulation caused by the long-wave second harmonic is an order smaller than that by the long-wave first harmonic. Hence, the PMM solution is well behaved even when $k_3 \gg k_1$ and $k_3 a_1 \sim O(1)$.

2.2 Numerical Scheme of Directional Hybrid Wave Models

2.2.1 Decomposition

To ensure the solution for strong interactions or bound waves is convergent, two complementary perturbation methods, namely MCM and PMM are used in Directional Hybrid Wave Model (DHWM). In principle, the computation of bound waves in an irregular wave field is made using a MCM general solution as long as it converges and a PMM is used only when the corresponding MCM solution likely diverges. It is because the computation using a MCM solution is simpler than using a corresponding PMM solution. Considering the computation of bound waves employing two different perturbation methods, the related wave models are named as Hybrid Wave Models.

To apply the two methods respectively to the interactions between free waves of quite different and close frequencies, free waves of relatively close frequencies are bundled into bands in the frequency domain. Depending on the frequency range of free waves involving substantial energy, a spectrum can be divided into six or more bands in the frequency domain as sketched in Figure 2.1. Bands are numbered from 0 to 5 in the order from low to high frequency. The spectral peak of ocean waves having a single-peak spectrum is likely located in Band 1. We define that free waves in Band 0 do not have significant energy. Thus the interaction of free waves in Band 0 with other free waves is insignificant and can be neglected. Although the cutoff frequency is set at the end of the last band (Band 5), the cut-off frequency of free waves is at the end of Band 4. Only free waves located in Bands 1 to 4 may have significant energy and consequently we only consider interactions among the free waves in these bands. In the case of a wave field being extremely broad banded, the number of bands of free waves involving significant wave energy can be more than four. As shown in Figure 2.1, the frequencies of any pair of free waves located in the same band or neighboring bands are relatively close and so are their wavelengths. Consequently, the interaction between them is computed using MCM. On the other hand, the frequencies of any pair of free waves are

quite different when they located in two different bands separated by at least one band. Therefore, their interaction is computed using PMM.

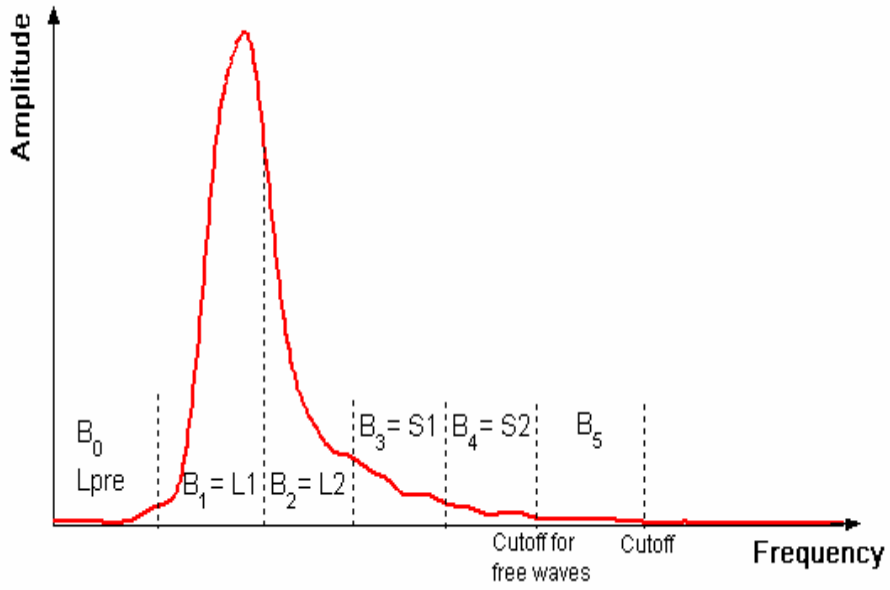

Figure 2.1 Band division of a typical wave spectrum (Zhang, 2005)

The DHWM contains two independent computation blocks: decomposition and prediction (superposition). When the computation is based on measured wave records, we need to decompose the measured wave field to obtain the information of free waves. The decomposition is achieved through iterative processes. In the first iteration, free waves are approximately computed based on linear wave theory and then bound waves are calculated based on the approximated free waves. In the next iteration, the revised measurements, in which bound waves have been subtracted or decoupled, are used to determine free waves. The newly computed free waves are then used to compute bound waves again. The iteration continues until the discrepancies between two sets of free

waves computed from two consecutive iterations are smaller than a prescribed error tolerance. The above iterative processes also involve additional steps to determine the wave direction, the number of directional free waves at each discrete frequency to represent the directional spreading and the initial phase of free waves. A flowchart illustrating the processes of iteration is sketched in Figure 2.2. The decomposition consists of three major steps: wave direction estimation, initial phase estimation, and computation and subtraction of the bound waves from the measurements. To achieve relatively fine resolution in wave direction using as few as three simultaneous wave records, the estimate of wave energy spreading is based on data-adaptive methods, such as Maximum Likelihood Method (MLM) and Maximum Entropy Method (MEM). In DHWM, the extended MLM (EMLM) was employed (Isobe et al., 1984). Knowing the directional spreading at a frequency, one or several directional free waves are chosen such that their amplitudes and directions conserve the total energy and approximately resemble the energy spreading at the frequency. The initial phases of the free waves are then determined by minimizing the square of the differences between the measurements and the resultant of predicted free and bound waves. Once the initial phases, amplitudes and directions of free waves are computed, the bound waves resulting from their interaction are calculated and then subtracted from the corresponding measurements.

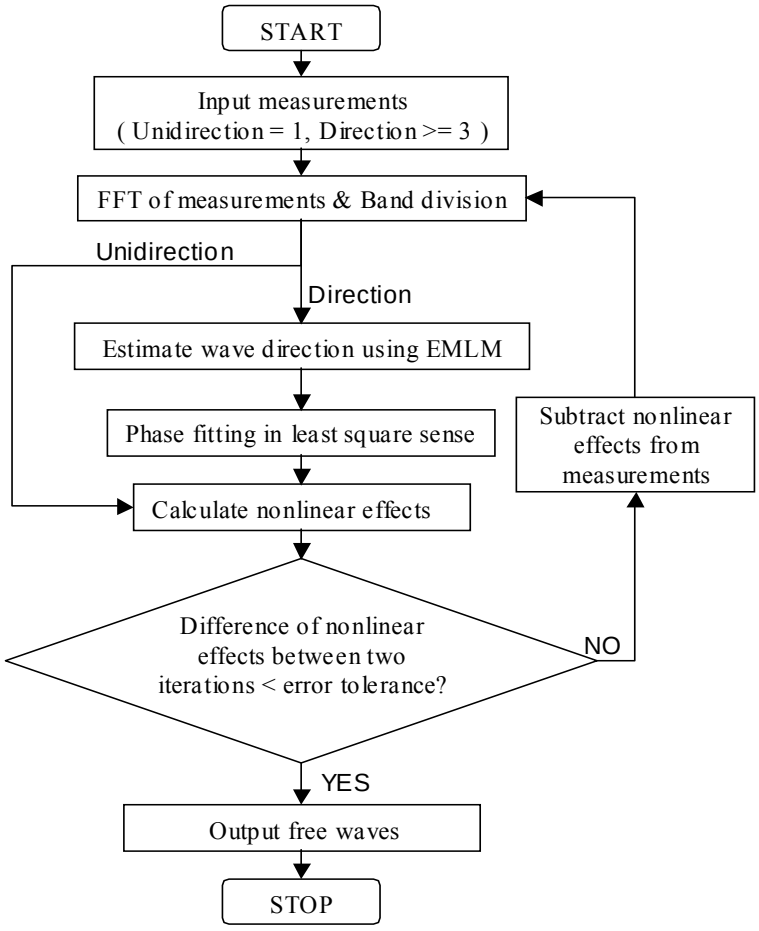

Figure 2.2: Flowchart of decomposition (Zhang, 2005)

2.2.2 Superposition

The information of free waves obtained in the decomposition or from other sources can be used for the prediction of resultant wave characteristics in the time domain. Wave characteristics predicted within an area of a few typical wavelengths from the location of measurements are relatively accurate. Further away from the measured location, either a higher order model should be used or the accuracy of prediction deteriorates. The computation of a bound wave using either MCM or PMM follows the same principles described in the decomposition. Based on the band division, the former is used to

compute bound waves resulting from any pair of free waves located in the same band or neighboring bands while the latter to compute bound waves resulting from any pair of free waves in two different bands separated by at least one other band. After the bound waves are calculated, their contribution is added to that of free waves to render the resultant wave characteristics at a given location. To be consistent with the assumption made in wave decomposition, the contribution from the free waves in Band 0 is included in the resultant wave characteristics while their interaction with other free waves are neglected.

2.3 Applications

The linear wave theory is widely employed in engineering practice and usually renders fairly good results. However, in cases that ocean waves are steep and have a broad band spectrum, the contributions from bound wave components at either low or high frequencies could be significant and the linear wave theory could fail in predicting the wave properties. Zhang (1999c) showed some applications of DHWM where linear theory fails. One of the examples is the estimation of kinematics near wave crests. It was well documented that the predicted particle velocity near a steep wave crest based on linear wave theory is far from satisfied (Wheeler, 1970). But the DHWM is able to predict the kinematics much more accurately because it distinguishes bound waves from free waves and computes their contributions to the wave kinematics accordingly. Another example is the estimation of low-frequency responses of a SPAR. Strong interactions among free waves are known to generate different-phase bound waves of very low frequencies close to the natural frequencies of a SPAR and may resonantly excite slow-drift motion of a SPAR. The DHWM can predict the kinematics of free waves and low frequency bond waves accurately, which is used as the input to the Morison Equation to calculate wave forces and then the surge, pitch and heave motions of a SPAR in the time domain (Cao & Zhang, 1997). Meza et al. (2000) applied DHWM to the study on the free wave energy dissipation due to wave breaking. The changes in wave energy at low- and high-frequency bands due to wave breaking were clearly

depicted after the contributions from bound waves were excluded using DHWM. The DHWM is also an excellent tool for the determination of boundary conditions of nonlinear numeric wave tank. In Chapter IV, the application of DHWM on WACSIS data analyses will be explored in detail.

CHAPTER III

WACSIS DATABASE

3.1 Introduction of WACSIS

The Wave Crest Sensor Inter-comparison Study (WACSIS) was designed as a thorough investigation of the statistical distribution of crest heights. Measurements were made in the southern North Sea during the winter of 1997-1998 from the Meetpost Noordwijk (MPN) platform in 18 m water depth. The platform is one of the stations of the North Sea monitoring Network and located 9 kilometers off the Dutch coast, near the coastal resort of Noordwijk. Figure 3.1 shows a picture of MPN looking from the Northwest.

Figure 3.1: Northwest corner of MPN (Prevosto et al., 2001)

The wave elevation sensors used in WACSIS include Baylor Wave Staff, EMI Laser, Marex radar, SAAB Radar, Vlissingen and Marine 300 step gauge. An S4ADW current meter was also deployed at 11.5m below the still water level to measure wave-induced horizontal velocities and pressure. In addition, a directional Waverider Buoy was deployed about one kilometer away from the platform to provide information on wave direction. An overview of WACSIS sensors is given in Table 3.1. In order to have records from different sensors with common sampling frequencies, the original data was resampled at 4Hz, 2Hz, and 1Hz. Figure 3.2 shows the locations of these sensors with respect to the platform and the orientation of the platform. The coordinates of the sensors whose records are used in the next chapters are listed in Table 3.2. The more comprehensive description of the WACSIS and its measurement can be found in Forristall et al. (2004)

Table 3.1: Overview of WACSIS sensors (Prevosto et al., 2001).

Sensor Name	Measurement Principle	Sampling Frequency	
Baylor Wave Staff	Inductance	4	[Hz]
THORN Wave Height Sensor	Laser	4	[Hz]
MAREX SO5 Wave Radar	Radar	4	[Hz]
SAAB Radar	Radar	5.12	[Hz]
Vlissingen Step Gauge	Electrodes	10	[Hz]
Marine 300 Step Gauge	Electrodes	10	[Hz]
Directional Waverider Buoy	Acceleration	1.28	[Hz]
SMART 800 GPS Buoy	GPS/Doppler	1	[Hz]
WAVEC Directional Buoy	Acceleration/Tilt	1.28	[Hz]
S4ADW Current Meter	Conductivity	2	[Hz]
Video Camera	Visual Inspection	2	[Hz]

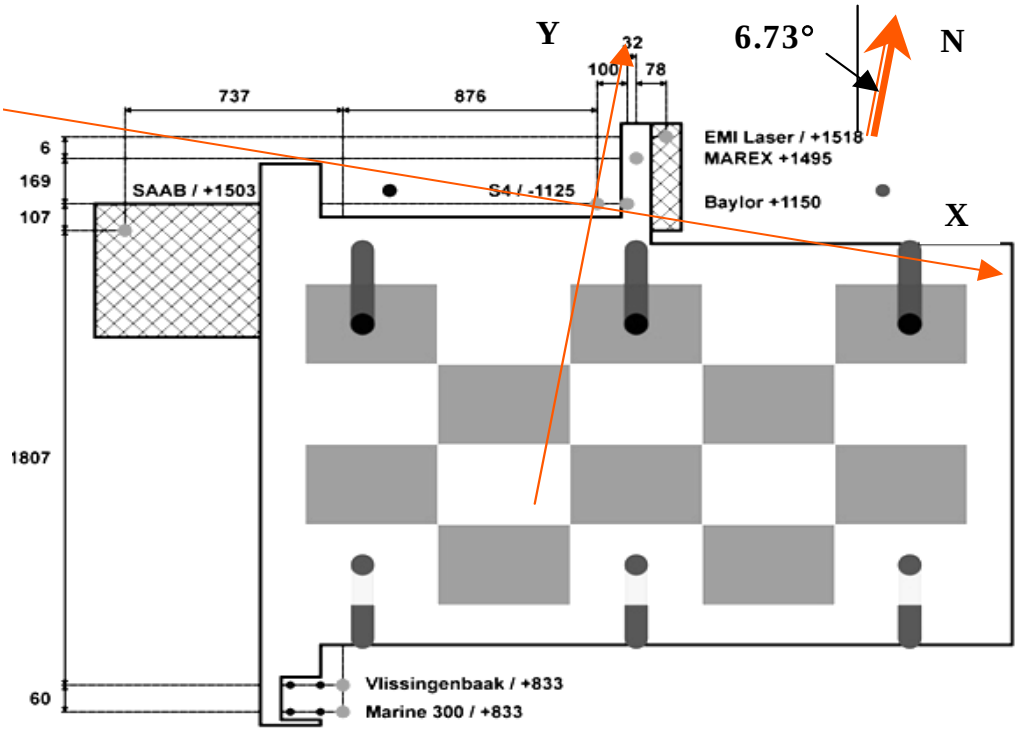

Figure 3.2: Plan view of sensor layout

Table 3.2: Coordinates of WACSIS sensors.

Sensor Name	X (m)	Y (m)	Z (m)
SAAB Radar	-15.89	-2.95	N/A
Marex Radar	1.11	1.83	N/A
EMI Laser	1.88	1.98	N/A
Baylor Wave Staff	0.99	0.12	N/A
S4ADW Current Meter	0	0	-11.5

3.2 Structure of Database

From the 5 months of nearly continuous measurements, approximately 120-hour wave records were selected for detailed processing. The data sets were separated into 20 minute files and can be referred to as the WACSIS Common Data Base, which provides a huge resource for us to conduct filed data analysis. The category and related number of 20-minute time series available for each sensor from these 120 selected hours are summarized in Table 3.3.

Table 3.3: Number of 20-minute time series (Prevosto, et al., 2001).

	EMILASER	MAREXSGN	SAABRNIV	VLISSING	WAVERGHR	BAYLORWS	S4PRVELO
Video (150x 20 min.)	111	129	126	149	123	129	90
High Hs (150x 20 min.)	62	140	147	150	122	140	30
Low steepness (60x 20 min.)	59	59	60	60	48	59	35
Total (360x 20 min.)	232	328	333	359	293	328	155

The data files are organized in four directories:

1) FSAMP0, corresponds to original data (without re-sampling)
2) FSAMP4, re-sampling 4Hz
3) FSAMP2, re-sampling 2Hz
4) FSAMP1, re-sampling 1Hz

The name of the files divulges the starting time of the time series in the format of yymmddhhmm, for example a name 9803051040 indicates the related series started at 10:40 on March 5, 1998.

CHAPTER IV

INTER-COMPARISON BETWEEN FIELD MEASUREMENTS

4.1 Introduction

One of the objectives of Wave Crest Sensor Inter-comparison Study (WACSIS) is to investigate the suitability and consistency of different wave sensors in measuring wave elevations. Detailed information about WACSIS can be found in Chapter III. Since wave sensors deployed by WACSIS were confined in a relative small area (about hundreds square meters), ocean waves in the vicinity of these sensors were assumed to be uniform. Hence, it is possible to conduct a deterministic analysis to examine the consistency of these sensors. The Directional Hybrid Wave Model (DHWM) has the capability to deterministically decompose and predict a directional wave field. It is able to predict the wave characteristics, such as elevation, kinematics and pressure, as a function of time based on three or more wave measurements. The prediction is hence compared in the time domain with the corresponding measurements which have not been used as input to the wave decomposition. The comparisons in this chapter show satisfactory consistency among measurements recorded by different sensors after the orientation of a current meter was corrected. The study also indicates the DHWM is an useful tool for the analysis of field measurements

4.2 Data Synchronization

Three cases were selected for the analysis of directional wave fields using the DHWM. They are respectively named 9803011020, 9803051040 and 9804131100. The sampling rate of all data sets used in this study is 2 Hz. The reasons for selecting these cases are: 1) relatively steep waves were recorded, and 2) most sensors were functioning simultaneously. The peak period and significant wave height of the three cases are summarized in Table 4.1.

Table 4.1: Wave characteristics of selected cases.

Cases	$H_{1/3}$	T_p	Wave Direction at the Peak
9803011020	2.648 m	7.1 sec	3.69°
9803051040	3.786 m	8.3 sec	-12.44°
9804131100	3.064 m	10.5 sec	-35.15°

The phase differences of wave characteristics recorded at different locations are the key information for determining the directions of waves. Hence, it is necessary to make sure that the sampling of different sensors started at the same time. According to linear wave theory, wave elevation, pressure and horizontal velocity of a regular wave train should be in phase if the corresponding sensors are located at the same horizontal coordinates. Because two horizontal velocity components and pressure recorded by S4ADW were at the same horizontal coordinates, these measurements were expected to have the same phase and hence were selected for the test of data synchronization.

First, the mean-value of measured particle velocities and pressure, that is, the current velocity and hydrostatic pressure, were subtracted from the related measurements. Then the dynamic pressure head and velocities were compared to examine whether these measurements were synchronized, that is, whether the start time of sampling was the same. All three cases were examined following the same procedure. For brevity, only the test of Case 9804131100 is presented.

Time series of measured wave pressure and x-direction horizontal velocity are compared in Figure 4.1. The reason for choosing the x-direction horizontal velocity for the comparison is that the dominant wave direction is close to the x-direction. Examining by the naked eye, one finds there is some phase shift. By using trial and error, it is found that if the velocity data are shifted 0.5s ahead, the phases of the two series match better than before the shift, as shown in Figure 4.2.

Furthermore, the synchronization of measured pressure head and x-direction horizontal velocity was examined by comparing the initial phase of the wave components of relatively large amplitude. Using the Fast Fourier Transfer (FFT), the initial phases of the pressure head and velocity components were computed. It is known that the contribution from nonlinear wave-wave interaction is mainly to the frequency ranges much higher or lower than the spectral peak frequency (Zhang, et al. 1996). Hence, the comparison of the initial phases of the wave components located near the spectral peak based on linear wave theory is valid. Figure 4.3 is the power spectrum plot for Case 9804131100 and Figure 4.4 shows that the initial phases of wave components containing significant energy are almost the same after shifting one time step, 0.5s. We also selected four wave components of large energy to compare the initial phases of corresponding pressure head and velocity. Table 4.2 lists the amplitude and initial phase of the four wave components. The differences in the initial phases between pressure head and velocity are small in comparison with the related phase shift of one time step. All above comparisons indicate that the initial phases of velocity and pressure are almost identical for the major wave components after shifting one time step. In other words, the data is synchronized after shifting. The synchronized data set recorded by S4ADW was then used as the input to the DHWM for the decomposition.

The synchronization of measurements recorded by EMI laser, Baylor staff, and SAAB radar was examined with respect to those by S4ADW. Since these sensors were not located at the same location, the synchronization of these records was achieved by

comparing the phase delays of the free wave (at the spectral peak) between the measurements recorded by these sensors. The time shift made in these time series with respect to that of S4ADW is summarized in Table 4.3.

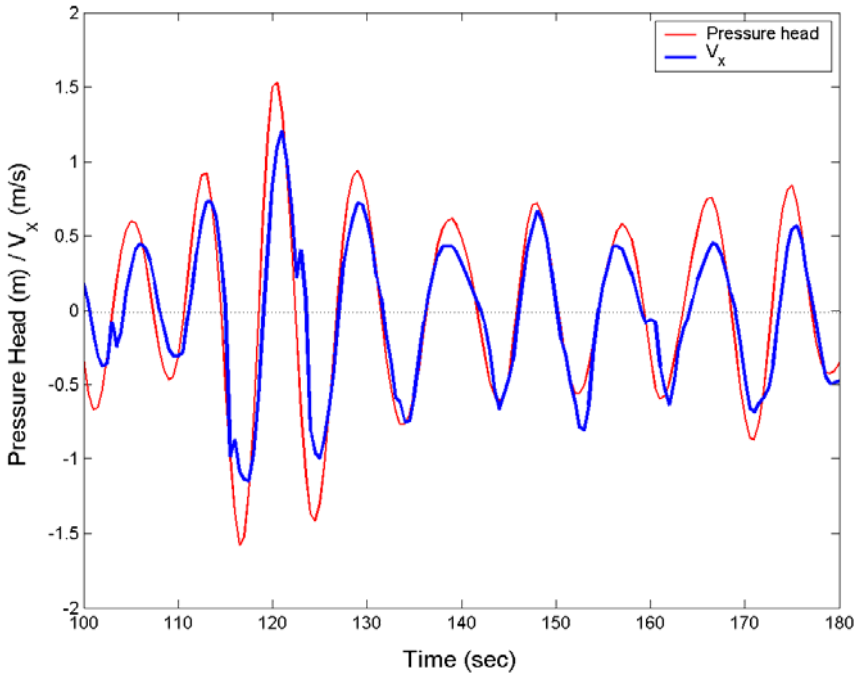

Figure 4.1: Time series of pressure and *Vx* (before shifted)

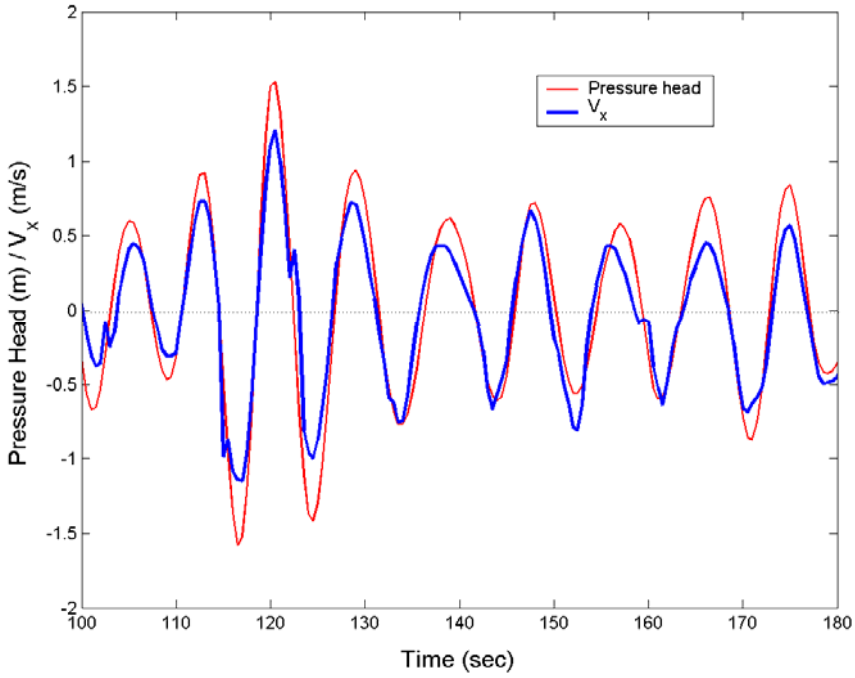

Figure 4.2: Time series of pressure and *Vx* (after shifted)

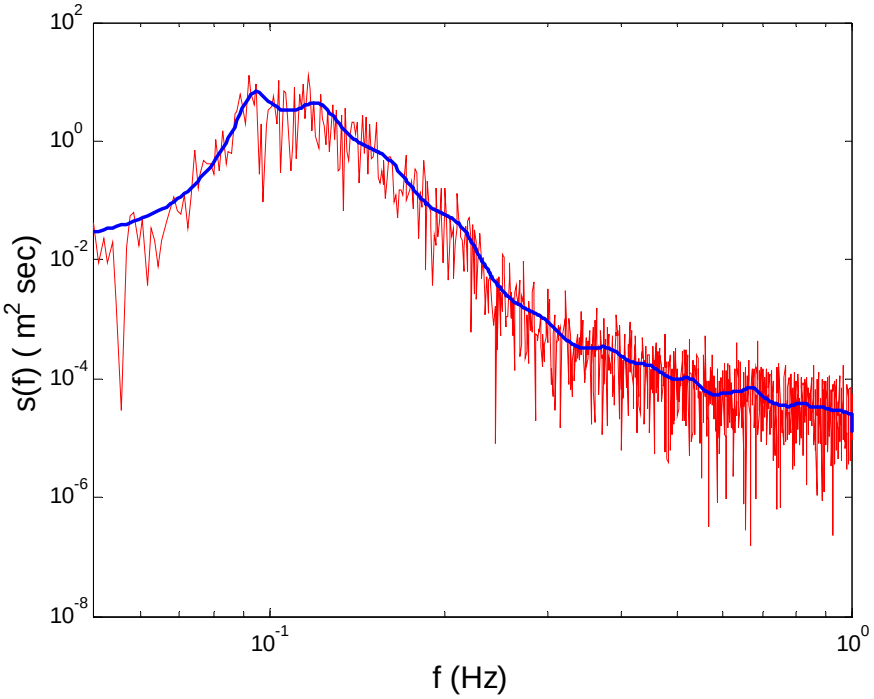

Figure 4.3: Power spectrum of pressure

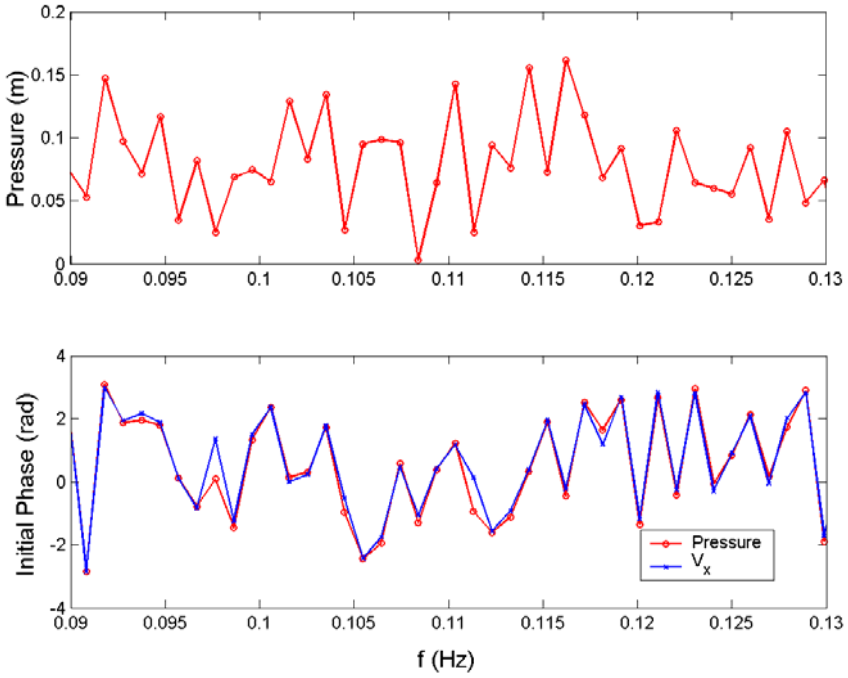

Figure 4.4: Initial phases of pressure and velocity

Table 4.2: Comparison of initial phases.

f (Hz)	Amplitude		Initial Phase	
	P (m)	*Vx* (m/s)	*P* (rad)	*Vx* (rad)
0.092	0.1472	0.1091	3.0893	2.9686
0.104	0.1344	0.0928	1.7120	1.7754
0.110	0.1424	0.1104	1.2275	1.1629
0.114	0.1559	0.1035	0.3355	0.3942

Table 4.3: Time shift of wave elevation respect to wave pressure.

Cases	Sensors		
	EMI	Baylor	SAAB
9803031020	0 sec	-0.57 sec	-2 sec
9803051040	N/A	N/A	N/A
9804131100	0.94 sec	0.35 sec	0.39 sec

4.3 Predictions Using DHWM and Their Comparison with Measurements

The data sets recorded by S4ADW, namely time series of wave dynamic pressure and two horizontal velocity components, are referred to as the S4 data set and used as the input to the DHWM for the decomposition of a measured directional wave field. It was found that measured wave fields selected in this study narrowly spread about a main direction at each discrete frequency over the majority of the frequency domain. It was then assumed that at each discrete frequency there was only one directional free wave. However, at different frequencies, the directions of free waves were usually different. After decomposition, the direction, amplitude and initial phase of free waves were used to predict wave characteristics.

4.3.1 Case 9803011020

To examine the wave directions obtained using the DHWM based on the S4 data set, they were compared with the corresponding main wave directions obtained from the measurements of the Waverider Buoy in Figure 4.5. Although the two measurements were made about one kilometer apart, it was expected the two sets of predicted wave directions should be close. However, the comparison shows an almost constant difference (about 45°) over the entire frequency range between the two sets of wave

directions. Furthermore, the wave directions obtained using the DHWM in the other two cases (9803051040 and 9804131100), which will be described later, also show the same constant difference from the corresponding results of the Waverider Buoy. Therefore, we suspected that the S4ADW might be different from the direction originally reported by the sensor installation team.

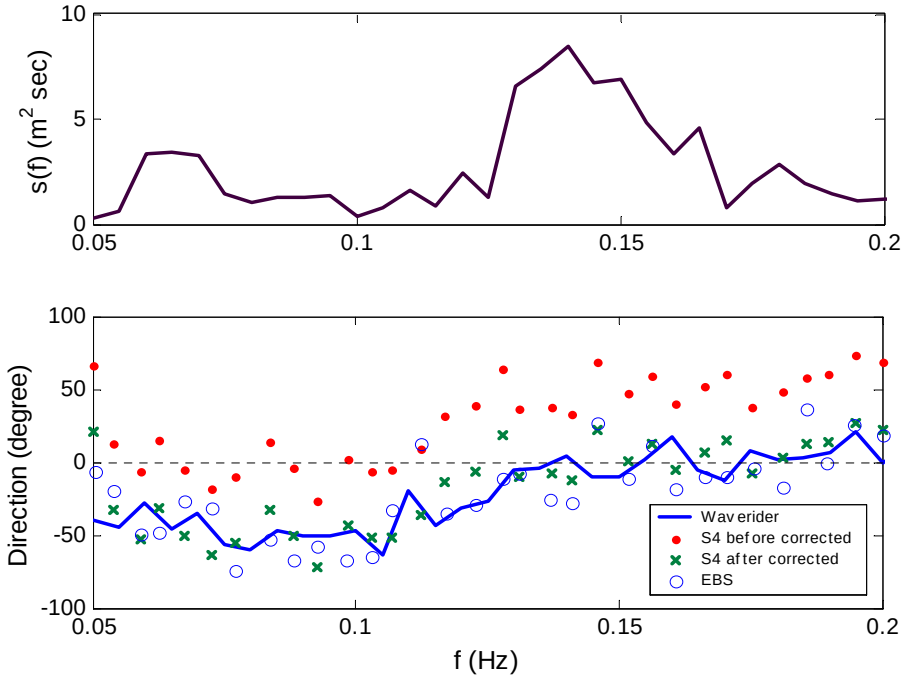

Figure 4.5: Free-wave directions of Case 9803011020

To substantiate our suspicion, the corresponding elevation data set recorded by the EMI, Baylor, and SAAB (later named as EBS data set) was used as the input to the DHWM. The wave directions based on the decomposition of the EBS data set are also plotted in Figure 4.5. The comparison shows the results based on the EBS data were very close to

those from the Waverider Buoy and had an almost constant difference (45°) from those based on the S4 data set. The comparison shows that the wave directions based on the EBS data set are in excellent agreement with those based on the S4 data set after the orientation of S4ADW is rotated 45° clockwise. These observations confirm our suspicion that the true orientation of S4ADW is about 45° clockwise from that originally reported. The consistency shown in the comparison also indirectly confirms the synchronization of the EBS data set.

The correction in the orientation of S4ADW is further examined by comparing the predicted and measured wave elevations. Based on the free waves obtained from the decomposition of the S4 data set, the DHWM was used to predict the wave elevation at the locations of the Marex and SAAB radars. It should be noted that these two wave records were not used in the decomposition of the S4 data set. If the free-wave directions are correct, the prediction should match the measurements of Marex and SAAB. Figure 4.6 and Figure 4.7 show the comparisons between the measurements and the corresponding predictions before and after the free wave directions are rotated by 45° . It is observed that the prediction based on the corrected directions matches the measurement substantially better. The satisfactory agreement between the predictions based on the corrected directions and measurements also indicates that the measurements recorded by S4ADW, Marex and SAAB are consistent. It is noticed that the prediction at the location of Marex matches the corresponding measurements better than that at the location of SAAB. This is expected because SAAB was located farther away from S4ADW and the prediction error increases with the increase of the prediction distance.

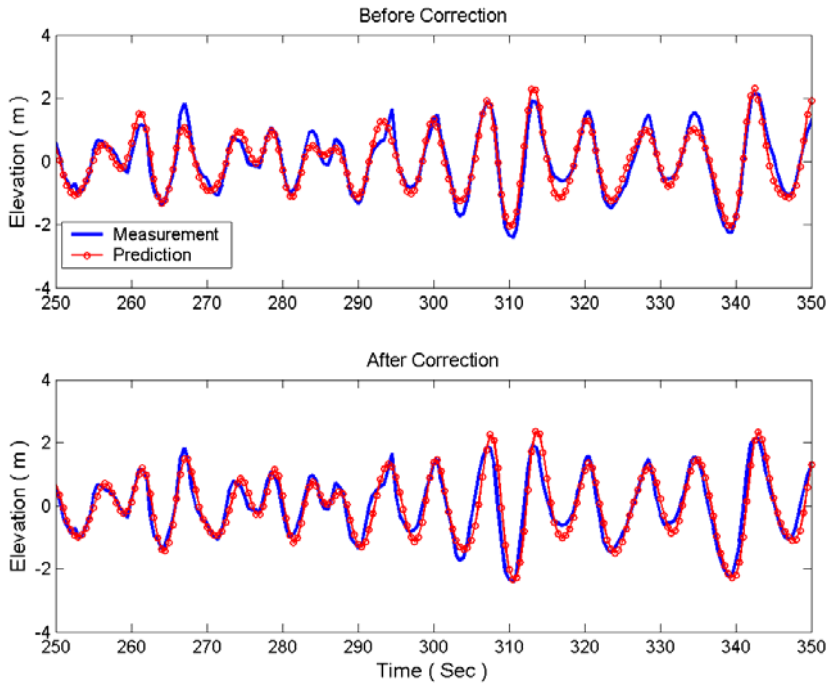

Figure 4.6: Comparison between elevations at Marex (9803011020)

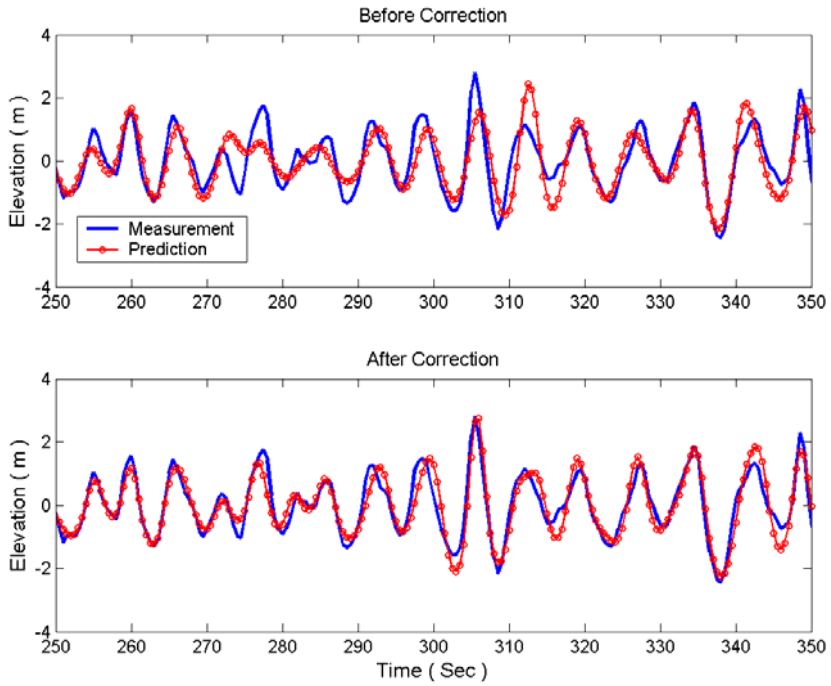

Figure 4.7: Comparison between elevations at SAAB (9803011020)

Conversely, the free waves obtained based on the decomposition of the EBS data set can be used to predict the pressure and horizontal velocity at the location of S4ADW. The predicted and measured wave pressures at S4ADW are in excellent agreement, as shown in Figure 4.8. The agreement is better than that between predicted and measured elevation at either Marex or SAAB (Figure 4.6 and Figure 4.7), which is also expected. Because measured pressure and horizontal velocity were made at 11.5 m below the still water level, the contributions from high-frequency free waves were insignificant at deep depth. As a result, the ratio of noise to signal in the measured pressure or horizontal velocity was relatively high and the results of high-frequency free waves based on the decomposition of these measurements usually involved significant errors. Consequently, the predicted wave elevation contributed by high-frequency free waves also involved significant errors. Figure 4.9 shows the predicted x-direction velocity compared with the corresponding measurements with or without the direction correction. It clearly shows that the agreement between the prediction and measurement rotated by 45° clockwise is much better.

4.3.2 Case 9803051040

The directions of free waves were calculated using the DHWM based on the S4 data set. They are compared with the results from the Waverider Buoy in Figure 4.10. Because the corresponding measurements of Marex, EMI, and Baylor are not available in Case 9803051040, only the elevation at SAAB was predicted and is compared with the measurement in Figure 4.11. Similar phenomena were observed in these Figures and the same conclusion about the true orientation of S4ADW was reached.

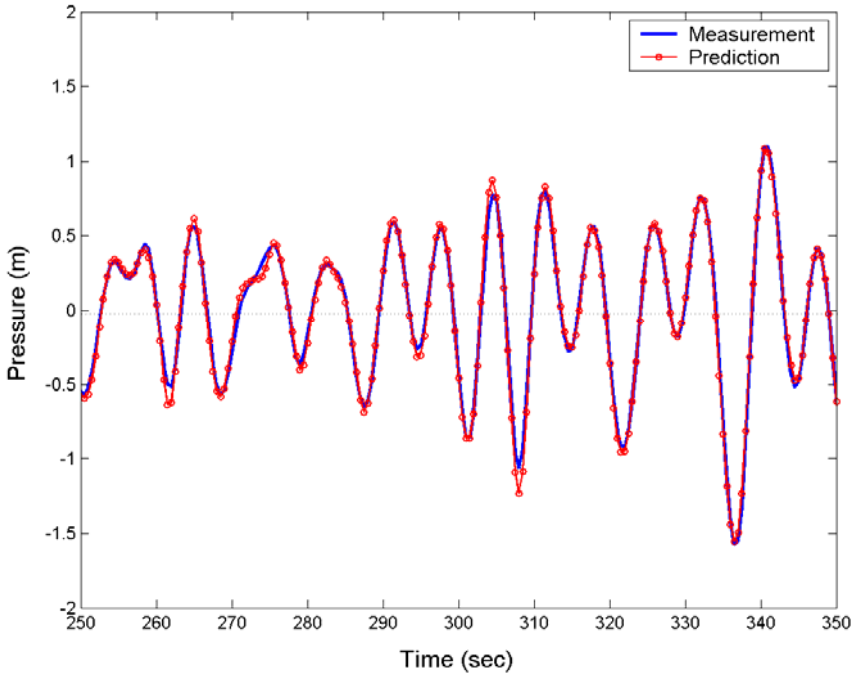

Figure 4.8: Comparison between pressures at S4ADW (9803011020)

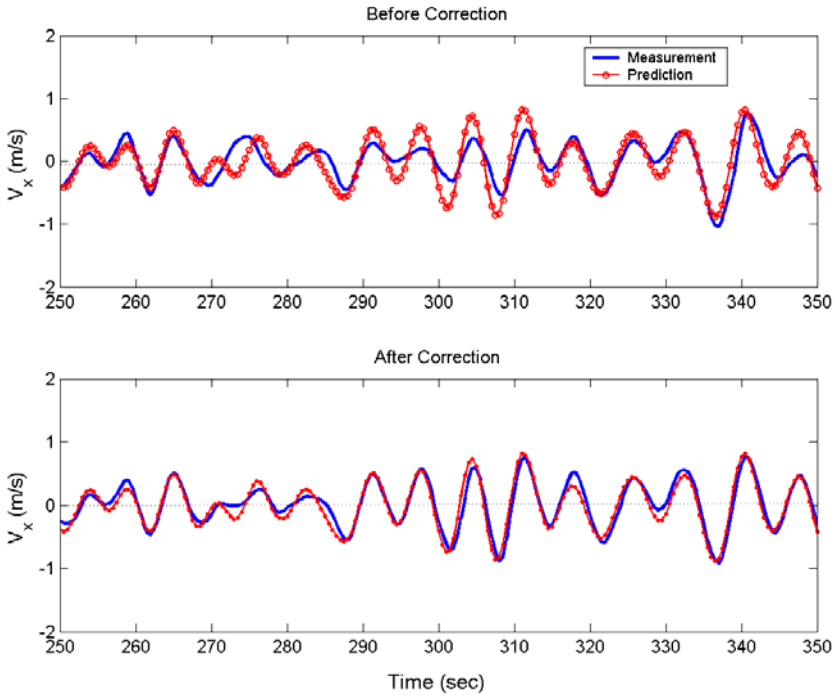

Figure 4.9: Comparison between *Vx* at S4ADW (9803011020)

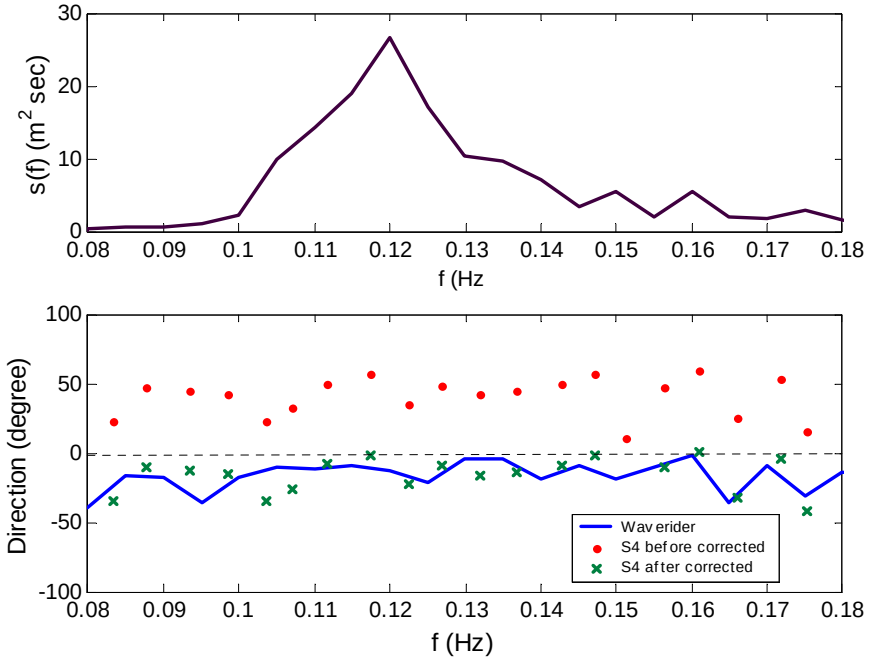

Figure 4.10: Free-wave directions of Case 9803051040

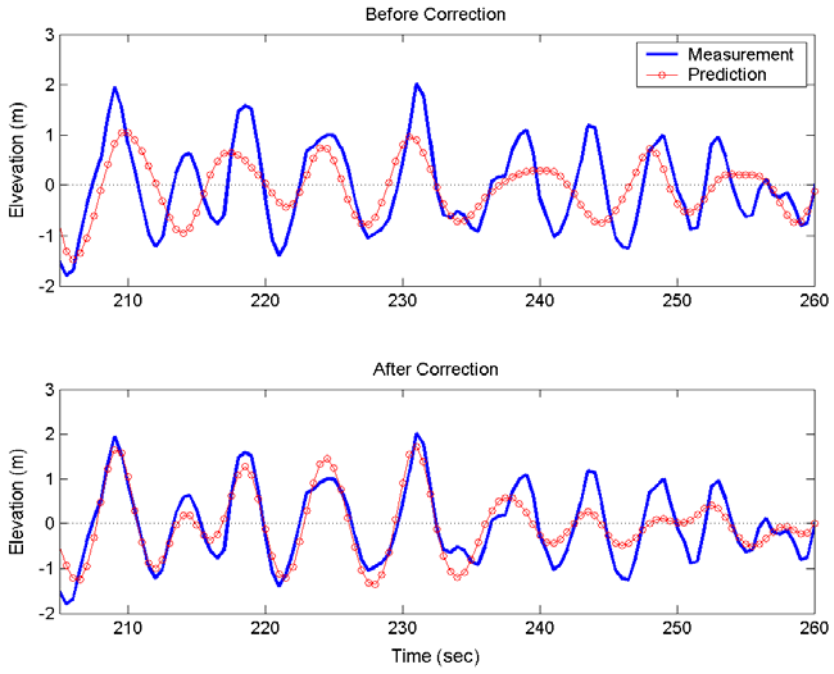

Figure 4.11: Comparison between elevations at SAAB (9803051040)

4.3.3 Case 9804131100

The directions of free waves were obtained using DHWM based on the S4 data and EBS data respectively. They are compared with the results of the Waverider Buoy in Figure 4.12. There also exists a 45° difference over the entire frequency range between the record of the Waverider Buoy and the wave direction based on the S4 data. After the orientation of the S4ADW rotating by 45°, the results match those of the Waverider Buoy and especially those of the EBS data set very well.

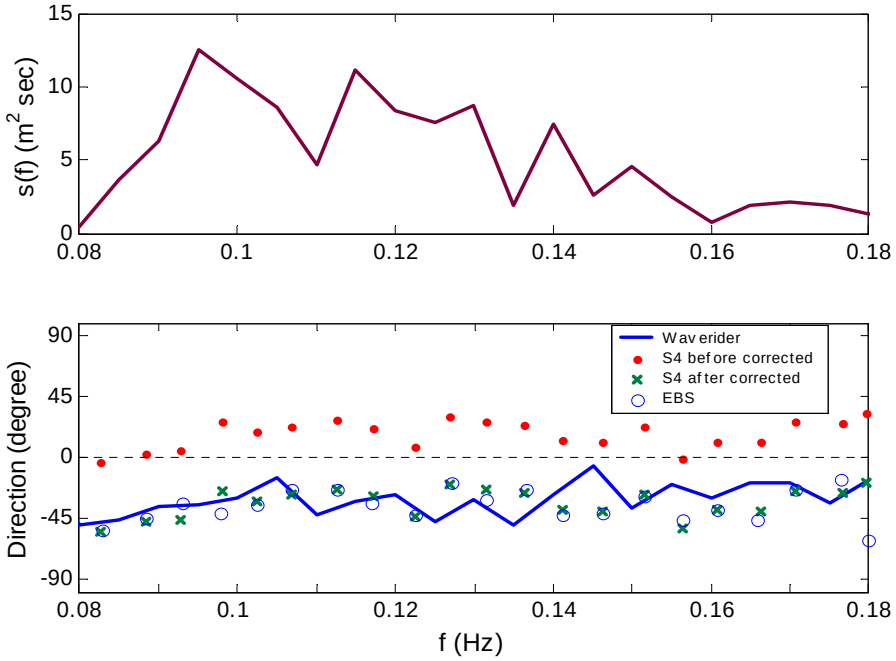

Figure 4.12: Free-wave directions of Case 9804131100

Figure 4.13 and Figure 4.14 show the comparisons between the predicted and the measured wave elevation at Marex and SAAB, respectively. The trends observed in these two Figures are similar to those in the previous two cases. The comparison between predicted and measured pressure at S4ADW is shown in Figure 4.15 and that

between predicted and measured x-direction velocity at S4ADW in Figure 4.16. Observations made in these two figures are similar to those in Case 9803011020. They all confirm that the original orientation of the S4ADW was mistaken by 45° and the measurements recorded by different sensors are in satisfactory agreement.

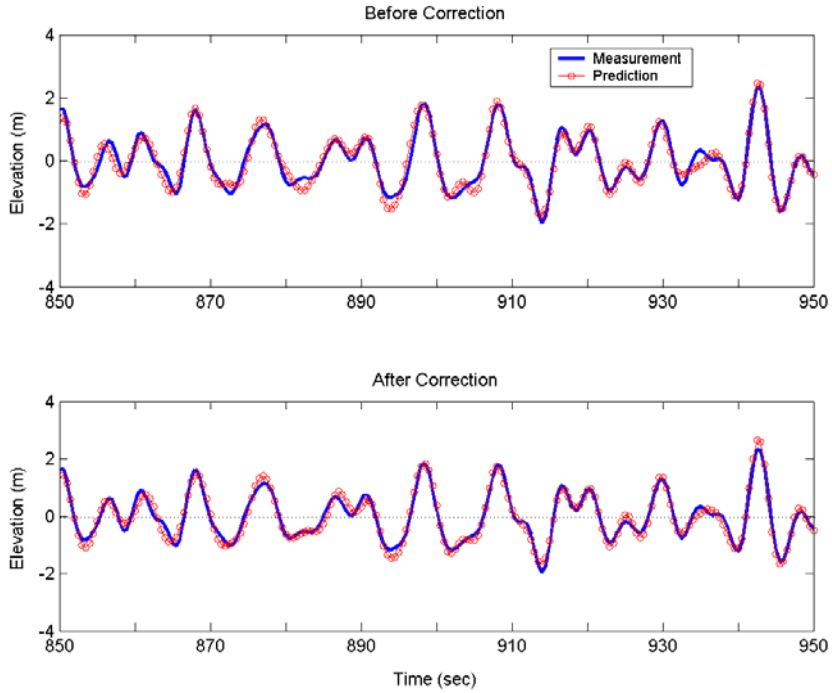

Figure 4.13: Comparison between elevations at Marex (9804131100)

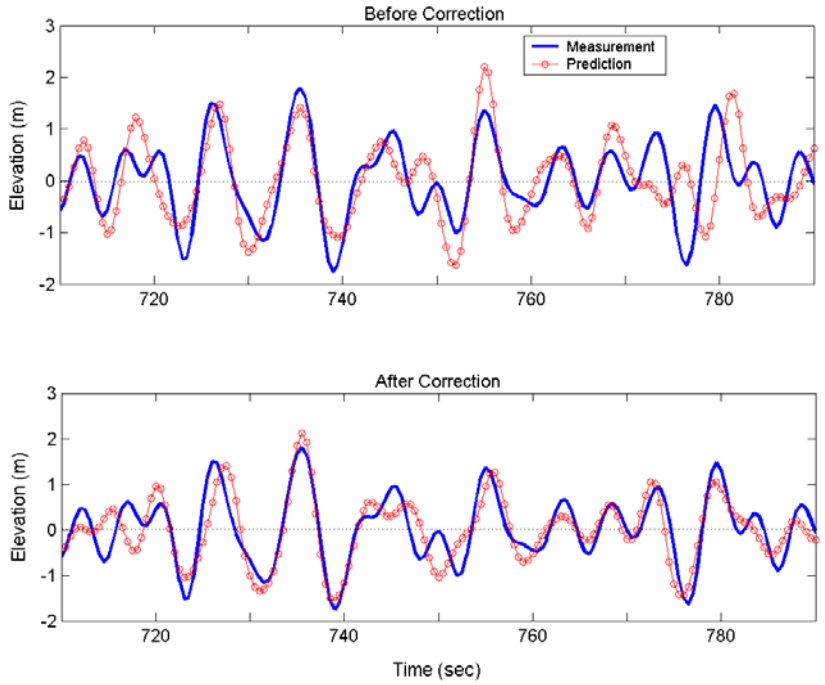

Figure 4.14: Comparison between elevations at SAAB (9804131100)

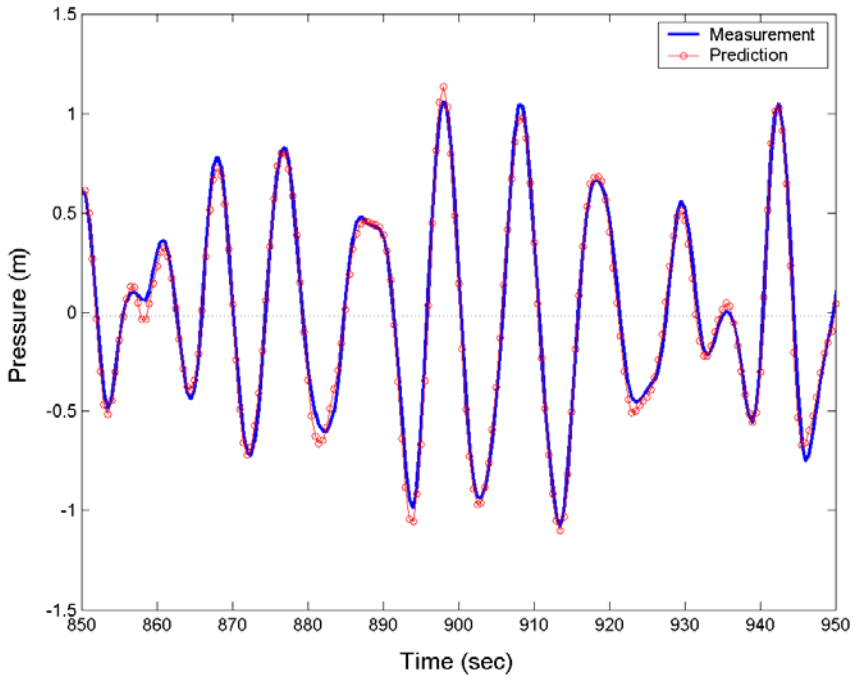

Figure 4.15: Comparison between pressures at S4ADW (9804131100)

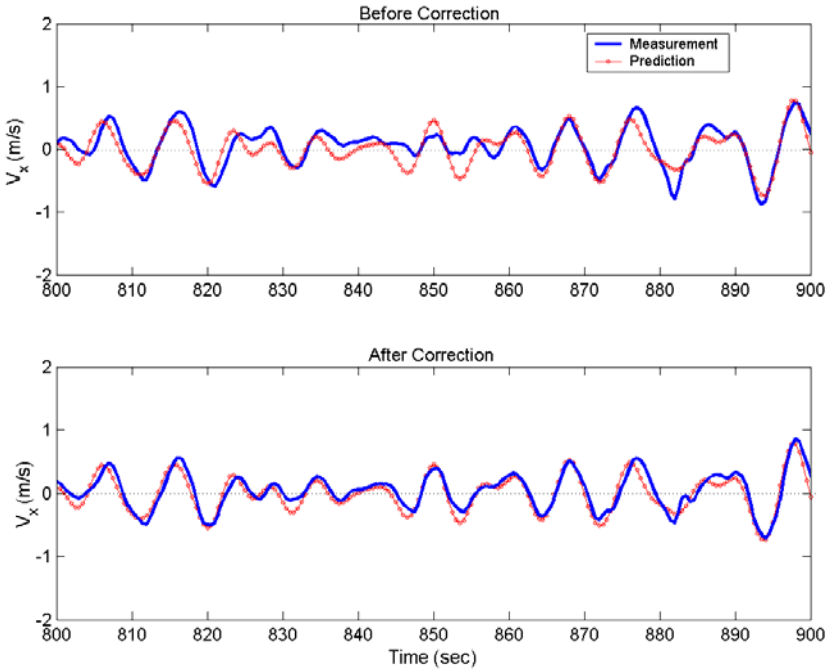

Figure 4.16: Comparison between *Vx* at S4ADW (9804131100)

CHAPTER V

ANALYSIS OF DIRECTIONAL WAVE FIELDS WITH STRONG CURRENT

5.1 Introduction

The Directional Hybrid Wave Model (DHWM) developed by Zhang et al. (1999a) is capable of decomposing a directional irregular wave field into its free waves based on three or more wave records. Knowing these free waves, it is able to predict wave properties deterministically in the vicinity of measurements (Zhang et al., 1999b&c). This chapter aims at extending the original DHWM to allow for the analysis of directional ocean waves in the presence of strong currents. Assuming that currents are uniform and steady and following the derivation of Zhang et al. (1999a), the solutions truncated at second order in wave steepness for directional wave interaction in the presence of steady and uniform currents were derived using two different perturbation methods to ensure rapid convergence. The numerical scheme for the extended DHWM is similar to that of the original DHWM except for the addition of iterations to determine the intrinsic frequency of each free wave component based on the corresponding apparent frequency, velocity of currents, and initially guessed wave direction.

Various numerical tests were conducted to ensure the reliability and convergence of the extended DHWM and it was then applied to the analysis of three cases of filed measurements selected from the database of the Wave Crest Sensor Inter-comparison Study (WACSIS). The comparison between the results obtained respectively using the extended and original DHWM demonstrates the Doppler effect of currents on the wave decomposition.

5.2 Governing Equations and Solutions

5.2.1 Governing Equations for Directional Wave with Current

In the presence of uniform and steady currents, the governing equation and boundary conditions for an irregular wave field are given below in the Cartesian coordinates with the *z*-axis pointing upwards.

$$\nabla^2\phi = 0 \tag{5.1}$$

$$\nabla\phi \to 0 \quad z \to -\infty, \quad \text{or } \frac{\partial\phi}{\partial z} = 0 \quad \text{at } z = -h. \tag{5.2}$$

$$\frac{\partial\phi}{\partial z} = \frac{\partial\eta}{\partial t} + (\nabla_h\phi + \vec{U})\cdot\nabla_h\eta, \text{ at } z = \eta \tag{5.3}$$

$$\frac{\partial\phi}{\partial t} + \frac{1}{2}\left|\nabla\phi + \vec{U}\right|^2 + g\eta = C(t), \text{ at } z = \eta \tag{5.4}$$

where, $\vec{U}$ is the velocity vector of currents

$$\vec{U} = u_x\vec{i} + u_y\vec{j} \tag{5.5}$$

and u_x and u_y are its *x*- and *y*- components. Compared Eqs. (5.1) – (5.4) with the governing equation and boundary conditions defined in Chapter 2 for an irregular wave field without current, they are similar except the inclusion of $\vec{U}$ in free surface boundary conditions, i.e. Eqs. (5.3) and (5.4).

To solve Eqs. (5.1) – (5.4) for the potential and elevation of a directional wave field in the presence of uniform and steady currents, we introduce a moving Cartesian coordinates (*X*-*Y*-*Z*), which are related to the fixed coordinates through,

$$\vec{X} = X\vec{i} + Y\vec{j} = (x - u_x t)\vec{i} + (y - u_y t)\vec{j} = \vec{x} - \vec{U}t \tag{5.6}$$

$$Z = z \tag{5.7}$$

In terms of the moving coordinates, the governing equation and boundary conditions reduce to the same form as those in the absence of current except for a difference in the Bernoulli constant which affects the computation of static pressures. Hence, the solutions in terms of the moving coordinates for an irregular wave field in the presence of the current are the same as those given in Chapter II. After transforming the variables back to those in the fixed coordinates, we can obtain the truncated solutions up to second order in wave steepness for the interaction between two free waves using two different perturbation methods, respectively, i.e., using MCM for the interaction between a pair of free waves of relatively close frequencies and PMM for those of quite different frequencies.

5.2.2 Conventional Perturbation Method Solutions:

$$\begin{aligned}\phi = \sum_{j=1}^{2}\left\{\frac{a_j g}{\sigma_{I,j}}\frac{\cosh\left[k_j\left(h+z\right)\right]}{\cosh\left(k_j h\right)}\sin\psi_j + \frac{3}{8}\frac{a_j^2\sigma_{I,j}\cosh\left[2k_j(h+z)\right]}{\sinh^4\left(k_j h\right)}\sin 2\psi_j\right\} \\ + \frac{a_1 a_2 \sigma_{I,2}}{2} A_{(-)}\frac{\cosh\left[\left|\vec{k}_1-\vec{k}_2\right|\left(h+z\right)\right]}{\cosh\left[\left|\vec{k}_1-\vec{k}_2\right|h\right]}\sin(\psi_1-\psi_2) \\ + \frac{a_1 a_2 \sigma_{I,2}}{2} A_{(+)}\frac{\cosh\left[\left|\vec{k}_1+\vec{k}_2\right|\left(h+z\right)\right]}{\cosh\left[\left|\vec{k}_1+\vec{k}_2\right|h\right]}\sin(\psi_1+\psi_2)\end{aligned} \tag{5.8}$$

Where

$$\psi_j = \overrightarrow{k_j}\cdot\overrightarrow{X} - \sigma_{A,j}t + \delta_j \tag{5.9}$$

$$A_{(\mp)} = \mp\frac{k_2\left[2\lambda\left(1\mp\lambda\right)\left(\Gamma\alpha_1\alpha_2 \pm 1\right)\mp\lambda^3\left(\alpha_1^2-1\right)+\alpha_2^2-1\right]}{k_2\left(1\mp\lambda\right)^2-\alpha_2\left|\overrightarrow{k_1}\mp\overrightarrow{k_2}\right|\tanh\left(\left|\overrightarrow{k_1}\mp\overrightarrow{k_2}\right|h\right)} \tag{5.10}$$

$$\lambda = \frac{\sigma_{I,1}}{\sigma_{I,2}} \tag{5.11}$$

$a_j, k_j,$ and δ_j represent the amplitude, wavenumber, and initial phase of the *j*th wave component. α_j and Γ have the same definitions as Eq. (2.8) and (2.10). $\sigma_{I,j}$ and $\sigma_{A,j}$ are the intrinsic frequency and apparent frequency, respectively. They satisfy

$$\sigma_{A,j} = \sigma_{I,j} + \vec{U} \cdot \vec{k}_j \tag{5.12}$$

By default, we define that a smaller subscript *j* indicates a free wave of lower frequency, i.e. $\sigma_{I,2} > \sigma_{I,1}$. It should be noted that the apparent frequency is only contained in the linear phase ψ_j.

$$\begin{aligned}\eta = \sum_{j=1}^{2}\left\{ a_j \cos\theta_j + \frac{a_j^2\sigma_j^2}{4g}\left[2 + \frac{3\cosh(2k_j h)}{\sinh^4(k_j h)} - \frac{1}{\sinh^2(k_j h)} \right]\cos 2\psi_j \right\} \\ + \frac{a_1 a_2 k_2}{2\alpha_2}\left[-(1-\lambda) A_{(-)} + M_{(-)} \right]\cos(\psi_1 - \psi_2) \\ + \frac{a_1 a_2 k_2}{2\alpha_2}\left[(1+\lambda) A_{(+)} + M_{(+)} \right]\cos(\psi_1 + \psi_2)\end{aligned} \tag{5.13}$$

where,

$$M_{(\mp)} = \lambda^2 + 1 - \lambda(\Gamma\alpha_1\alpha_2 \pm 1) \tag{5.14}$$

5.2.3 Phase Modulation Method Solutions

The effects of a short wave on a long free wave are of third order in wave steepness and the solution for a long free wave up to the second order is the same as that of a single

Stokes wave train. Hence, only the potential and elevation of a modulated short free wave are given below.

$$\phi_3 = \frac{a_3 g}{\sigma_{I,3}} e^{k_3(z+f_k)} \sin\left(\psi_3 + k_3 f_{\psi,\phi}\right) \tag{5.15}$$

$$\eta_3 = a_3\left(1+ f_a\right)\cos\left(\psi_3 + k_3 f_{\psi,\eta}\right) + \frac{1}{2} k_3 a_3^2 \cos\left[2\left(\psi_3 + k_3 f_{\psi,\eta}\right)\right] \tag{5.16}$$

where,

$$f_k = a_1 \cos\psi_1 \left[B_{(-)} e^{\left(\left|\bar{k}_3 - \bar{k}_1\right| - k_3\right)z} - B_{(+)} e^{\left(\left|\bar{k}_3 + \bar{k}_1\right| - k_3\right)z} \right] \tag{5.17}$$

$$f_{\psi,\phi} = -a_1 \sin\psi_1 \left[B_{(-)} e^{\left(\left|\bar{k}_3 - \bar{k}_1\right| - k_3\right)z} + B_{(+)} e^{\left(\left|\bar{k}_3 + \bar{k}_1\right| - k_3\right)z} \right] \tag{5.18}$$

$$f_a = a_1 k_3 \cos\psi_1 \left[\left(B_{(-)} - B_{(+)}\right) - \lambda\left(B_{(-)} + B_{(+)}\right) - \lambda\alpha_1\Gamma + \lambda^2 + 1 \right] \tag{5.19}$$

$$f_{\psi,\eta} = -a_1 \sin\psi_1 \left[\left(B_{(-)} + B_{(+)}\right) - \lambda\left(B_{(-)} - B_{(+)}\right) - \lambda \right] \tag{5.20}$$

$$B_{(-)} = \frac{\lambda\left(1-\lambda\right)\left(1+\alpha_1\Gamma\right) - \frac{\lambda^3}{2}\left(\alpha_1^2 - 1\right)}{\left(1-\lambda\right)^2 - \sqrt{1 - 2\lambda^2\Gamma\alpha_1 + \lambda^4\alpha_1^2}} \tag{5.21}$$

$$B_{(+)} = \frac{\lambda\left(1+\lambda\right)\left(1-\alpha_1\Gamma\right) - \frac{\lambda^3}{2}\left(\alpha_1^2 - 1\right)}{\left(1+\lambda\right)^2 - \sqrt{1 + 2\lambda^2\Gamma\alpha_1 + \lambda^4\alpha_1^2}} \tag{5.22}$$

Subscripts *1* and *3* denote the long and short free wave, respectively.

In comparing the above solutions with the corresponding solutions in the absence of currents given in Chapter 2, we found that they are virtually identical except for the frequencies involved in the phases (ψ_j for $j = 1 \sim 3$). That is, in the presence of currents

the frequencies involved in the phases are the apparent frequencies instead of intrinsic frequencies as in the absence of currents.

The wave induced horizontal particle velocities and dynamic pressure can be obtained through

$$u = \frac{\partial \phi}{\partial x};\ v = \frac{\partial \phi}{\partial y} \tag{5.23}$$

and Bernoulli equation

$$-\frac{p}{\rho g} = \frac{1}{g}\frac{\partial \phi}{\partial t} + \frac{1}{2g}\nabla^2 \phi + z - C(t), \tag{5.24}$$

respectively based on the corresponding MCM or PMM solutions of ϕ. They are listed in Appendix A. Noticing that the solutions truncated at second order in wave steepness involve at most two distinct free waves, we may straightforwardly extend the above solutions to allow for more than two free waves involved in a directional wave field. The extended solutions for multiple free wave components are given in Appendix B.

5.3 Numeric Scheme of C-Directional Hybrid Wave Model

Similar to the original DHWM, the extended DHWM (named as C-DHWM hereinafter) consists of two parts: decomposition and prediction (superposition). Given the velocity of currents, the decomposition is to retrieve the free waves consisting of a directional wave field based on three or more resultant wave property records. The iterative procedure in the decomposition of the C-DHWM also involves three fundamental steps: wave direction and amplitude estimation, initial phase optimization, and computation of nonlinear wave-wave interactions and their subtraction from the measurements. The flow chart of the decomposition is sketched in Figure 5.1.

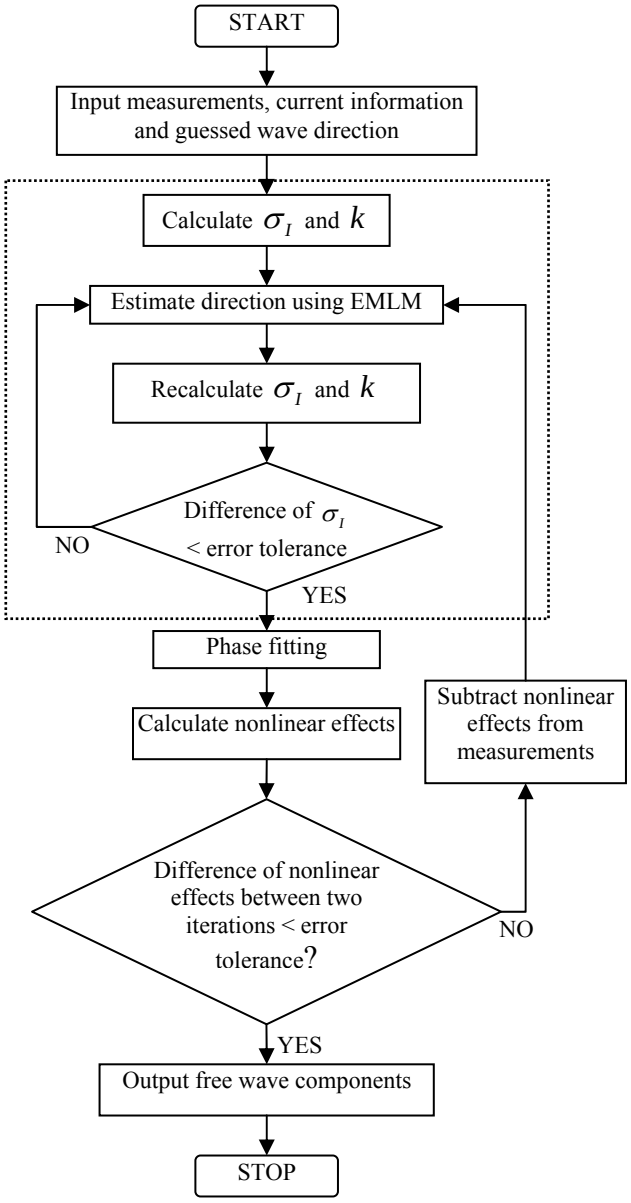

Figure 5.1: Flow chart of decomposition part of C-DHWM

The key difference between a C-DHWM and an original DHWM (referred to as DHWM) is in the computation of the wavenumber vector of free waves. In the decomposition of a

DHWM, a discrete frequency resulting from the Fast Fourier Transfer (FFT) of a wave record is considered as an intrinsic frequency and the magnitude of the corresponding wavenumber is obtained following the dispersion relation. In the presence of currents, a discrete frequency given by the FFT is the apparent frequency. For computing the related intrinsic frequency, we need to know the corresponding wavenumber vector while the computation of the magnitude of wavenumber needs the intrinsic frequency. Therefore, the calculation of an intrinsic frequency and wavenumber vector is accomplished through iterations in a C-DHWM. Initially, the magnitude of a wavenumber is approximately calculated based on the corresponding apparent frequency using the dispersion relation. Based on a guessed wave direction and approximate magnitude of the wavenumber, the related intrinsic frequency is approximately calculated using Eq. (5.12) and then the magnitude of a wavenumber is re-calculated based on the newly computed intrinsic frequency. When the difference in the magnitudes of the intrinsic frequency obtained respectively from two consecutive iterations is smaller than a prescribed error tolerance, the approximate magnitude of the wavenumver is used to determine directional spreading of wave energy based on the cross spectra of resultant wave properties using a Maximum Likelihood Method (MLM) (Isobe et al., 1984). Based on the computed direction of free waves, an intrinsic frequency is calculated again and so is the magnitude of the corresponding wavenumber. The difference between the magnitudes of an intrinsic frequency computed respectively before and after the determination of the wave direction is examined again. If it is smaller than a prescribed error tolerance, then the decomposition proceeds to the next step, otherwise the newly computed wavenumber is employed to re-calculate the wave energy spreading using a MLM.

After the amplitude, intrinsic frequency and direction of individual free waves are obtained, the rest steps of decomposition, i.e. initial phase optimization and computation of nonlinear wave-wave interactions and their subtraction from the measurements, are similar to the corresponding ones in DHWM which is described in Chapter II.

While the decomposition of a directional irregular wave field employs an iterative numerical scheme, the prediction part of C-DHWM can be accomplished straightforwardly. Given the information of free waves and currents, resultant wave properties at a given location can be obtained by superposing the corresponding properties of free waves and nonlinear interactions among them.

5.4 Numeric Verification

Before applying C-DHWM to real wave data, numeric verification was conducted to ensure that its numeric scheme is reliable and especially the iterative procedures of the decomposition are convergent. It had been shown in the previous study (Zhang, et al. 1999a) that the iterative procedures of decomposing a directional wave field in the absence of currents were convergent. Therefore, our numerical tests focus on the convergence of computing the intrinsic frequencies by decoupling the Doppler effect from the corresponding apparent frequencies. The velocity of currents chosen in the numerical tests was 1.5 m/s, considered to be a relatively strong current in ocean environment and of course much greater than the largest current velocity recorded in the WACSIS project. The Doppler effect reaches the maximum when waves are in the same or opposite direction to the currents. Hence, we choose following and opposing currents in the numerical tests.

In each numerical test, we first simulated a directional wave field in the presence of currents using the prediction part of a C-DHWM, given the amplitude, direction, intrinsic frequency and initial phase of a set of free waves and the velocity of currents. Three resultant wave properties at given locations were then used as input to the decomposition. The sampling rate and duration of a numerical wave record are 2 Hz and 256 seconds, respectively. The decomposition of a simulated wave field may recover its free waves. The comparison between the decomposed (recovered) and given (input) free waves may divulge whether or not the numerical scheme of a C-DHWM is reliable and

convergent. To demonstrate errors caused by neglecting currents in the decomposition, the corresponding results obtained using a DHWM were also included in the comparison. To make the numerical tests more realistic, the free waves of a simulated wave field were determined based on the characteristics of field measurements. That is, the shape of the amplitude spectrum and the direction of free waves were chosen to be similar to a case selected from the WACSIS database. Because the amplitudes of free waves in all three selected cases from the WACSIS database were relatively small, in numerical tests they were magnified on purpose. The nominal wave steepness (defined as the product of one half of significant wave height and the wavenumber at spectra peak) is around 0.25 in numerical tests. The initial phases of free waves were randomly selected from 0 to 2π and the water depth is set to be 30 m.

5.4.1 Numerical Test 1: PUV Record and Following Currents

Both mean directions of the simulated wave field and current direction were set at 0°. Three different wave properties: dynamic pressure, *x*- and *y*-component velocities were simulated at the location 6 m below the still water level, resembling the field measurements recorded by a PUV sensor. At the beginning, 'guessed' directions of all free waves were set at 20°, different from their true direction by about 20° - 40°. The amplitude, direction, and initial phase of free waves obtained by decomposing simulated PUV records using a C-DHWM are compared with those input to simulate the wave field in Figure 5.2 – Figure 5.4. The free waves obtained using a DHWM (without considering currents) are plotted in Figure 5.2 and Figure 5.5. Figure 5.2 – Figure 5.4 show that the decomposed free waves obtained using a C-DHWM are virtually identical to the input free waves. The excellent agreement indicates the numerical scheme of a C-DHWM is convergent. However, the decomposed free waves obtained using a DHWM are quite different from the corresponding input free waves. Figure 5.2 shows that the amplitude spectrum obtained using a DHWM differs from that of input free waves in three aspects. First, the DHWM spectral peak shifts to a frequency higher than the input

spectrum. Secondly, the DHWM amplitude spectrum is overestimated, especially at high frequencies. Thirdly, the input free-wave spectrum has no energy above 0.22 Hz or below 0.05 Hz while the DHWM spectrum has significant energy in these high and low frequency ranges.

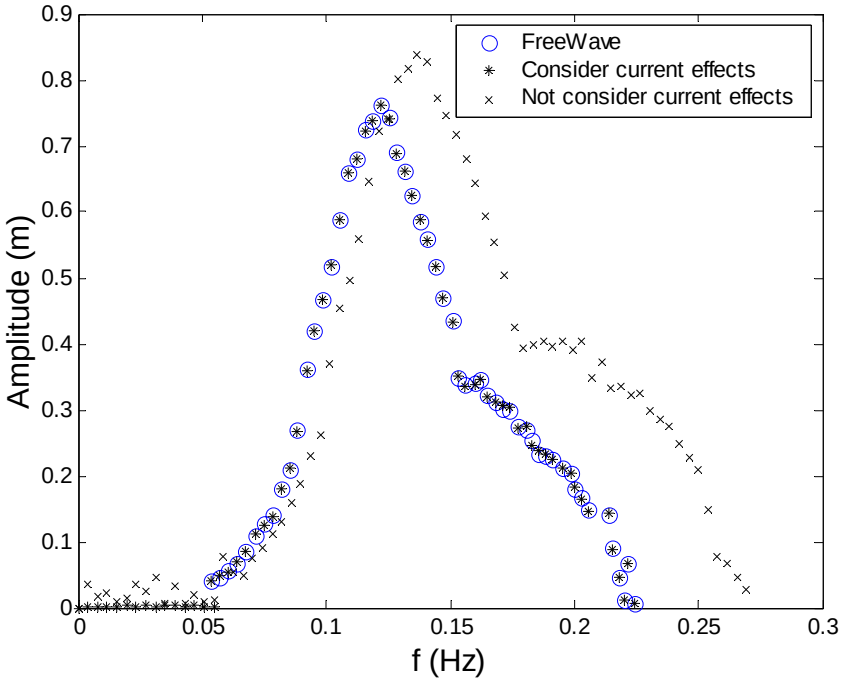

Figure 5.2: Comparison of amplitude (PUV, Following current)

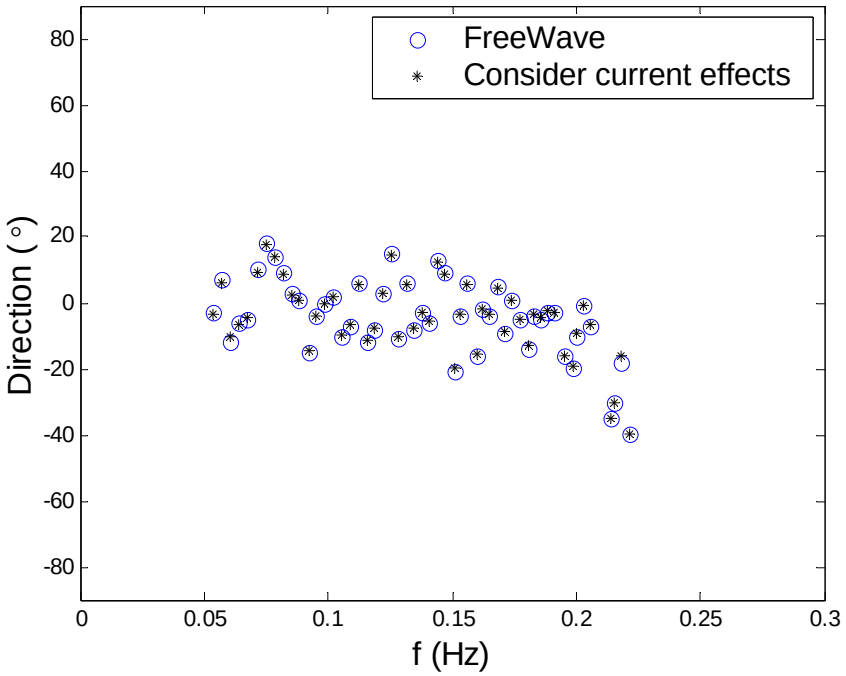

Figure 5.3: Comparison of direction (PUV, Following current)

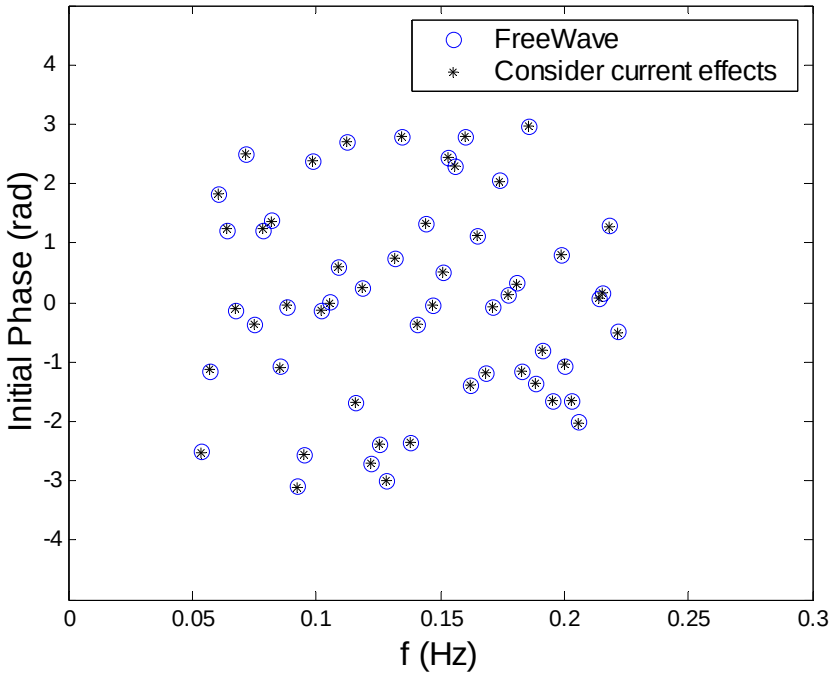

Figure 5.4: Comparison of initial phase (PUV, Following current)

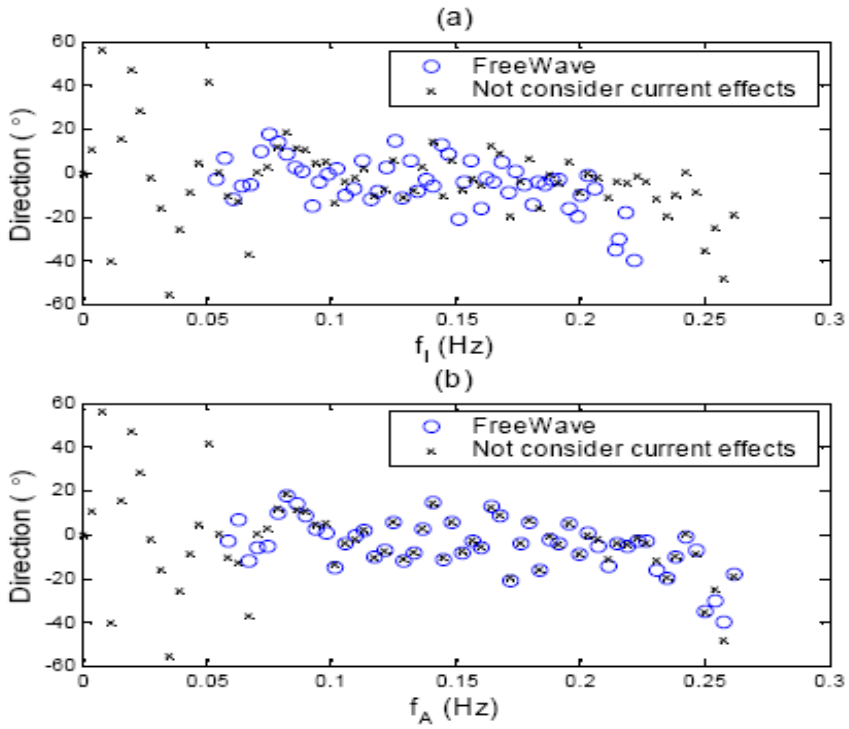

Figure 5.5: Comparison of direction in detail (PUV, Following current)

The first two differences result directly from neglecting the effect of currents. Owing to the following currents, the apparent frequency of a free wave is higher than its intrinsic frequency and the increase in the apparent frequency is greater when the intrinsic frequency is higher. Noticing that the amplitude spectrum is plotted against the intrinsic frequency in Figure 5.2, the DHWM spectrum regards the apparent frequency as the intrinsic frequency, resulting in a shift of wave energy toward higher frequencies. The magnitude of wavenumber computed in a DHWM was based on the apparent frequency and hence is greater than the 'true' wavenumber based on the intrinsic frequency. It is known that wave induced dynamic pressure and velocity decay exponentially with respect to the product of the wavenumber and the distance from the still water level to the location of the record. As a result, the transfer function (from pressure or velocities to the elevation) used in a DHWM is greatly overestimated due to the overestimated

wavenumber and the error is greater at higher frequencies. Consequently, the DHWM amplitude spectrum was greatly overestimated in the high frequency range. The third difference between the input and DHWM spectra results indirectly from neglecting currents. Because the amplitudes of free waves near the spectral peak were estimated incorrectly using a DHWM, the interaction among these free waves was also calculated incorrectly. Hence, nonlinear bound waves could not be correctly decoupled or subtracted from the corresponding resultant wave records. Consequently, the free-wave amplitudes in relatively high and low frequency ranges were incorrectly estimated.

Figure 5.5(a) shows the comparison between the directions of free waves obtained using a DHWM and those of input free waves. The main discrepancy between the two sets of wave directions results mainly from the neglect of the Doppler frequency shift. To examine the errors caused by the factors in addition to the frequency shift, both wave directions were plotted against the apparent frequency in Figure 5.5(b). It shows the two sets of wave directions are close except at relatively high and low frequency ranges. Because the three resultant wave records (PUV) used in the decomposition were recorded at the same location, the wave directions estimated using a MLM are mainly based on the ratio of the two horizontal velocities. Although linear transfer function from velocity to surface elevation was overestimated, the ratio of their transfer functions remains the same. That is why the discrepancies in wave direction excluding the frequency shift are relatively insignificant in the PUV case. The large discrepancies at relatively high and low frequencies were caused by incorrect subtraction of nonlinear wave-wave interactions from the corresponding wave records. The comparison of the input and DHWM initial phases showed similar trends as those of wave directions and is omitted for brevity.

5.4.2 Numerical Test 2: Elevation Records and Opposing Currents

The free waves input to the prediction part of a C-DHWM for simulating a numerical wave field were similar to those in the previous test except that the direction of currents

(1.5 m/s) was opposite. Wave elevations recorded at locations (0, 0), (15 m, 0), and (0, 10 m) were used as input to the decomposition. The amplitudes, directions, and initial phases of free waves obtained using a C-DHWM were compared with those of input free waves in Figure 5.6 – Figure 5.8. Similar to the previous test, in the initial iteration the 'guessed' direction of all free waves was set at 20°. The comparison in these three figures confirms the decomposed free waves obtained using a C-DHWM are in excellent agreement with the input free waves. To examine the errors caused by neglecting the currents in the decomposition, the free waves obtained using a DHWM were compared with the input in Figure 5.6 and Figure 5.9. Figure 5.6 shows the DHWM spectral peak shifts to a lower frequency than the input spectrum. This is expected because the apparent frequency is smaller than the corresponding intrinsic frequency owing to the opposing currents. However, in this case the DHWM spectrum would be very close to the input spectrum if both of them were plotted against the apparent frequency, which is quite different from the observation made in Figure 5.2. This is because wave elevation records were used in this case and no transfer function was used in the decomposition. Figure 5.6 also shows the DHWM spectrum has some wave energy in very high and very low frequency ranges but it is much smaller than that in Figure 5.2. This is because the errors in estimating free wave amplitudes near the spectral peak were much smaller than those in the previous case.

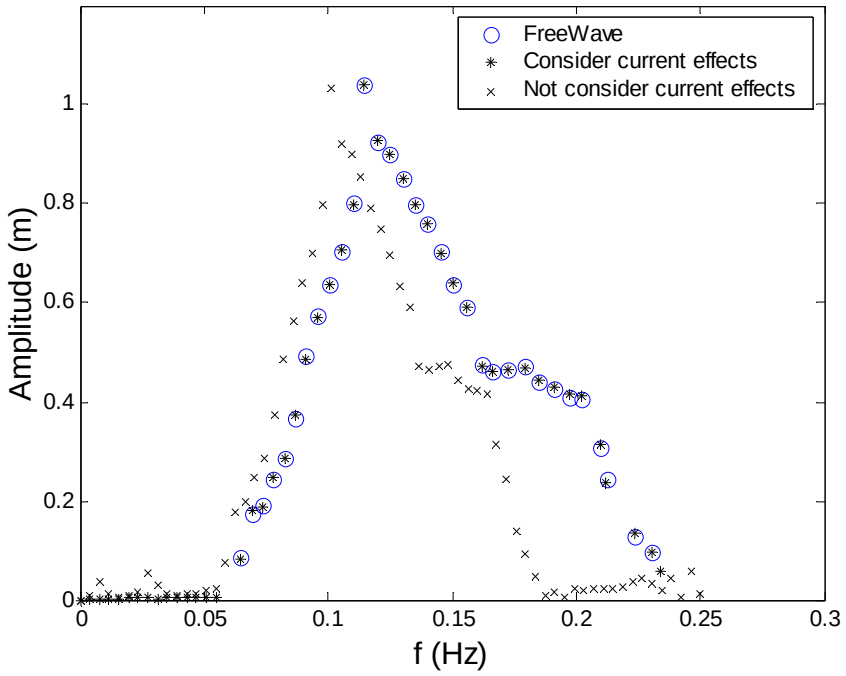

Figure 5.6: Comparison of amplitude (Elevations, Opposing current)

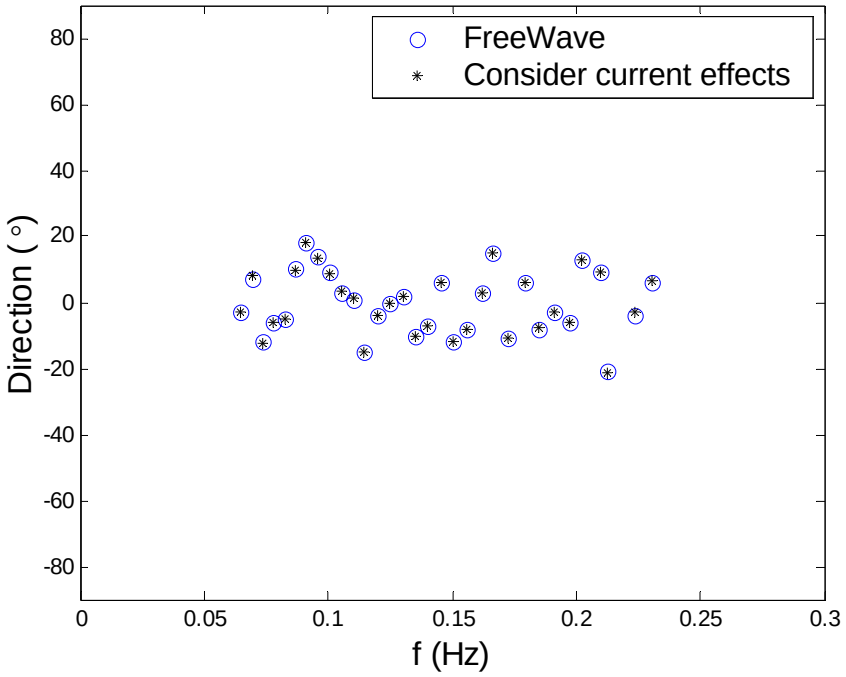

Figure 5.7: Comparison of direction (Elevations, Opposing current)

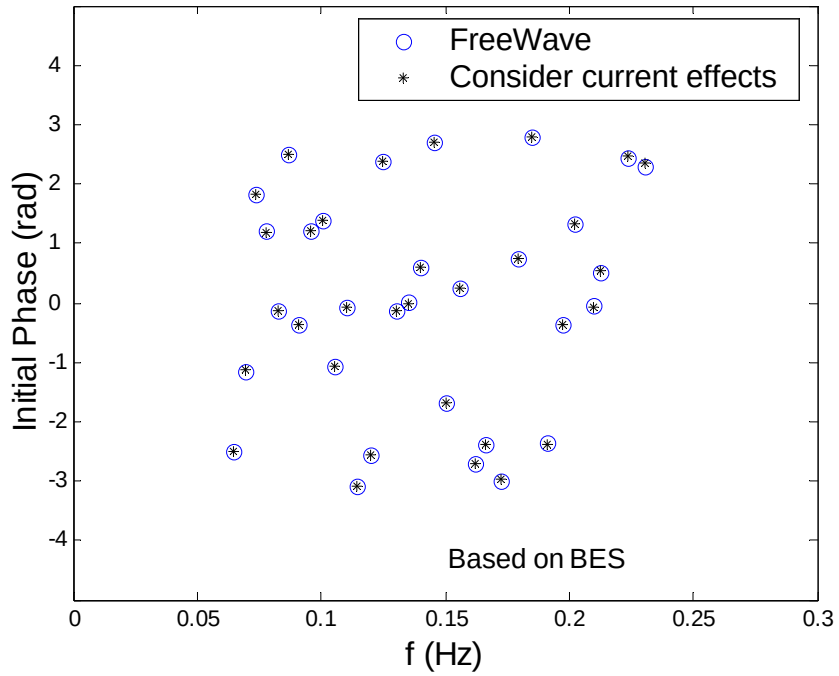

Figure 5.8: Comparison of initial phase (Elevations, Opposing current)

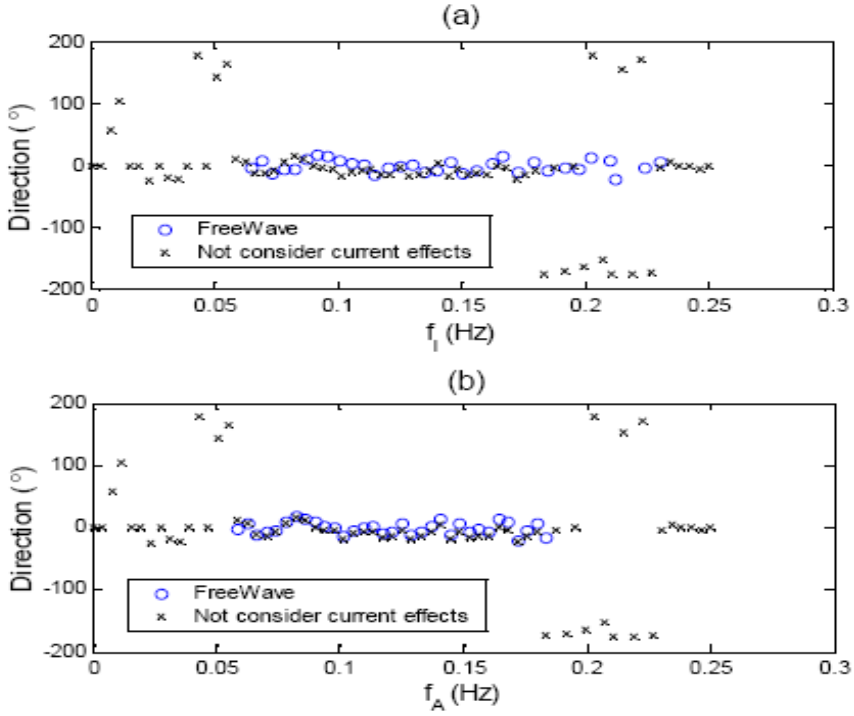

Figure 5.9: Comparison of direction in detail (Elevations, Opposing current)

The free-wave direction obtained using a DHWM and that of input free waves were plotted against the intrinsic frequency and compared in Figure 5.9(a). In addition to the difference caused by the frequency shift, there are substantial direction discrepancies between them over the entire frequency range. To demonstrate these discrepancies clearly, both wave directions were also plotted against the apparent frequency in Figure 5.9(b). Different from Figure 5.5(b) in the previous case, it shows the discrepancies between the two sets of wave directions near the spectral peak as well as large discrepancies shown in relatively high and low frequency ranges. Noticing that the input resultant elevation records were recorded at different locations, the estimated wave directions using a MLM were based on the phase delay between two wave records. The phase delay is equal to the product of wavenumber and the distance between two wave records and hence sensitive to the accuracy in estimating wavenumbers. The wavenumber estimated in a DHWM was based on the apparent frequency and the estimate of phase delay was hence incorrect. Basded on the observed errors resulting from neglecting currents in this case and the previous one, we find that the related errors depend on the type of wave records used in the decomposition.

5.4.3 Layout of Wave Elevation Records

It is known that the accuracy in estimating wave direction depends on the layout of wave gages in the absence of current (Panicker and Borgman, 1970). To shed the lights on our future analysis of WACSIS field measurements, in this numerical test we particularly chose the locations of three elevation records to resemble the locations of the Baylor Wave Staff, EMI Laser, and SAAB Radar (later referred as EBS) deployed by the WACSIS. For clearly examining the errors caused by the layout mentioned above, we artificially excluded the effects of non-linearity on wave direction estimation in this case. We used the same free waves and the opposing currents as the previous case to simulate a linear directional wave field. The three locations with respect to the main wave and currents directions were sketched in Figure 5.10. The input to linear decomposition part of C-DHWM and DHWM was the wave elevation recorded at the three locations. The

wave directions estimated respectively using linear decomposition part of C-DHWM and DHWM were compared with those of input free waves for simulating the linear numerical wave field in Figure 5.11 and Figure 5.12. To show the errors not caused by the Doppler frequency shift, the wave directions were plotted against the apparent frequency in both figures. Figure 5.11 shows that the estimated wave directions using C-DHWM remain in excellent agreement with those of input free waves, while Figure 5.12 shows large errors in the estimated wave directions using DHWM. The discrepancies are greater than those shown in Figure 5.9(b) (in the frequency range from 0.05 – 0.18 Hz). This larger errors observed in Figure 5.12 were caused by the ill-positioned records, that is, the locations of three wave records were almost aligned. It is known that if three wave sensors are exactly positioned along a line then there always exist two equally possible estimated directions symmetric to the line. Considering that the locations of three wave sensors in this numerical test were closely although not exactly positioned along a line, accurate direction estimation requires accurate estimation of the magnitude of wavenumbers that was satisfied in using C-DHWM. Owing to the neglecting the Doppler Effect, the magnitude of wavenumbers was not correctly estimated in DHWM. Consequently, the wave direction cannot be estimated correctly using DHWM. At high frequencies, the errors in estimating wavenumbers increased and the errors in estimating wave directions became very large as shown in Figure 5.12.

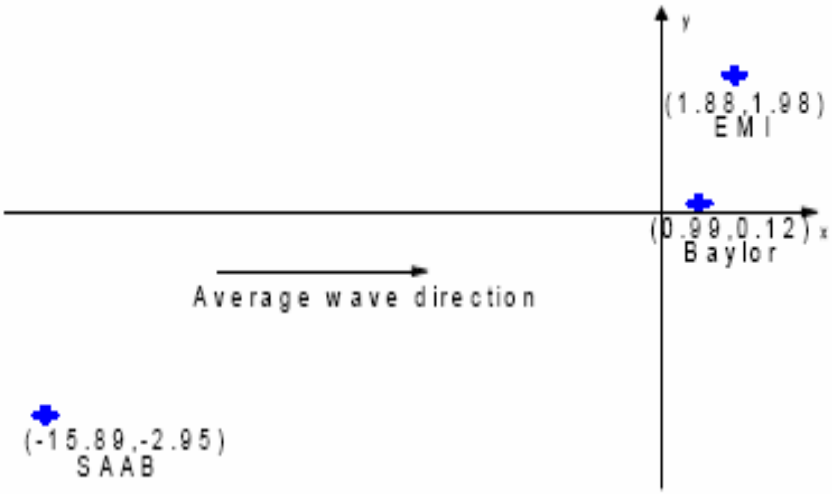

Figure 5.10: Layout of wave elevation sensors (EBS)

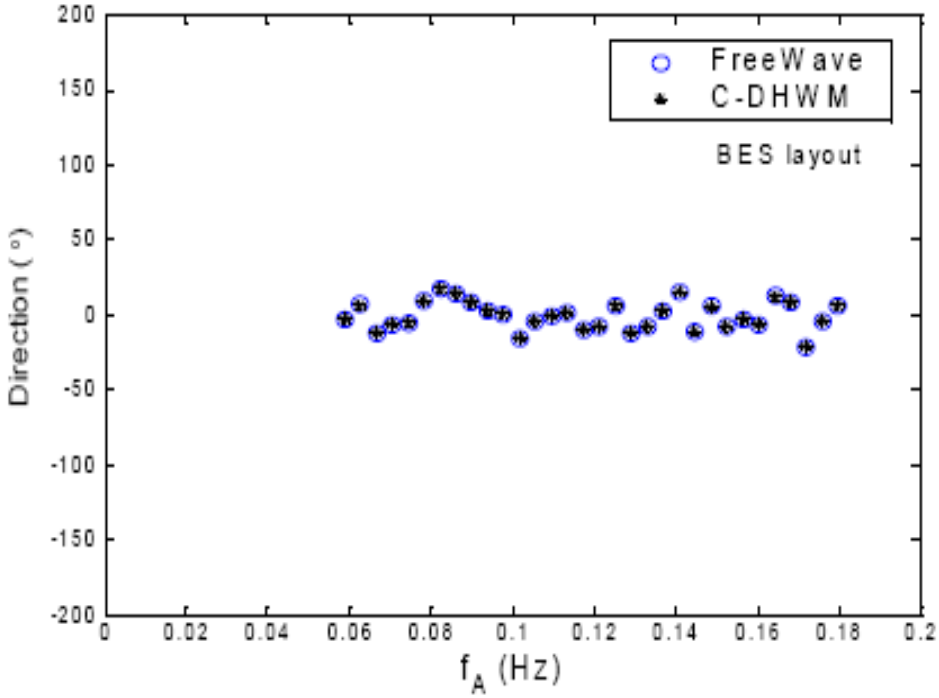

Figure 5.11: Comparison of direction (Opposing current, EBS layout, C-DHWM)

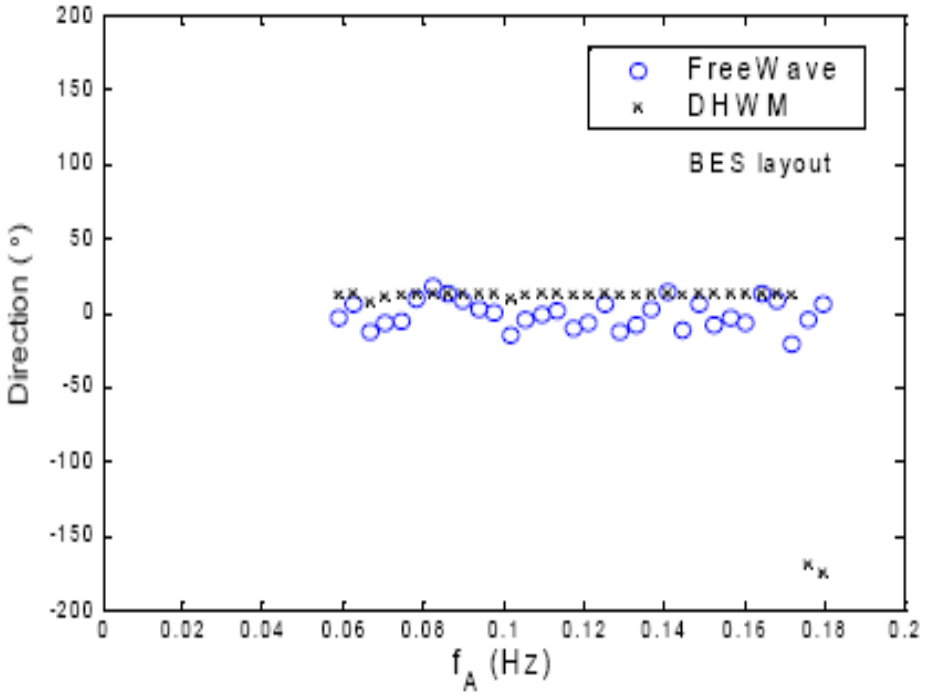

Figure 5.12: Comparison of direction (Opposing current, EBS layout, DHWM)

5.5 Cases from WACSIS Database

Different from the numeric simulations, field measurements inevitably include effects of viscosity, higher-order wave nonlinearity, wave breaking and wind. In addition, they are more or less contaminated by noise generated from instruments and the data acquisition system. These factors were not considered in the numerical tests. Hence, the applications of a C-DHWM to the cases selected from the WACSIS database are essential to examine and demonstrate its feasibility and capability.

Data files of sampling rate at 2 Hz in the WACSIS database were used in this study. The suitability and consistency of different wave sensors used by the WACSIS were investigated earlier in the absence of currents and presented in Chapter IV, showing that wave characteristics could be deterministically predicted based on three or more wave

records using a DHWM. The present study extends the previous study to allow for the analysis of wave records in the presence of significant currents. Three data files involving relatively strong currents were selected upon the recommendation (Prevosto, 2002). They are named as 9802281040, 9803031420 and 9803031800, respectively. The directions of currents in the three selected cases were roughly the perpendicular, opposite and same as the mean wave directions, respectively. Since wave sensors deployed by the WACSIS were within a relatively small area (about hundreds of square meters), ocean waves and the current in the vicinity of these sensors were assumed to be uniform. To ensure whether or not the currents were steady in 20-min duration, the velocity vectors of currents measured by S4ADW are averaged over every 10-min period in a span of 30 min. Figure 5.13 presents an example. It shows the velocity virtually remains unchanged and validates the assumption of steady currents within 20-min duration. However, avareage velocities might change their direction completely in a 4-hour span. Main characteristics of currents and wave fields of the three selected cases are summarized in Table 5.1. In each case, all wave records were synchronized in the same way as described in Chapter IV.

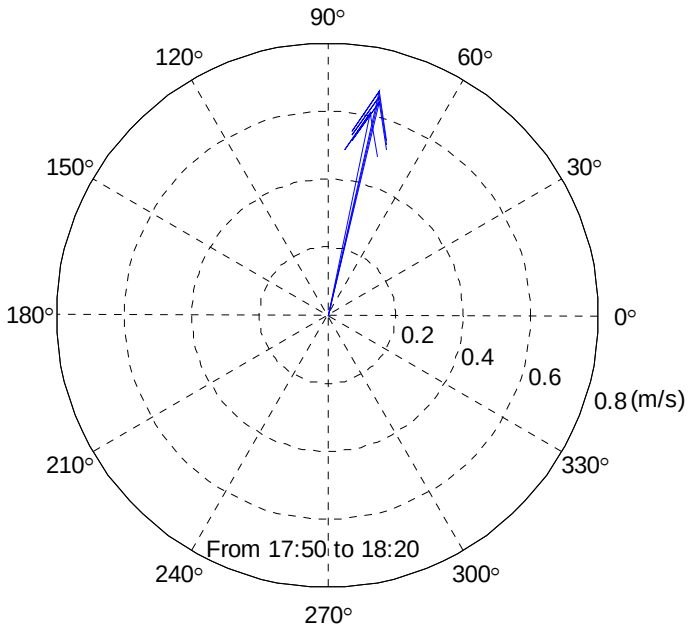

Figure 5.13: Average current velocity vectors from 17:50 to 18:20 (Case 9803031800)

Table 5.1: Wave and current characteristics of selected cases.

Case Name	Current (m/s)	Current Direction	Wave Direction at Peak	Significant Wave Height	Peak Wave period
9803031800	0.67	76.7°	39.5°	3.97m	8.70s
9803031420	0.41	-115.2°	33.3°	2.43m	7.14s
9802281040	0.70	-117.8°	-29.0°	3.19m	8.33s

5.5.1 Case 9803031800 (Following Current)

As shown in Table 5.1, the angle between the wave and current directions is about 37.2°. Hence, it was roughly categorized as the following-current case. First, the data files of 20-min pressure and two horizontal velocity components recorded by S4ADW were used as input (PUV data set) to the decomposition part of C-DHWM and DHWM, respectively. The free-wave amplitude spectra obtained respectively by these two models were plotted against the intrinsic frequency in Figure 5.14. Because S4ADW was located 10-m below the still water level, the ratio of signal to noise of its measurements was very low at high frequencies. Hence, the spectra were truncated at 0.20 Hz. They were also truncated below 0.05 Hz because of very weak signal. As expected, the discrepancies between the spectra obtained respectively using a C-DHWM and DHWM followed the same trends observed in Figure 5.2. The peak of the spectrum predicted by a DHWM was shifted to a higher frequency and its amplitudes were overestimated at relative high frequencies. For comparison with the wave direction provided by the Waverider buoy, the predicted wave directions were plotted against the apparent frequency in Figure 5.15. Wave directions predicted by both models were in satisfactory agreement except at relatively low frequencies, which is consistent with the observation based on Figure 5.5(b). Both predicted wave directions were about 15° higher than the results of the buoy. Secondly, we used the elevation measurements recorded by the sensors EMI laser, Baylor wave staff and SAAB radar (hereinafter referred EBS data set) as the input to the decomposition. The two predicted free-wave amplitude spectra were compared in Figure 5.16, and the predicted wave directions and the corresponding results of the buoy were plotted against the apparent frequency in Figure 5.17. Because the ratio of signal to noise in the elevation measurements is large enough in the frequency range, 0.20 - 0.25 Hz, the corresponding predictions were truncated at 0.25 Hz. The amplitude spectra and wave direction predicted using a C-DHWM respectively based on the PUV and EBS data sets were consistent. The predicted wave directions are about 10° – 15° greater than those given by the buoy. However, in the very low frequency range (0.05 – 0.07 Hz), the predicted wave directions were quite different from the buoy results. We suspect the

large difference at very low frequencies may result from notorious inaccuracy of buoys at very low frequencies.

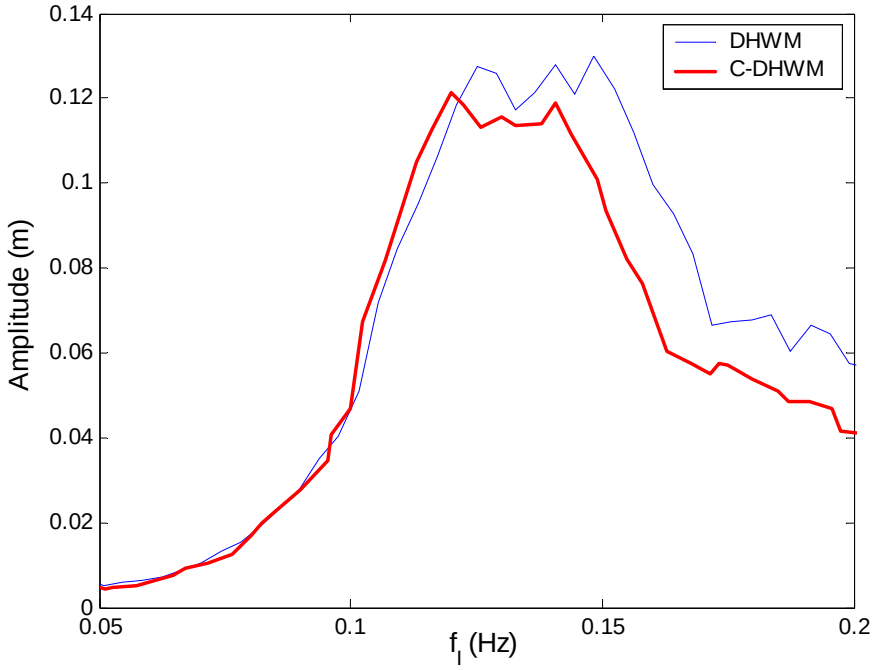

Figure 5.14: Comparison of amplitude based on S4ADW (Case 9803031800)

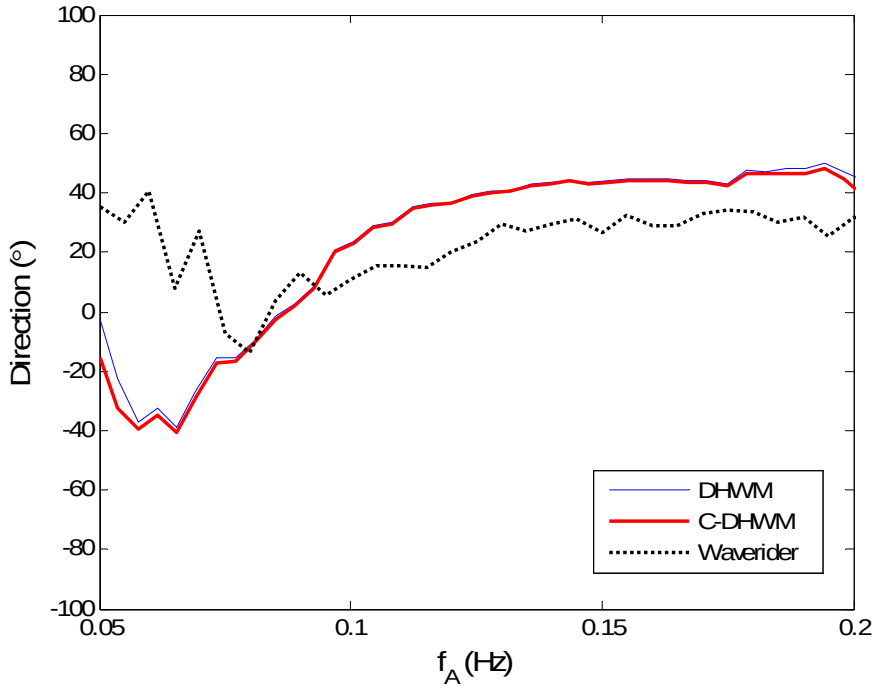

Figure 5.15: Comparison of direction based on S4ADW (Case 9803031800)

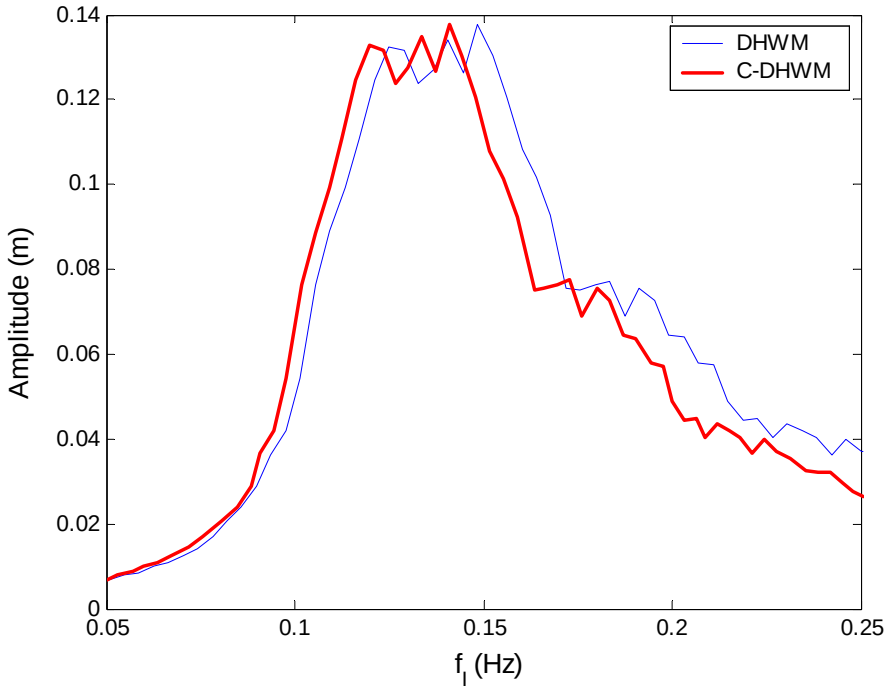

Figure 5.16: Comparison of amplitude based on EBS (Case 9803031800)

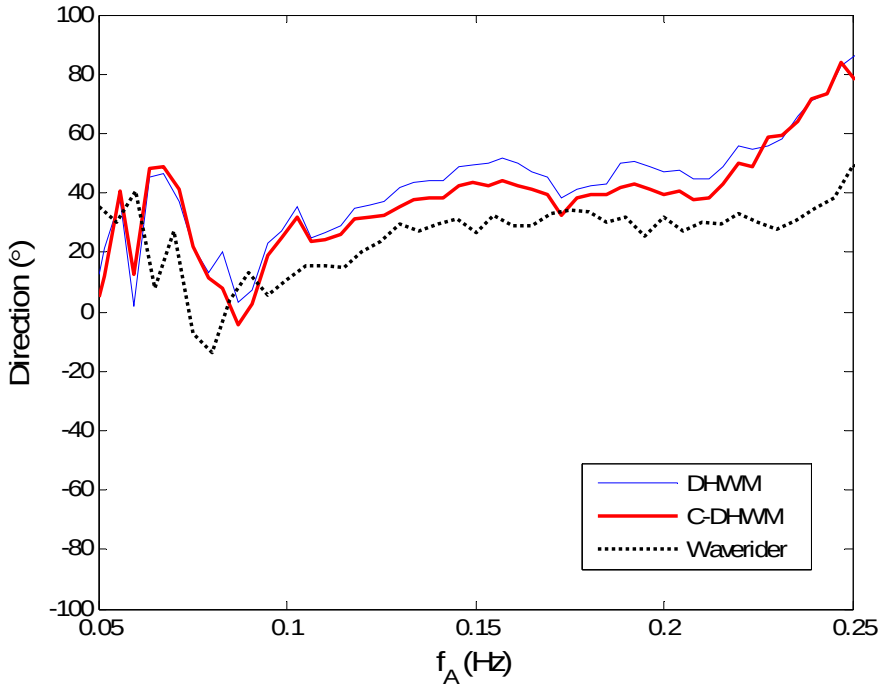

Figure 5.17: Comparison of direction based on EBS (Case 9803031800)

5.5.2 Case 9803031420 (Opposing Current)

The relative direction between currents and waves was about 148.5°, which is categorized as the opposing-current case. Using the PUV data set as input, the free-wave amplitude spectra predicted respectively using the two models were plotted against the intrinsic frequency in Figure 5.18. The wave directions predicted by the two models and the corresponding buoy results were plotted against the apparent frequency in Figure 5.19. Using the EBS data set as input, the corresponding predictions are plotted in Figure 5.20 and Figure 5.21. When currents are opposite to the wave direction, apparent frequencies are smaller than the corresponding intrinsic ones. The peak frequency of a DHWM amplitude spectrum shifted to a lower frequency. Wave amplitudes are under-predicted at high frequencies when the PUV data set was used as input, consistent with

the observation made in the corresponding numerical test. However, the related discrepancies are smaller due to small velocity of currents in field measurements.

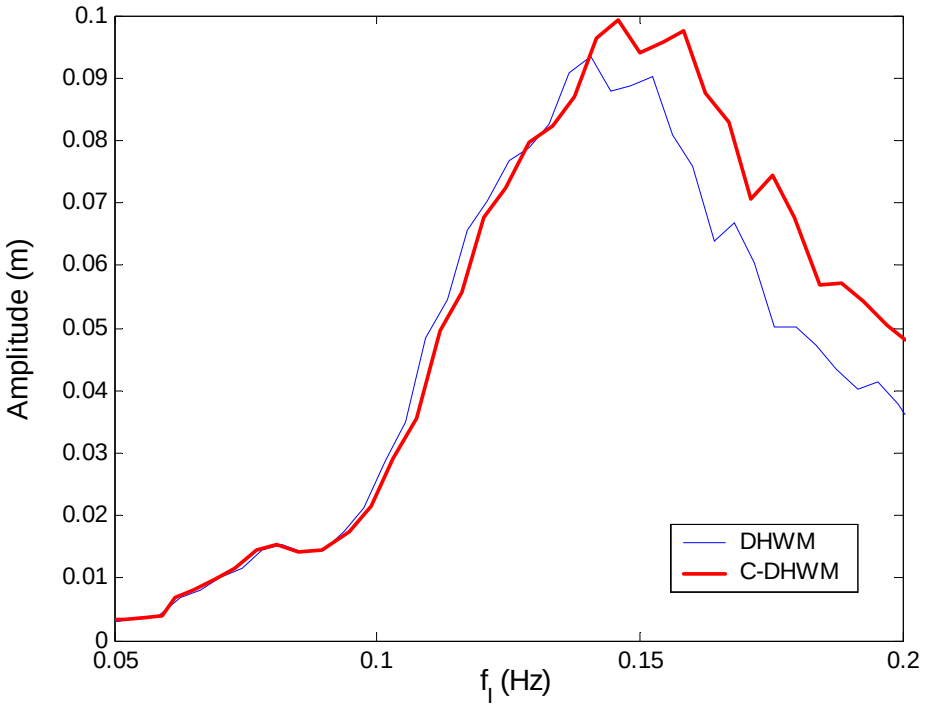

Figure 5.18: Comparison of amplitude based on S4ADW (Case 9803031420)

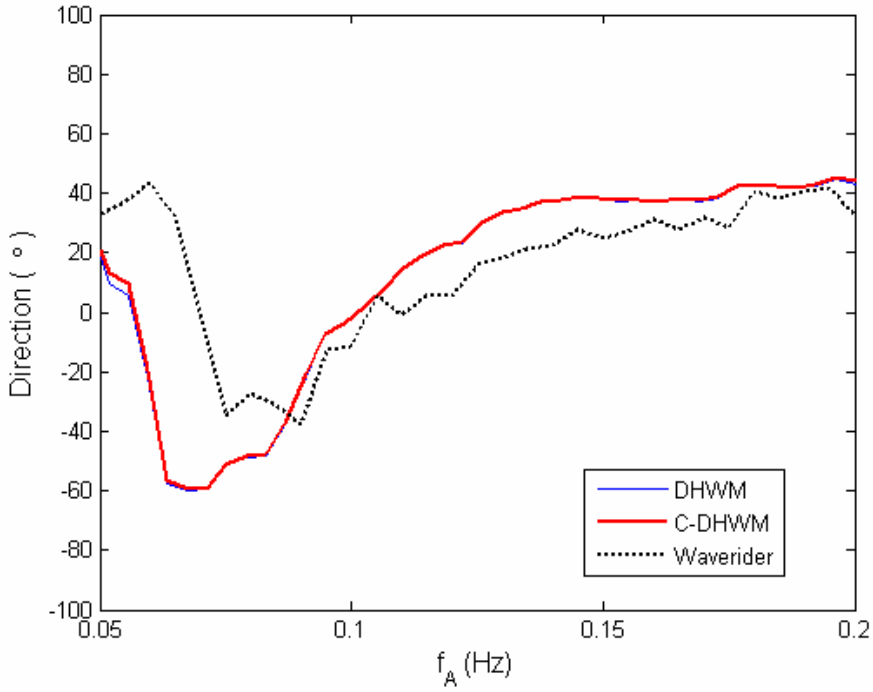

Figure 5.19: Comparison of direction based on S4ADW (Case 9803031420)

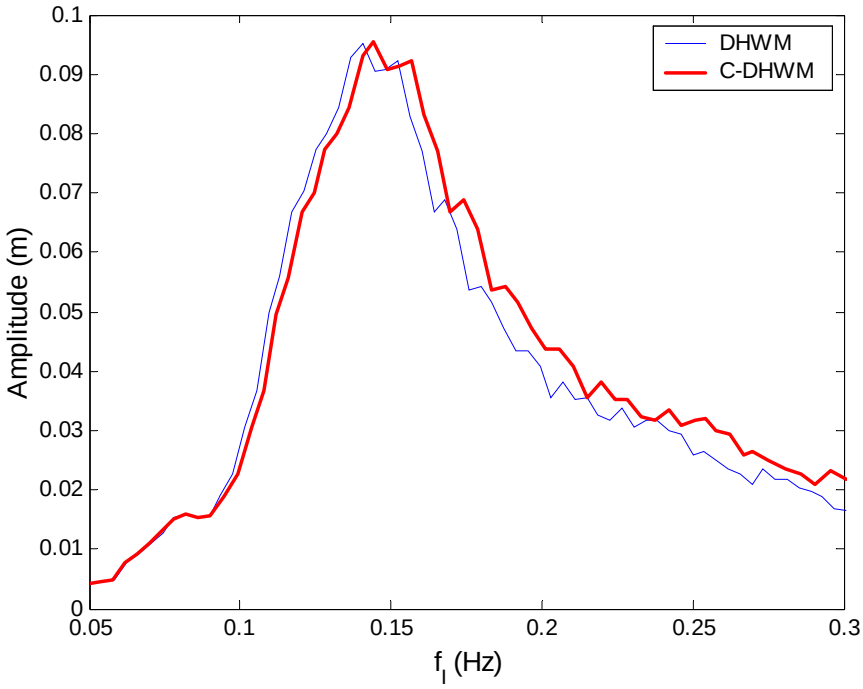

Figure 5.20: Comparison of amplitude based on EBS (Case 9803031420)

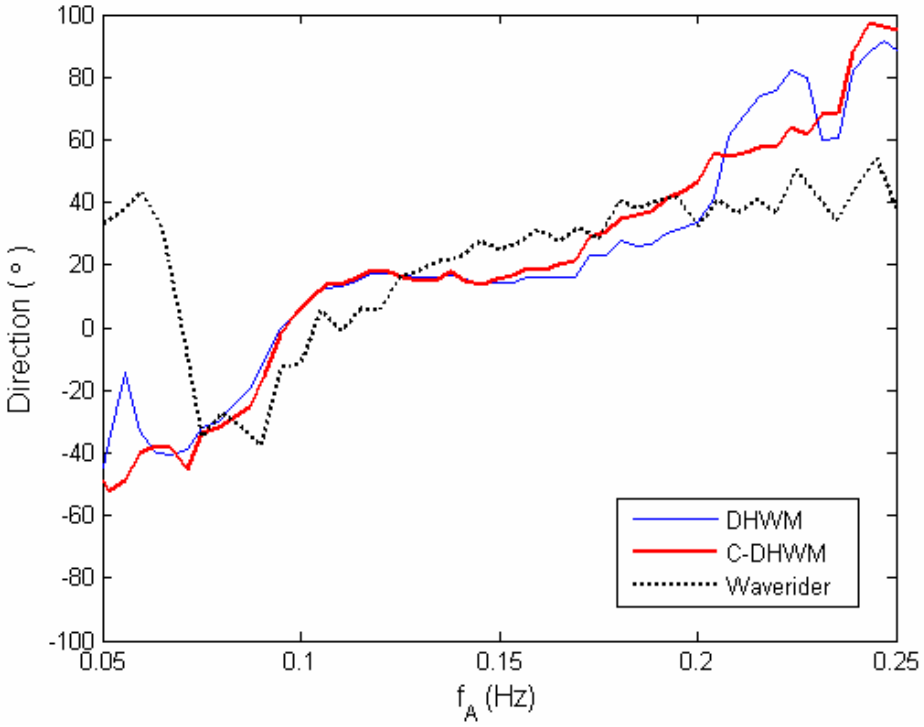

Figure 5.21: Comparison of direction based on EBS (Case 9803031420)

5.5.3 Case 9802281040 (Perpendicular Currents)

The angle between the wave and current directions is about 88.8° and it is named as perpendicular-current case. According to Eq. (5.12), the Doppler effect of currents on wave frequencies is insignificant in this case. As expected, we found that the peak frequency shift and over- or under-estimated amplitude at high frequencies in a DHWM spectrum are insignificant in comparison with those in the previous two cases. For brevity, its comparison with the corresponding one of C-DHWM is omitted.

CHAPTER VI

ESTIMATION OF DIRECTIONAL SPREADING PARAMETERS OF A COSINE-2S MODEL

6.1 Introduction

For simulating directional waves numerically or experimentally, a cosine-2*s* model (Eq. 1.1) has been widely used to describe waves spreading in a uni-modal wave field. In cosine-2*s* model, both mean wave direction θ_M and spreading parameter *s* depend on frequency *f* and are the key factors for the simulation of directional waves when this model is employed. Hence, the calibration and collection of various sea states in term of these two parameters are of great importance to wave climatology.

A general directional spreading function $D(\theta)$ at frequency *f* can be expanded in an angular Fourier series

$$D(\theta) = \frac{1}{\pi}\left(\frac{1}{2} + \sum_{n=1}^{\infty} A_n \cos n\theta + B_n \sin n\theta\right). \tag{6.1}$$

where A_n and B_n are the angular Fourier coefficients. In practice, directional waves are often measured by three or more wave sensors. Three wave sensors at the same location are commonly deployed for measuring directional waves, for example, a pitch/roll buoy or the combination of a pressure transducer and a current meter. Based on three simultaneous wave measurements recorded at the same location, it is known that only the first and second angular Fourier coefficients can be obtained based on the cross spectra using a method known as Direct Fourier Transfer (DFT) (Longuet-Higgins et al., 1963). In the case of the measurements recorded by a pitch/roll buoy,

$$A_1 = \frac{Q_{12}}{\left[C_{11}(C_{22}+C_{33})\right]^{1/2}} \tag{6.2}$$

$$B_1 = \frac{Q_{13}}{\left[C_{11}(C_{22}+C_{33})\right]^{1/2}} \tag{6.3}$$

$$A_2 = \frac{C_{22}-C_{33}}{C_{22}+C_{33}} \tag{6.4}$$

$$B_2 = \frac{2C_{23}}{C_{22}+C_{33}} \tag{6.5}$$

where subscripts 1, 2 and 3 denote wave elevation, *x*- and *y*-direction wave slope of the surface, respectively, and C_{ij} and Q_{ij} are the real and imaginary parts of a cross spectrum between wave records *i* and *j*. The spreading parameter *s* and the mean wave direction θ_M are related to the first harmonic through Eqs. (1.3) – (1.5) or the second harmonic through Eqs. (1.6) – (1.8). In the following description, we name this approach as the conventional approach.

As introduced in Chapter 1, the conventional approach is sensitive to the errors in estimating the cross spectra (Figure 6.1), which cause the inaccurate and instable estimations of the directional spreading parameter *s*. For accurate and consistent estimates of the directional spreading parameter and mean wave direction of directional seas based on a cosine-2s directional spreading model, a new approach is proposed, employing a Maximum Likelihood Method (MLM) to estimate the directional spreading function and then the angular Fourier coefficients. Because a MLM is more tolerant of errors in the estimated cross spectrum than a directional Fourier transfer used in the conventional approach, the proposed approach is able to estimate the directional spreading parameter more accurately and consistently, which is examined and confirmed by applying the proposed and conventional approach, respectively, to the time series generated by numerical simulation and recorded in field.

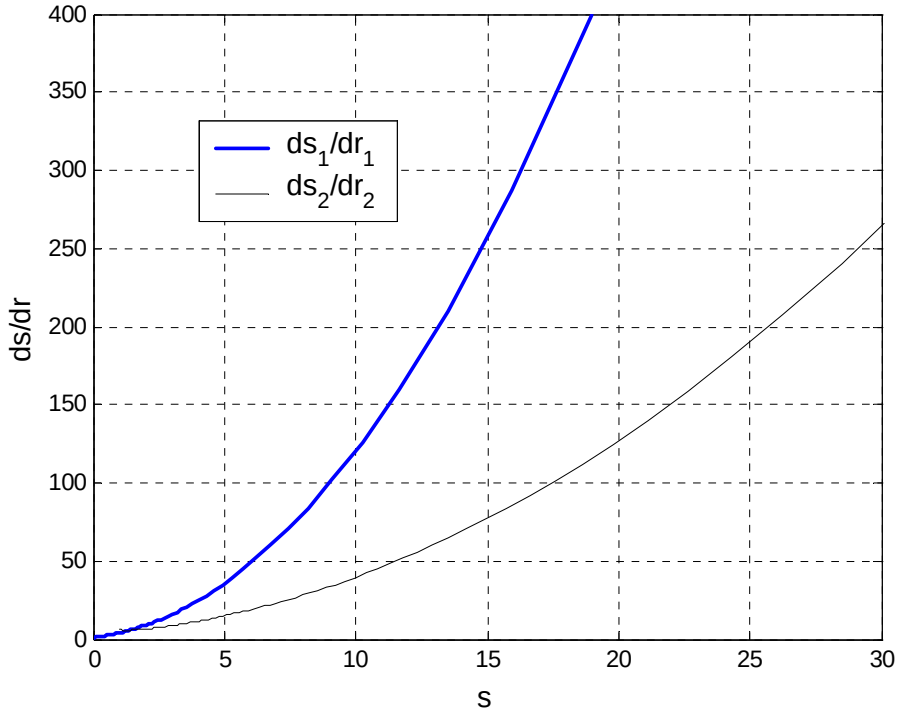

Figure 6.1: Sensitivity of s to r ($r_i = \sqrt{A_i^2 + B_i^2}$)

6.2 Errors in the Estimation of Cross Spectra

The computation of the cross spectra of a wave field is a prerequisite of estimating its directional spreading parameter s and the mean wave direction θ_M . Errors related to estimated cross spectra may result from noises occurring in measurements and assumptions made in computing wave characteristics, such as the neglecting of nonlinear wave interactions, wind, wave breaking, and the viscosity of water. In addition, the most common errors result from so called interaction term, which exists even in a homogenous wave field numerically generated based on linear wave theory. Since this

type of errors is significant and common to the estimated cross spectra and in turn to the predicted spreading parameter and mean wave direction, here we briefly show the source of the interaction term and the related measure for reducing its magnitude.

To simulate a linear and homogenous directional wave field, a single summation over the frequency domain is used to produce a resultant wave property by superposing the corresponding one of individual wave components.

$$\mathrm{X}_m(t) = \mathrm{Re}\sum_{j=1}^{\infty} H_m(f_j, \theta_j, \vec{x}, z) a_j e^{-i\psi_j} \tag{6.6}$$

where, $\psi_j = \vec{k}_j \cdot \vec{x} - 2\pi f_j t + \delta_j$, a_j, k_j and δ_j are, respectively, the amplitude, wavenumber and initial phase of *j-th* component, and t is time. H_m stands for a linear transfer function from the elevation to the *m-th* wave property. For example, the linear transfer functions used in this chapter are listed in Table 6.1. Considering the fact that numerically generated or measured wave records used in this study to determine the cross spectra are of the same horizontal coordinates, without loss of generality, we may put the location of these records coincident with or below the origin of the Cartesian coordinates whose *x*- and *y*- axis are in the plane of the still water surface and the *z*-axis points upward. Hence, the horizontal coordinates of wave records disappear in the following equations.

Table 6.1: Linear transfer functions for different wave properties.

$$\Upsilon = \frac{\cosh\left[k\left(h+z\right)\right]}{\cosh kh},\ \Pi = 2\pi f \frac{\cosh\left[k\left(h+z\right)\right]}{\sinh kh}$$

Wave Property	$H_m(\theta, f, z)$
Pressure	$\rho g \Upsilon$
x-axis velocity	$\Pi \cos\theta$
y-axis velocity	$\Pi \sin\theta$
x-axis displacement	$i\Pi \cos\theta$
y-axis displacement	$i\Pi \sin\theta$

To generate an ocean wave field consisting of numerous wave components whose frequencies vary almost continuously from low to high, the increment frequency, Δf_g, is chosen to be extremely small. That is, it is much smaller than the frequency increment used in the decomposition of a wave field into wave components, $\Delta f_g \ll \Delta f_d = 1/T$, where T is the duration of wave records used in the decomposition. The use of a single summation implies that simulated resultant waves are different in directions at different frequencies but uni-directional at each discrete frequency, which seems to contradict the concept of wave directional spreading. The seemingly contradictory is resolved owing to $\Delta f_g \ll \Delta f_d = 1/T$. The components in frequency band Δf_d describe the directional spreading properties.

Based on the time series with limited duration *T*, the decomposed wave component at a discrete frequency defined by the FFT, is the convolution of the actual wave components (of much finer resolution, Δf_g, in the frequency domain) and the Fourier transform of a window function of duration *T*,

$$F_m(f_k) = H_m a e^{-i\psi} \otimes W \,, \tag{6.7}$$

where $\otimes$ denotes convolution. Various window functions, for example rectangular and Hanning windows (Harris, 1978), were employed in the digital signal processing. In the following equations, a rectangular window is used, which is also employed in our analysis of numerical simulation and field measurements. The Fourier transform of a rectangular window function is given by

$$W(f) = \frac{\sin \pi fT}{\pi fT} e^{-i\pi fT} \,. \tag{6.8}$$

It is noted that the magnitude of W diminishes when $|f|$ increases. Hence, Eq. (6.7) can be approximated by

$$F_m(f_k) = \sum_{j=k-M}^{k+M} H_m(f_j, \theta_j, z) a_j e^{-i\psi_j} W\left(f_j - f_k\right) \tag{6.9}$$

where M is a relatively large integer and $M\Delta f_g \le \Delta f_d < (M+1)\Delta f_g$. The above equation indicates that the decomposed wave component of discrete frequency, f_k, is approximately equal to the superposition of $2M$+1 wave components used in generating resultant wave field whose frequencies range from $f_k - M\Delta f_g$ to $f_k + M\Delta f_g$. These ($2M$+1) wave components are different in directions and the directional spreading at frequency f_k can be approximately realized by appropriately choosing the directions of the $2M$+1 wave components to follow a prescribed directional spreading function. Details about the implementation of the single summation model will be described in the following section.

Using the Fourier coefficients of the wave properties *m* and *n*, the cross spectrum between them at discrete frequency, f_k , is given by

$$\hat{\phi}_{mn} = \frac{1}{2}\sum_{j=k-M}^{k+M} H_m(f_j,\theta_j,z)H_n^*(f_j,\theta_j,z)w_j{}^2a_j^2 + \delta\phi_{mn}, \tag{6.10}$$

where

$$w_j = \frac{\sin\pi\left(f_j - f_k\right)T}{\pi\left(f_j - f_k\right)T}, \tag{6.11}$$

$$\delta\phi_{mn} = \frac{1}{2}\sum_{j=k-M}^{k+M}\sum_{\substack{i=k-M \\ l\neq j}}^{k+M} H_m(f_j,\theta_j,z)H_n^*(f_l,\theta_l,z)w_jw_la_ja_le^{-i\Delta\psi_{jl}}, \tag{6.12}$$

$$\Delta\psi_{jl} = \delta_j - \delta_l - \pi(f_j - f_l)T, \tag{6.13}$$

and * denotes the complex conjugate. The left hand side of Eq. (6.10) is the estimated cross spectrum and the first term at the right hand side is approximately the true cross spectrum. The second term, $\delta\phi_{mn}$, known as the interaction term, is hence the discrepancy between the true and estimated cross spectrum. Since $\Delta\psi_{jl}$ is a random variable, the error, $\delta\phi_{mn}$, behaves like a random variable as well. Its statistical properties were derived by Jenkins and Watts (1968). Although the mean of the error is equal to zero, for each individual realization (run) it is not likely to be zero and indeed may not be very small. Their results were also confirmed in our numerical tests. For example, the normalized error, $\delta\phi_{11}/\phi_{11}$, of the computed power spectrum from a single realization approximately obeys the *chi-square* distribution $\left(\frac{1}{2}\chi_2^2 - 1\right)$ with 2 degrees of freedom, as plotted in Figure 6.2. In a single realization, the probability for $\left|\delta\phi_{11}/\phi_{11}\right| < 0.1$ is only

about 0.0737, indicating that in more than 90% of individual realizations the relative error is greater than 10%. To increase the probability for $\left|\delta\phi_{11}/\phi_{11}\right| < \varepsilon$, where ε is a small positive fraction, say 0.1, a common practice is to chop a time series of a wave record into a number of segments of the same duration *T*. A cross spectrum is calculated based on a simultaneous set of segments belonging to a pair of wave records and then the corresponding cross spectra of all segments are averaged to render the average cross spectrum. The normalized error of the average power spectrum, $\overline{\delta\phi_{11}}/\overline{\phi_{11}} \sim \left(\frac{1}{2n}\chi^2_{2n} - 1\right)$, obeys the *chi-square* distribution with *2n* degrees of freedom, where *n* is the number of segments used in the average. The probability density functions for related *chi-square* distributions of n = 16 and 128 are also plotted in Figure 6.2. It is shown that the variance of the normalized error is greatly reduced with the increase of *n*. For example, the probability that $\left|\overline{\delta\phi_{11}}/\overline{\phi_{11}}\right| < 0.1$ increases to 0.7429 when n =128. In reality, however, the number of segments is limited due to the overall length of measured wave records and even if the measurements have the duration much longer than 20 min the overall length of wave records used in the analysis has to be truncated in order to be consistent with the assumption of stationary wave fields.

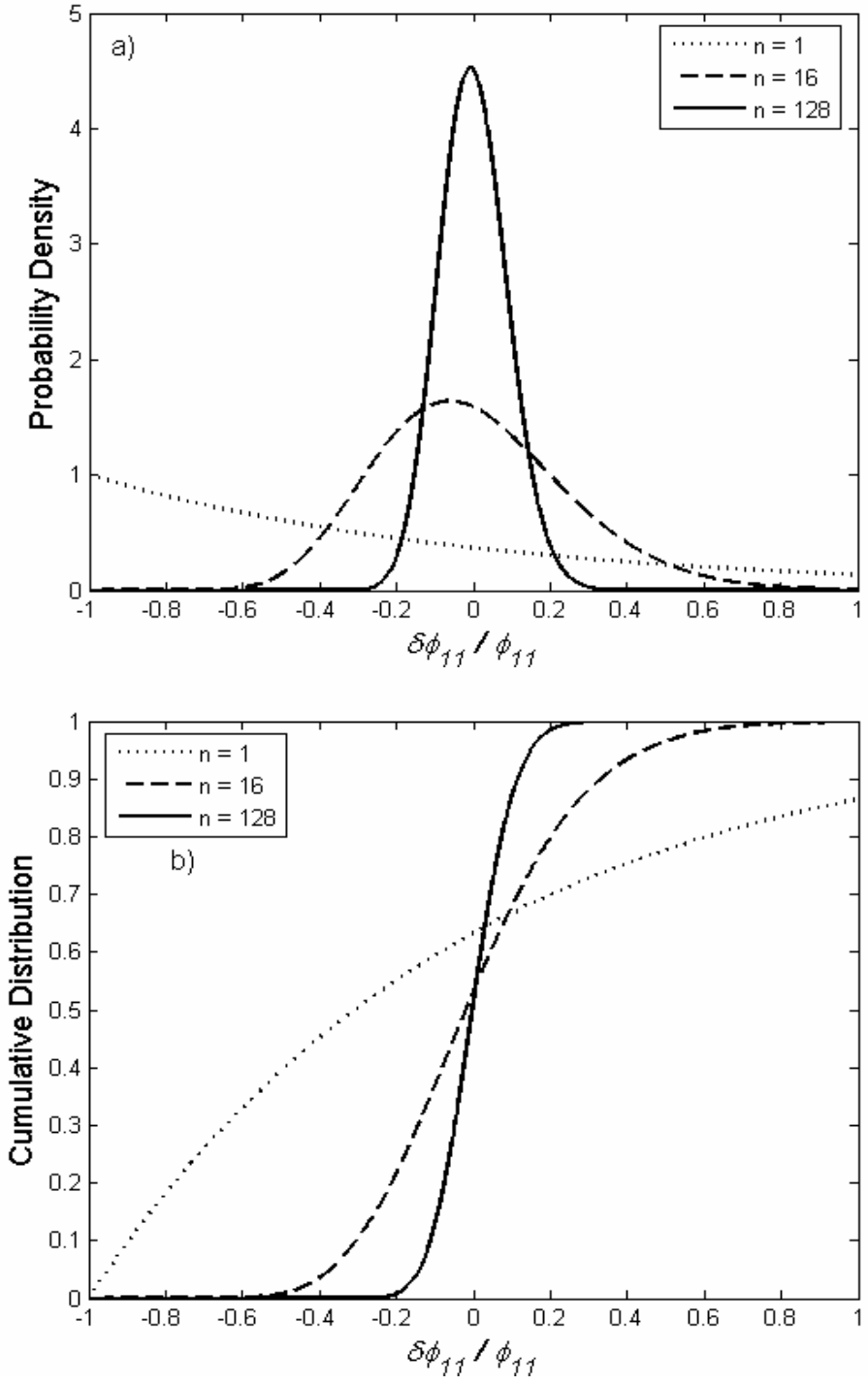

Figure 6.2: a) Probability density and b) Cumulative distribution of $\delta\phi_{11} / \phi_{11}$

6.3 A New Approach for Estimating Directional Spreading

To obtain consistent and reliable estimation of uni-modal directional seas in terms of θ_M and s, we propose a new approach based on the directional spreading function estimated using a data adaptive method. It was demonstrated that the directional spreading of a measured wave field can be estimated using data adaptive methods, such as Maximum Likelihood Method (MLM), Maximum Entropy Method (MEM) and Bayesian method. Based on three simultaneous wave records, such as those measured by a pressure-current sensor (PUV) or a pitch/roll buoy, a conventional DFT method renders a directional energy spreading described by the first and second Fourier coefficients only while a data adaptive method is able to render a general approximate energy spreading. Because a MLM does not require prescribed (often subjective) parameters and its numerical scheme is relatively simple in comparison with a MEM or Bayesian method (Massel and Brinkman, 1998), we use a MLM to estimate the directional spreading function. Three basic steps involved in our proposed approach are outlined in Figure 6.3 and elaborated below.

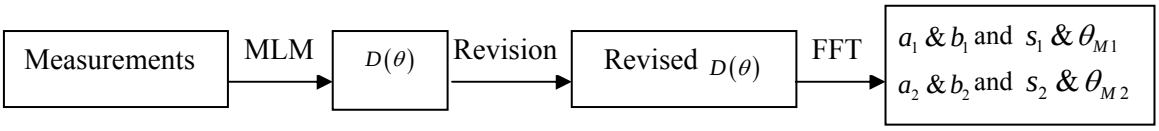

Figure 6.3: Flow chart of the proposed approach

At the beginning, the directional spreading function denoted by $D(\theta)$ is estimated using a MLM based on three or more simultaneous wave records following Isobe et al. (1984). In comparison with a prescribed uni-modal wave spreading function following which a

cross spectrum matrix was generated and used as the input to the MLM, Isobe et al. (1984) found that the MLM slightly under-predicted wave energy around the mean wave direction while over-predicted energy around the opposite direction. His observation was also confirmed in our related numerical tests.

Knowing the shortcomings of the MLM, in the second step we modify the estimated directional spreading function $D(\theta)$ to reduce the discrepancies. The modification is to cut wave energy nearby the opposite direction and then add to that around the mean direction. As sketched in Figure 6.4, the cut-off angles, denoted by θ_L and θ_R, beyond which the wave energy is cut, are chosen based on two criteria: 1) the amount of wave energy cut beyond θ_L and θ_R is 7% of the total wave energy, and 2) wave energy at these two angles are equal, $D(\theta_L) = D(\theta_R)$. To conserve the total energy, 7% energy cut in the tail is added back to the energy spreading function between θ_L and θ_R. The addition at a given direction θ is proportional to the value of $D(\theta)$ before the cut. Hence, the modification of energy spreading keeps the mean wave direction virtually unchanged and adds the wave energy mainly around the mean wave direction. It is noted that the modified energy spreading function abruptly reduces to zero at θ_L and θ_R. Because the discontinuities at these two directions do not play significant roles in determining the first and second Fourier coefficients (for estimating θ_M and s) of modified directional spreading function, no effort was made to smooth them. It is also noted that the choice of 7% cut-off energy in the tail is not a rigorous decision. Our numerical tests, however, show that the 7% cut works well in reducing the discrepancies between the directional spreading function predicted by the MLM and the corresponding cosine-2s function used as the input in for a wide range of s. It should be noted that the above modification to $D(\theta)$ may fail if the estimated directional spreading function is of bi- or multi-modal. Hence, the application of the proposed approach should be limited to sea states of uni-modal directional spreading. At the third step, the first and second

Fourier coefficients of the modified $D(\theta)$ are obtained using the FFT and then the parameters s_1 and θ_{M1} or s_2 and θ_{M2} are calculated using Eqs. (1.3) – (1.8).

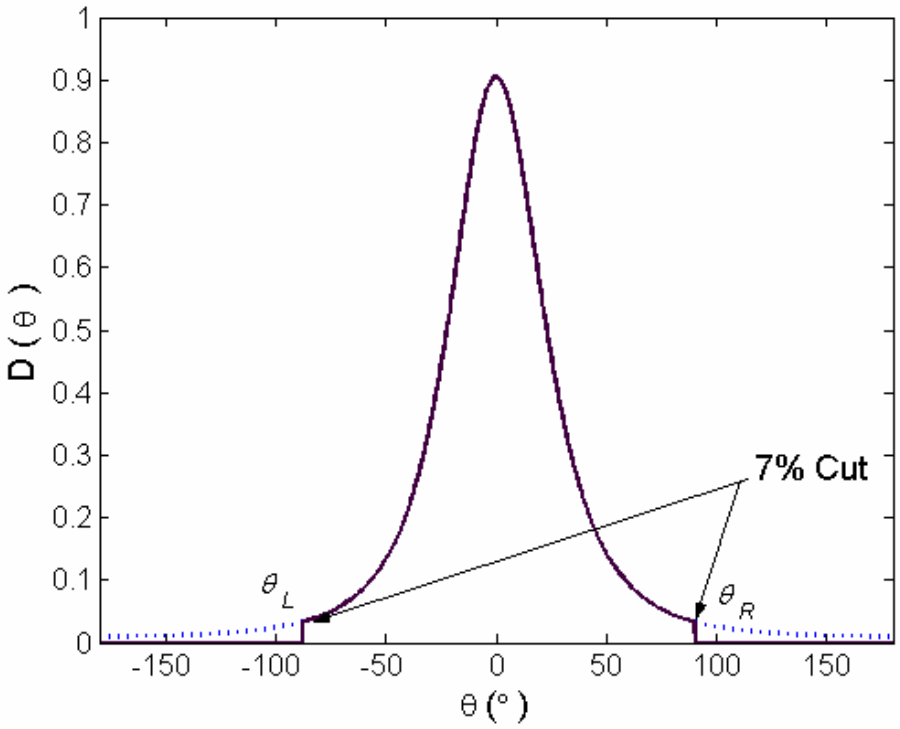

Figure 6.4: Sketch of the modification of $D(\theta)$

6.4 Application to Numerically Generated Wave Records

6.4.1 Numeric Simulation of Directional Waves

Numeric simulation of directional waves provides an indispensable tool for studies of their properties. The primary purpose of this section is to introduce the background

information for the numeric simulations which are adopted in this chapter to verify the proposed approach.

Two different principles exist in numeric simulations of directional waves, deterministic and probabilistic approach. The deterministic method is also known as the random phase (RP) method. In this method, the amplitude of each Fourier component is set deterministically according to the desired or target frequency spectrum and the initial phase is set to a random variable with a uniform distribution from $-\pi$ to π. The wave elevation time series is obtained by an inverse Fourier transform. The main advantage of the RP method is that the target spectrum can be matched over the recycling length of the simulation. The probabilistic approach is also known as the random Fourier coefficient method or nondeterministic spectral amplitude method. In this technique, the Fourier coefficients (real and imaginary parts) are first set to independent random variables having a Gaussian distribution with zero mean and unit variance. The amplitude of a wave component is then multiplied by the square root of the related discrete area of the target spectra. A subsequent inverse Fourier transform yields the desired wave elevation time series. Any particular realization of a relatively short duration will produce spectral shapes with statistical variability similar to that of real wave spectra of the same duration. Since in this study we only employ the deterministic approach, the following description is limited to the RP method. Regarding the RP method, several different models have been presented in the literature over the past decades. They are generally classified as Double Summation Model and Single Summation Model (Miles and Funke, 1989).

a) Double Summation Model

The double summation model for the wave elevation of a linear Gaussian directional sea was original proposed by Borgman (1969) and one version of the double summation model (Miles and Funke, 1989) is given by:

$$\eta(x,y,t)=\sum_{i=1}^{N}\sum_{j=1}^{M}a_{ij}\left(\sqrt{\frac{2}{P}}\sum_{l=1}^{p}\cos\left[\sigma_{il}t-k_{il}\left(x\cos\theta_j+y\sin\theta_j\right)+\delta_{ijl}\right]\right) \tag{6.14}$$

where,

$$a_{ij}=\sqrt{2S_\eta(f_i)D(f_i,\theta_j)\Delta f\,\Delta\theta} \tag{6.15}$$

$$\sigma_{il}=\left(\sigma_i-\frac{\Delta\sigma}{2}\right)+l\frac{\Delta\sigma}{P} \tag{6.16}$$

P is the number of wave component in a frequency band of width $\Delta\sigma$. In this version, a unidirectional wave train traveling in direction θ_j is constructed in each frequency band $\Delta\sigma$ centered at σ_i. Miles and Funke (1989) indicated that the variance of wave energy in a frequency band $\Delta\sigma$ decrease with the increase of P. If P is sufficiently large, the variance of wave energy over space can be reduced to an acceptable level. It should be pointed that their conclusion is no longer valid if the resolution of the spectra analysis is $\Delta\sigma/P$, instead of $\Delta\sigma$. If $f_d=\frac{\Delta\sigma}{P}\frac{1}{2\pi}$, the resultant wave field is neither ergodic nor spatially homogeneous. Jefferys (1987) shown that these effects are caused by wave components that propagate in multiple directions with identical frequencies, which produces an artificial phase locking in any given realization. As a consequence, the average wave power in a frequency band will vary over space from approximately zero to four times its mean value. The phase lock phenomenon is one of the basic properties of all the double summation models.

b) Single Summation Model

The other approach to synthesize a directional sea is to superpose each sinusoidal component with a unique frequency together. The propagate direction of each

component is selected based on the target directional spreading function. This will produce a spatially homogeneous wave field. The single summation model is defined by

$$\eta(x,y,t)=\sum_{i=1}^{N} a_i \cos\left[\sigma_i t - k_i\left(x\cos\theta_i + y\sin\theta_i\right)+\delta_i\right]. \tag{6.17}$$

As opposed to the double summation model, it takes a small band of frequencies to describe the directional spreading properties. It is required that the frequency increment in wave generation, Δf_g, is much smaller than the that used in the decomposition of a wave field into wave components, $\Delta f_d = 1/T$, where T is the duration of wave records used in the decomposition. In a frequency band, Δf_d, the directional spreading properties could be simulated.

The selection of direction of propagation of each frequency component with a frequency increment of Δf_g can be made in several ways. One of them introduced by Sand and Mynett (1987) is described below. The direction is randomly selected following a mapping procedure shown in Figure 6.5. The curve shown in Figure 6.5 is the cumulative distribution of wave direction calculated based on a given directional spreading function. A random number following the uniform distribution $U(0,1)$ is selected and then the corresponding direction θ_i is obtained through the mapping shown in the figure. For a narrow and symmetric directional distribution the cumulative function becomes rather steep around 0.5, so that the directions close to the mean wave direction θ_M are more likely to be selected. If the number of wave components in a frequency band, Δf_d is large enough, the target spreading function could be reproduced very well.

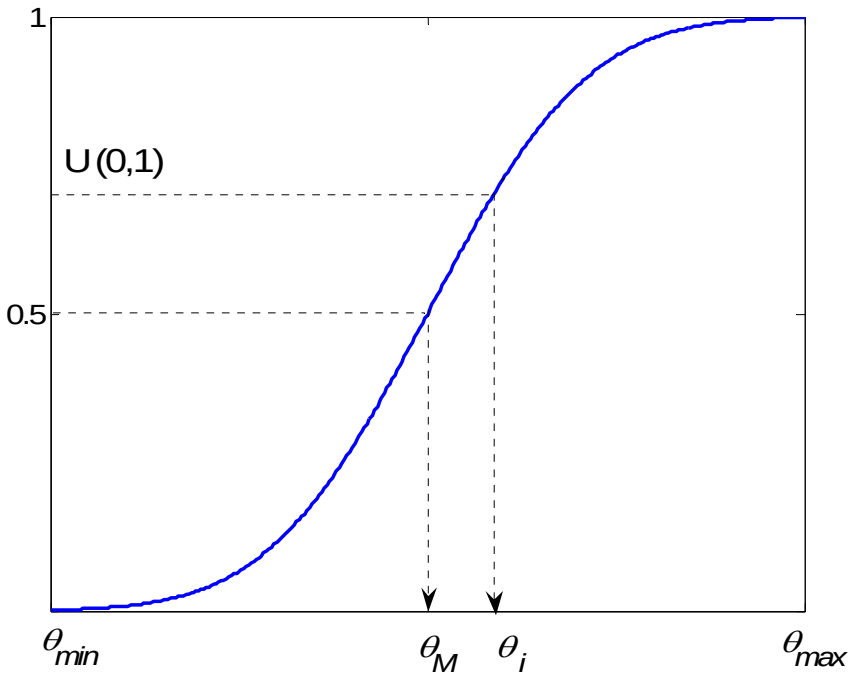

Figure 6.5: Random selection of direction of each free wave component

6.4.2 Numerically Generated Time Series

Before applying the proposed approach to the measurements of ocean waves, it is desirable to examine its accuracy and consistency under ideal conditions, that is, applying it to numerically simulated wave records which are free of measurement noises and errors due to the assumptions made in computing wave characteristics. Based on the time series of a wave field simulated following a cosine-2s spreading function of prescribed values of s and θ_M , the corresponding values of s and θ_M can be estimated using the proposed and conventional approach, respectively. The comparison between the estimated and the prescribed directional spreading parameter and mean wave direction may divulge the accuracy of the proposed approach and its superiority over the conventional approach. It is important to emphasize that the simulated wave records used as the input to the two approaches are time series recorded at a fixed point,

resembling the measurements of ocean waves made by a pitch/roll buoy or a PUV. In some previous studies of data adaptive methods (for example, Isobe et al, 1984, Hashimoto, 1997), cross spectra were calculated directly based on a prescribed directional spreading function and used as the input to numerical tests. Of course, the use of the cross spectra directly calculated based on a prescribed directional spreading function avoids the error resulting from the interaction term as described in Section 6.2, which may make the comparison look better. In our opinion, however, such numerical tests are unrealistic because the measurements of ocean waves in overwhelming majority cases are in the form of time series and its spreading function is not known in advance.

To generate homogenous directional seas within the scope of linear theory, a single summation over the frequency domain is used to superpose individual wave components consisting of a directional wave field. A directional irregular wave field of a prescribed 2s-cosine spreading function at frequency $f_k = 11/128$ Hz is generated using 1025 wave components evenly distributed within the frequency band between 10/128 and 12/128 Hz ($\Delta f_g = 2^{-16}$ Hz and M = 512). Hence, the time series of the generated resultant wave field at a fixed point have non-repeated duration of 65,536 sec (about 18.2 hour). The amplitude of these 1025 wave components are chosen to be the same and their initial phases are randomly selected between $-\pi$ to π. Making use of an approximation for large s (Tucker and Pitt, 2001)

$$\cos^{2s}\frac{\theta-\theta_M}{2} \approx \exp\left[-\frac{(\theta-\theta_M)^2}{4/s}\right]. \tag{6.18}$$

The directions of the 1025 components are randomly assigned following a normal distribution of the mean of θ_M and variance of $2/s$, which can be conduced more conveniently than the procedure shown in Figure 6.5 with the help of random normal

number generator in MATLAB. Figure 6.6 shows that the above approximation holds well for $s \geq 5$.

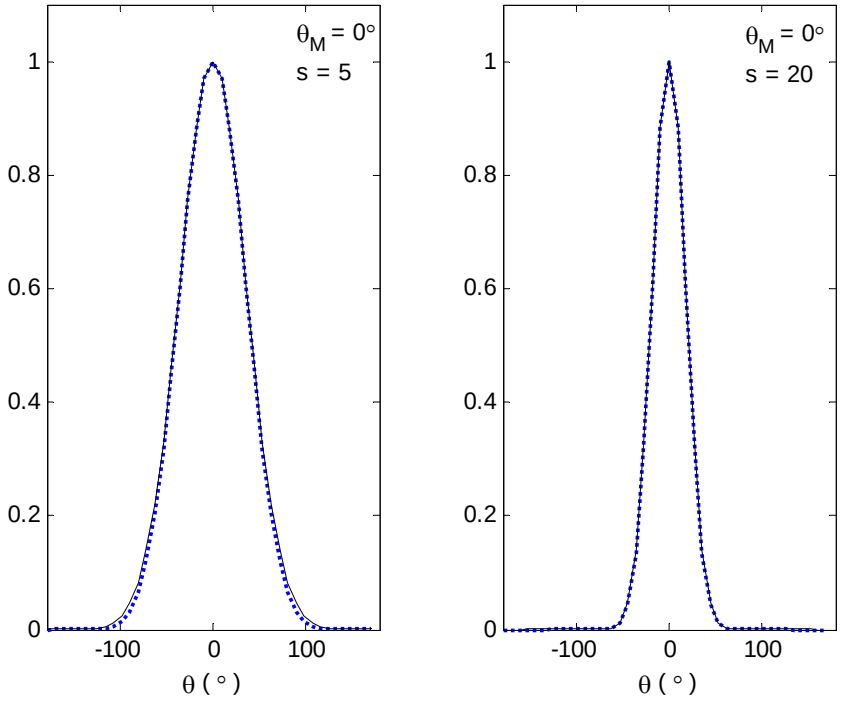

Figure 6.6: Comparison of cosine-2s models with the corresponding normal distributions. (..... denotes $\cos^{2s}\frac{\theta-\theta_M}{2}$, ——denotes $\exp\left[-\frac{(\theta-\theta_M)^2}{4/s}\right]$)

In the following numerical tests, the time series of four resultant wave fields of different directional spreading parameters s = 5, 10, 15 and 20 are generated. These values of s cover the range of the spreading parameter of majority ocean waves near their spectral peak frequencies (Mitsuyasu et al., 1975, Hasselman et al., 1980). In all four resultant

wave fields, the mean wave direction remains the same, $\theta_M = 0^\circ$. It will be show that the use of the mean wave directions other than 0° does not substantially alter the findings made in our numerical tests. Once the time series of a directional wave field are generated, we apply the FFT to them and then obtain the related cross spectra.

6.4.3 Statistics of Estimated Directional Spreading Parameters

Each wave field of a prescribed spreading parameter was simulated 100 times and each simulation (run) is realized by a set of randomly selected initial phases and directional angles as described in Section 6.4.2. In each run, the time series of wave induced pressure and two horizontal velocity components were recorded at 5 m below the still water level and those of wave elevation and two wave slopes in the *x*- and *y*-axis at the still water level. It is understood that the wave slope at the still water level does not exist when the wave elevation is negative and thus they are recorded as the extension of related wave slopes based on linear wave theory. Although the total non-repeated duration of time series is about 18 hours, we only use a 20-minute section of time series in the numerical tests, resembling the length of most field measurements. Each time series is divided into 17 segments of 128-sec long and with a 50% overlap. Because of the overlap, the equivalent degree of freedom (EDF) is reduced to 23 from 34 (Welch, 1967). Applying the proposed and conventional approach, respectively, to the averaged cross spectra, we obtain estimated spreading parameter s and mean direction θ_M for each run of a resultant wave field. Based on the results of 100 runs of a simulated wave field, we are able to obtain the mean and variance of s_1, s_2, θ_{M1} and θ_{M2} of each simulated wave field. The comparisons of the estimated and prescribed spreading parameter and mean wave direction based on the PUV records are similar to those based on the pitch/roll buoy records. For brevity, we only present the comparisons based on the pitch/roll buoy records in Table 6.2 – Table 6.4. To confirm our computation on the statistics of estimated spreading parameter and mean wave direction using the conventional approach, also included in Table 6.2 and Table 6.4 are the corresponding

ones calculated based on the Long (1980) after a printing error in his equation (Eq-19) for computing the standard deviation of s_1 was corrected. His equations for computing the related statistics were derived based on the assumptions that the errors resulting from the interaction term obey a normal distribution and can be approximated by linearization. When the EDF is large enough, the *chi-square* distribution becomes symmetric and closes to a normal distribution, as evidenced in Figure 6.2. Therefore, the standard deviations estimated using the conventional approach should be close to the corresponding ones computed based on Long (1980), which is confirmed in Table 6.2 and Table 6.4.

Table 6.2: Statistics of estimated θ_M ($s = 10$, $\theta_M = 0^\circ$, EDF = 23).

Method	θ_{M1} ($^\circ$)		θ_{M2} ($^\circ$)	
	Mean	Std. Deviation	Mean	Std. Deviation
Long (1980)	0	5.402	0	6.994
Conventional Approach	0.5260	6.437	0.5424	8.258
Proposed Approach	0.5436	4.580	0.5700	5.051

Table 6.3: Mean of the estimated s ($\theta_M = 0^\circ$, EDF = 23).

s	s_1		s_2	
	Con.	Prop.	Con.	Prop.
5	4.93	4.64	5.57	4.61
10	10.16	10.34	10.70	10.17
15	16.00	15.81	16.72	15.61
20	21.94	21.86	22.89	21.69

Table 6.4: Standard deviation of the estimated s ($\theta_M = 0^\circ$, EDF = 23).

s	s_1			s_2		
	Long	Con.	Prop.	Long	Con.	Prop.
5	1.97	2.00	1.34	2.89	2.86	1.33
10	4.25	4.38	2.79	5.19	5.25	2.81
15	6.84	7.02	3.12	7.93	8.06	3.13
20	9.21	8.89	5.03	10.53	10.20	5.05

It is found that the estimated mean directions of θ_{M1} and θ_{M2} by both approaches are consistent and in excellent agreement with the prescribed θ_M. For example, the statistics of the estimated mean wave direction given in Table 6.2 for the case of s = 10 and $\theta_M = 0^\circ$ indicate that the accuracy of the mean wave direction predicted by both approaches is indeed excellent and the proposed approach produces slightly better results than the conventional approach. Consequently, our attention hereafter focuses on the comparisons of estimated and prescribed spreading parameter. As shown in Table 6.3, the mean of s_1 and s_2 predicted by both approaches is in satisfactory agreement with the corresponding prescribed value. It is noticed that the mean values of s_2 are consistently

and noticeably greater than those of s_1 when they are estimated using the conventional approach. The proposed approach gives significantly smaller standard deviations of estimated s_1 and s_2 than the conventional approach, as shown in Table 6.4. The standard deviations of s_1 estimated using the proposed approach is about 42% in average smaller than those estimated using the conventional approach. In the case of s_2, the average reduction in the standard deviation is even greater, about 53%. It is also observed in Table 6.4 that the standard deviations of s_1 and s_2 estimated by both approaches increase with the increase in s, which is expected because when s is large it is very sensitive to a small change in Fourier coefficients. As a result, a small error in the average cross spectrum may result in large error in the estimation of spreading parameter.

Large standard deviations of s_1 and s_2 may result in inconsistency between estimated s_1 and s_2. This inconsistency was reported previously in using the conventional approach (Hasselmann et. al., 1980, Ewing and Laing, 1987). The large discrepancy between them was one of the major reasons to discard certain estimates of the spreading parameter of oceans waves (Wang and Freise, 1997). To examine the consistency between them predicted by these two approaches, we plotted s_1 against s_2 of all runs of four simulated wave fields predicted by the conventional and proposed approach in Figure 6.7. Overall, the consistency between s_1 and s_2 shown in Figure 6.7b is excellent as all points are close to the diagonal line, especially when the value of the prescribed spreading parameter is large. On the other hand, the consistency between s_1 and s_2 shown in Figure 6.7a is unsatisfactory and in general s_2 is greater than s_1, especially in the cases of small prescribed spreading parameters. The inconsistency between s_1 and s_2 predicted using the conventional approach is not unique to the pitch/roll wave records. It was also observed in the case of PUV wave records.

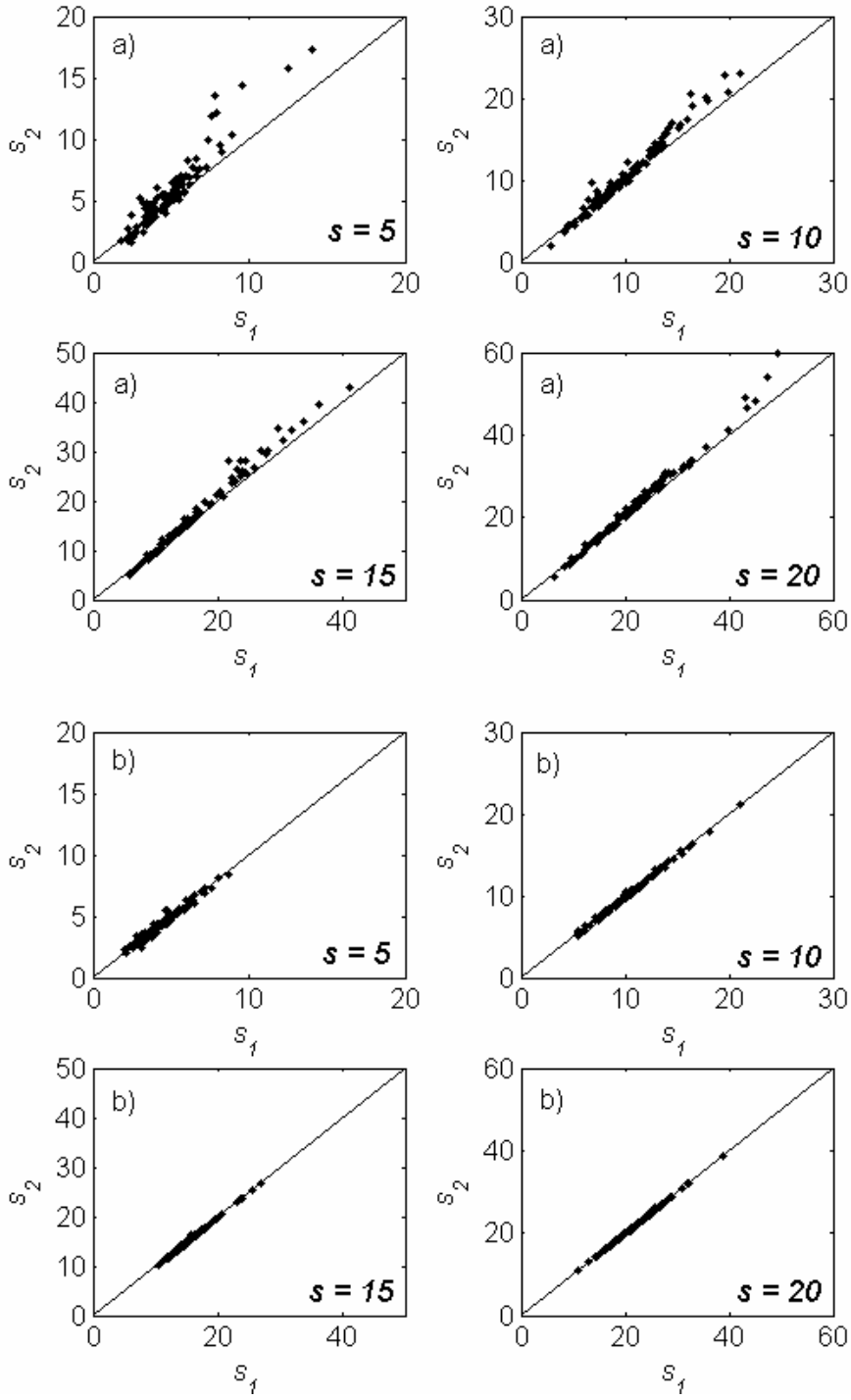

Figure 6.7: s_1 vs. s_2 (EDF = 23)

a): using the conventional approach; and b) using the proposed approach.

Because the prescribed mean wave direction has been kept zero in our numerical tests and one of recoded wave properties happens to be in the x-direction, one may wonder whether the trend observed in the above comparison of the statistics will change if the prescribed mean wave direction is different from 0° or 90°. To answer this question, three additional prescribed mean wave directions ($\theta_M = 30^\circ, 45^\circ$ and 60°) were used to simulate a resultant wave field of a prescribed spreading parameter s = 15. Same as in the previous numerical tests, 100 runs were performed for each prescribed mean wave direction. The related statistics are presented in Table 6.5 and Table 6.6. They confirm that the statistics are virtually independent of the choice of prescribed mean wave direction.

Table 6.5: Mean of estimated s and θ_M for different wave directions (s =15, EDF = 23).

$\theta_M\,(^\circ)$	s_1		s_2		$\theta_{M1}-\theta_M\,(^\circ)$		$\theta_{M2}-\theta_M\,(^\circ)$	
	Con.	Prop.	Con.	Prop.	Con.	Prop.	Con.	Prop.
30	15.68	15.92	16.44	15.74	0.39	0.42	0.47	0.45
45	16.05	15.46	16.77	15.26	0.10	-0.07	0.32	-0.07
60	16.21	16.01	16.92	15.81	0.26	0.00	0.29	-0.02

Table 6.6: Standard deviation of estimated s and θ_M for different wave directions (s =15, EDF = 23).

θ_M (°)	s_1		s_2		θ_{M1} (°)		θ_{M2} (°)	
	Con.	Prop.	Con.	Prop.	Con.	Prop.	Con.	Prop.
30	6.64	3.81	7.87	3.83	4.38	3.41	5.18	3.51
45	6.54	3.50	7.50	3.53	4.93	3.96	5.82	4.04
60	6.66	3.90	7.81	3.94	4.64	3.41	5.47	3.53

To substantiate the results stated in Section 6.2 that the probability for a small normalized error increases when the number of segments used in producing the average cross spectra becomes greater, here we fully made use of the numerical time series of duration about 2 hours. Each time series was divided into 111 segments of 128-sec and with a 50% overlap. Therefore, the corresponding average cross spectra have the EDF of about 148. Given in Table 6.7 are the standard deviations of estimated s_1 and s_2 using the proposed and conventional approach respectively. The standard deviations given by both approaches decrease significantly in comparison with those in Table 6.4. Furthermore, the standard deviations given by the conventional approach are closer to those of Long (1980), which is anticipated because of a much larger number of EDF (148) in this case. The consistency between s_1 and s_2 of all four resultant wave fields is plotted in Figure 6.8a for the conventional approach and in Figure 6.8b for the proposed approach. In comparison with Figure 6.7a and Figure 6.7b, Figure 6.8a shows significant improvement in the consistency between s_1 and s_2 estimated using the conventional approach while a smaller improvement is observed in Figure 6.8b. The improvement observed in Table 6.7 and Figure 6.8 shows that the reduction in the error of the estimated cross spectra greatly reduces the errors in estimating the spreading parameter when the conventional approach is used but only marginally improves the estimates

when the proposed approach is used. This observation suggests that the proposed approach is less sensitive to the errors involved in the estimated cross spectra than the conventional approach. This advantage of the proposed approach becomes more crucial in its application to field measurements. It is because not only the computation of the cross spectra based on field measurements involves errors resulting from factors other than the interaction term but also the duration of time series, namely, the number of cross spectra used in producing their averages is limited due to the assumption of stationary seas.

Table 6.7: Standard deviation of the estimated s ($\theta_M = 0^\circ$, EDF = 148).

s	s_1			s_2		
	Long	Con.	Prop.	Long	Con.	Prop.
5	0.68	0.73	0.53	0.94	0.96	0.53
10	1.45	1.41	1.00	1.72	1.68	1.00
15	2.30	2.58	1.54	2.60	2.88	1.55
20	3.17	3.53	2.00	3.52	3.90	2.00

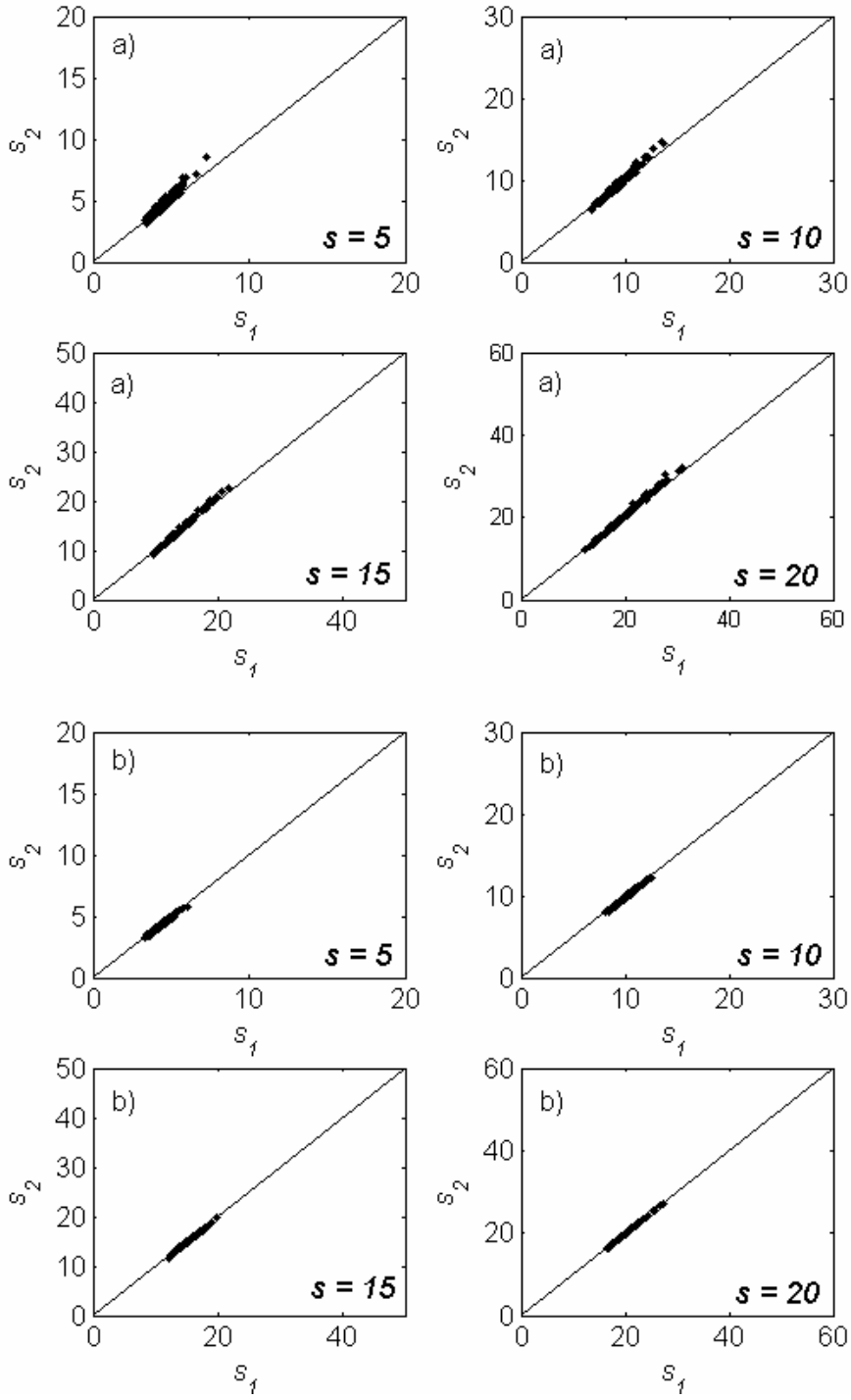

Figure 6.8: s_1 vs. s_2 (EDF = 148)

a) using the conventional approach; and b) using the proposed approach

6.5 WACSIS Data Analysis

According to the WACSIS database, the S4ADW current meter was deployed 11.5 m below the mean sea level, measuring the two horizontal velocity components and pressure. Wave information was also collected by a directional Waverider buoy measuring three components of wave induced acceleration, which was moored about 1 km to the north of the platform. Comprehensive description of the WACSIS and its measurement are referred to Chapter 3. The measurements recorded by the S4ADW and Waverider are used here to examine the accuracy and consistency of the two approaches in estimating the directional spreading parameter and mean wave direction. Since second-order wave-wave interactions mainly affect wave characteristics in the frequency ranges relatively low or high with respect to the spectral peak frequency (Zhang et al, 1996), to exclude the errors resulting from the neglect of second-order nonlinear wave-wave interactions in this study we mainly focus our attention to the estimate of the directional spreading parameter and mean direction of waves at the spectral peak frequency. It is known that the spreading parameter at the spectral peak reaches the maximum and decreases away from the peak frequency (Mitsuyasu et al., 1975; Hasselmann et al., 1980). To demonstrate the efficacy of the proposed approach not limited to the measurements at the spectral peaks, we also estimate the spreading parameters at frequencies at the entire frequency domain using both approaches.

All available data sets recorded by the S4ADW and Waverider were screened based on the following three criteria. First, if a data set involves a lot of abnormal spikes which were observed in some velocity records made by the S4ADW, the related data set was excluded in this study. Secondly, when the velocity component of ocean currents in the mean wave direction is significant with respect to the wave phase velocity at the spectral peak frequency, the observed (or appearance) wave frequency can be significantly different from the corresponding intrinsic frequency due to the Doppler effect, which may result in large errors in estimating wave directional spreading unless the effect of current is properly accounted for (Forristall and Ward, 1978). Hence, when the projected

current velocity in the mean wave direction is greater than 5% of the phase velocity at the spectral peak, the related data sets were discarded. Thirdly, the consistency between the estimated θ_{M1} and θ_{M2} is excellent if the directional spreading function of a wave field is of uni-modal, as evidenced in our previous numerical tests. It is also known that the estimated mean wave directions (θ_{M1} and θ_{M2}) of a wave field of bi- or multi-modal directional spreading are significantly different. Therefore, significant differences between them can be viewed as a vital sign of the sea states of bi- or multi-mode directional spreading. Hence, if the difference between the θ_{M1} and θ_{M2} estimated using the conventional approach is greater than 10°, the related wave field is thought to be bi- or multi-modal and should not be modeled by a cosine-2*s* spreading function. The related data sets were consequently rejected as well. It is noted that the cases rejected due to the difference between θ_{M1} and θ_{M2} being greater than 10° are very few in the WACSIS data sets, accounting for about 3.4% of cases considered in our study.

After screening, we had 85 cases available to our study, each of which was recorded by both S4ADW and Waverider. The related data sets were used as the input to the two approaches for the estimate of the spreading parameter and mean wave direction. The ratio of the projecting current to the phase velocity and the significant wave height of 85 selected cases are summarized in Figure 6.9. Each data set involves a 20-min time series of a sampling rate at 2 Hz. Similar to our numerical tests, for obtaining the average cross spectra each 20-min time series was divided into 17 segments of 128-sec duration and a 50% overlap between two consecutive segments.

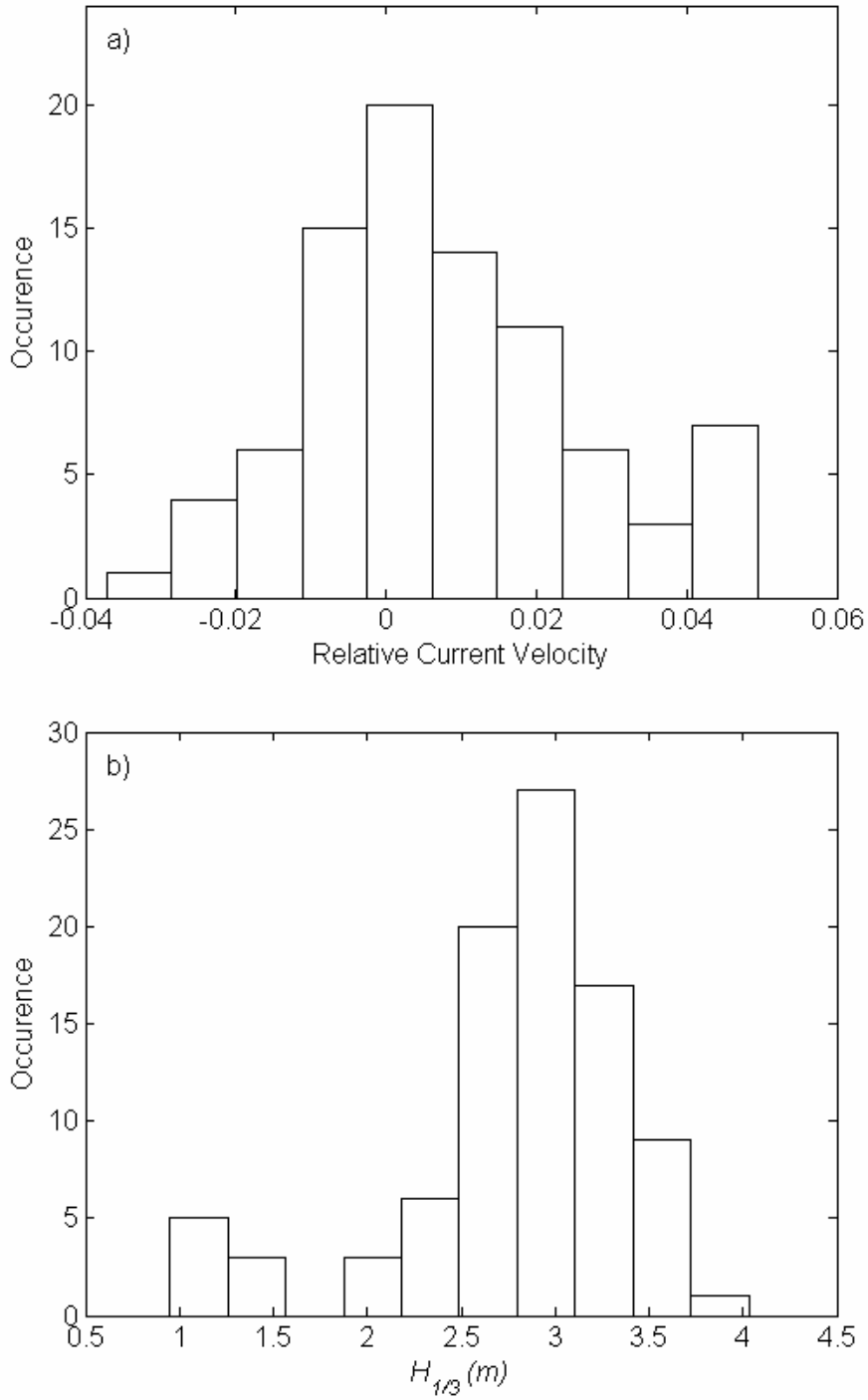

Figure 6.9: Histogram of a) ratio of the projecting current velocity in the mean wave direction to the phase velocity; and b) significant wave height.

6.5.1 Data Sets Recorded By the Directional Waverider Buoy

Unlike a pitch/roll buoy measuring the vertical acceleration and two wave slopes in the *x*- and *y*-direction, the directional Waverider buoy measures three acceleration components (vertical, north and west). Three measured acceleration components were then integrated twice in the time domain to render three corresponding components of the particle displacement, which were given in the WACSIS database. Consistent with linear wave theory, we assumed that the three components of the displacement were recorded at a fixed point at the mean sea level. The first and second Fourier coefficients of the directional spreading function of a measured wave field were calculated following Eq. (6.2) in using the conventional approach.

The spreading parameters, s_1 and s_2, and mean wave directions, θ_{M1} and θ_{M2} at the spectral peaks, estimated using the two approaches, respectively, are compared in Figure 6.10 and Figure 6.11. Similar to the trend observed in the related numerical tests, the consistency between s_1 and s_2 estimated using the proposed approach is excellent, virtually all points falling near the diagonal line as shown in Figure 6.10b. On the other hand, Figure 6.10a shows that the consistency of the conventional approach is poor and s_2 is in general greater than s_1. Almost all the estimated *s* falls in the range from 5 to 20 in using the proposed approach. While most estimated *s* using the conventional approach falls in that range, in about 18% cases, s_1 estimated using the conventional approach is significantly greater than 20, which is too great and hence may be erroneous. The consistency between θ_{M1} and θ_{M2} is satisfactory as observed in Figure 6.11, although that given by the proposed approach is slightly better. The satisfactory consistency may partially results from the exclusion of the data sets in which the difference between θ_{M1} and θ_{M2} estimated using the conventional approach is greater than 10°. Although the trends observed in these two figures are based on the field measurements, they are very similar to those observed in the numerical tests.

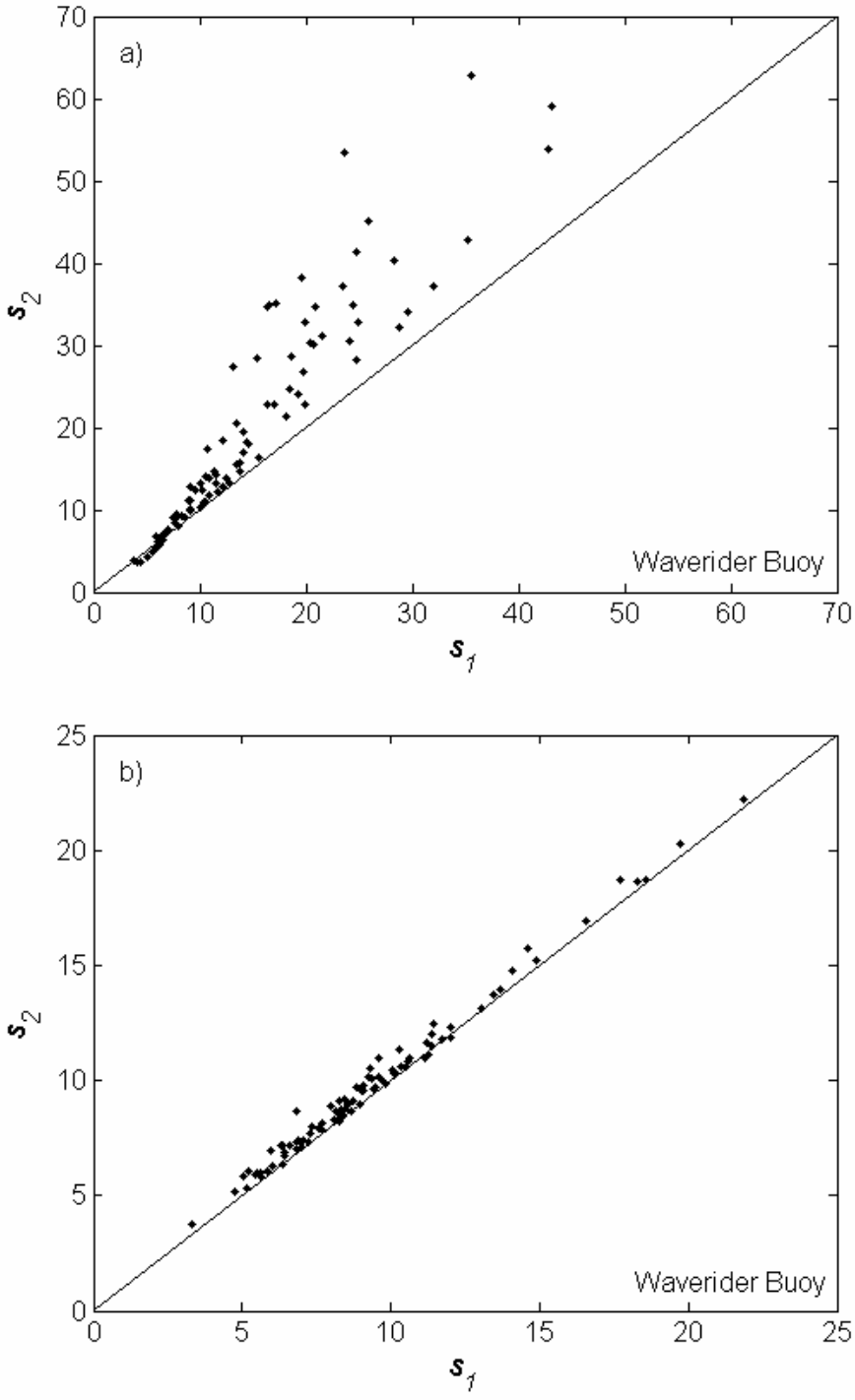

Figure 6.10: s_1 vs. s_2 estimated from Waverider data.

a) using the conventional approach; and b) using the proposed approach

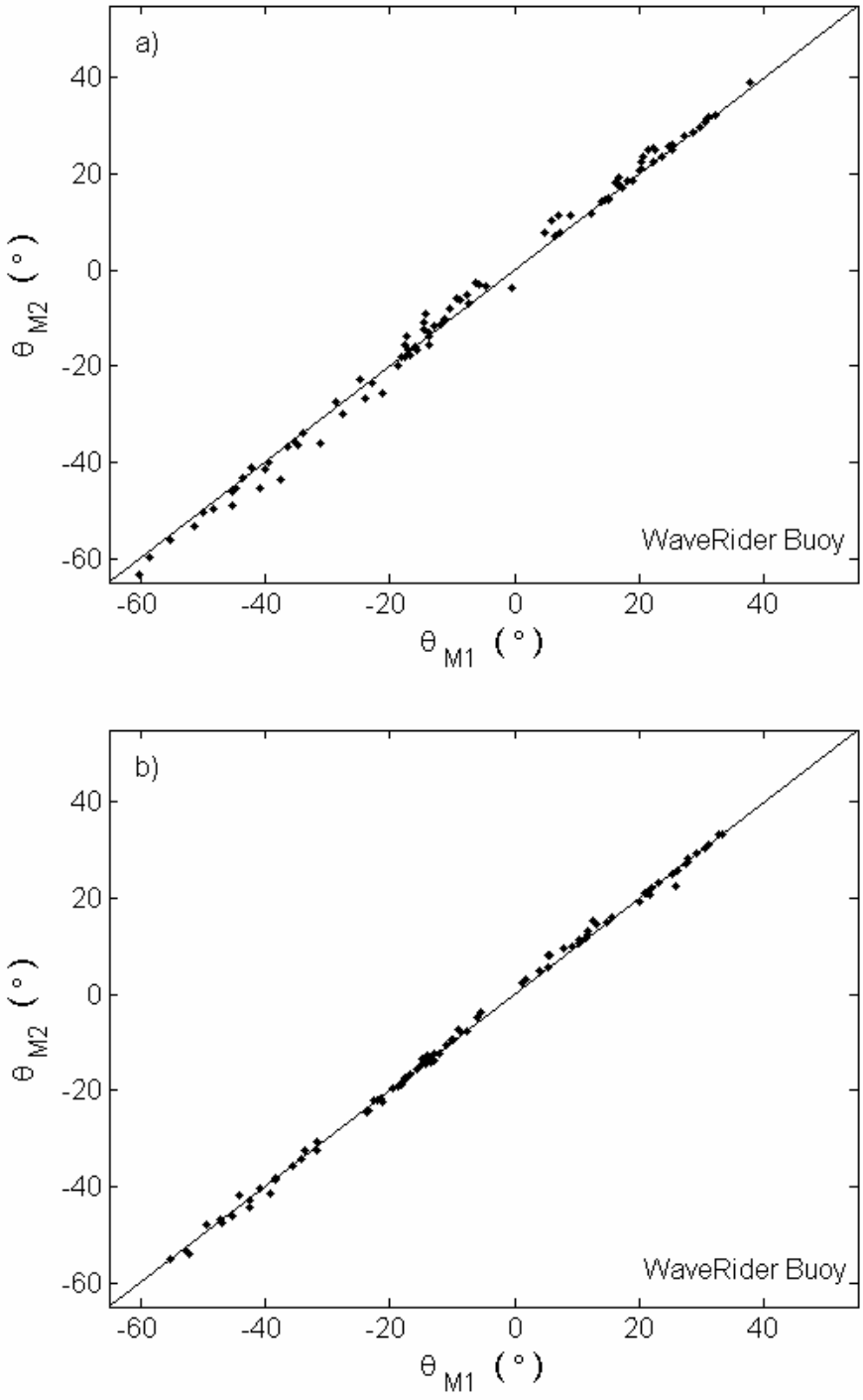

Figure 6.11: θ_{M1} vs. θ_{M2} estimated from Waverider data.

a) using the conventional approach; and b) using the proposed approach.

6.5.2 Estimation Based On the PUV

In applying the conventional approach, Eq. (6.2) was used to compute the Fourier coefficients except that Q_{12} and Q_{13} are replaced by C_{12} and C_{13}, respectively, where subscripts 1, 2 and 3 denote wave pressure, and the *x*- and *y*-axis velocity components. The related results are plotted in Figure 6.12 and Figure 6.13. As observed in Figure 6.12, the consistency between s_1 and s_2 estimated using the proposed approach remains excellent while that given by the conventional approach is rather poor. The estimated values of s_2 are in general greater, and some are significantly greater than those of s_1 in using the conventional approach. The consistency between estimated θ_{M1} and θ_{M2} is satisfactory. In short, the general trends observed in the cases of the PUV records are similar to those in the cases of the Waverider records. However, the consistency of either approach is slightly deteriorated in comparison with the corresponding one in the cases of the Waverider records.

6.5.3 Spreading Parameters at Frequencies Away From the Spectral Peaks

The directional spreading parameter *s* depends on the wave age and frequency. Previous studies (Hasselmann et al., 1976, Hasselmann et al., 1980, and Young, 1994) suggested that the dependence of directional spreading parameter s on wave age should be small. Therefore, we only discuss the dependence of *s* on wave frequency. Hasselmann et al. (1980) proposed a formula for directional spreading *s* at different frequency on the basis of JONSWAP experiment,

$$\frac{s}{s_p} = \left(\frac{f}{f_p} \right)^{\mu} \tag{6.19}$$

s_p is the directional spreading parameter at peak frequency.

For $f \geq 1.05 f_p$,

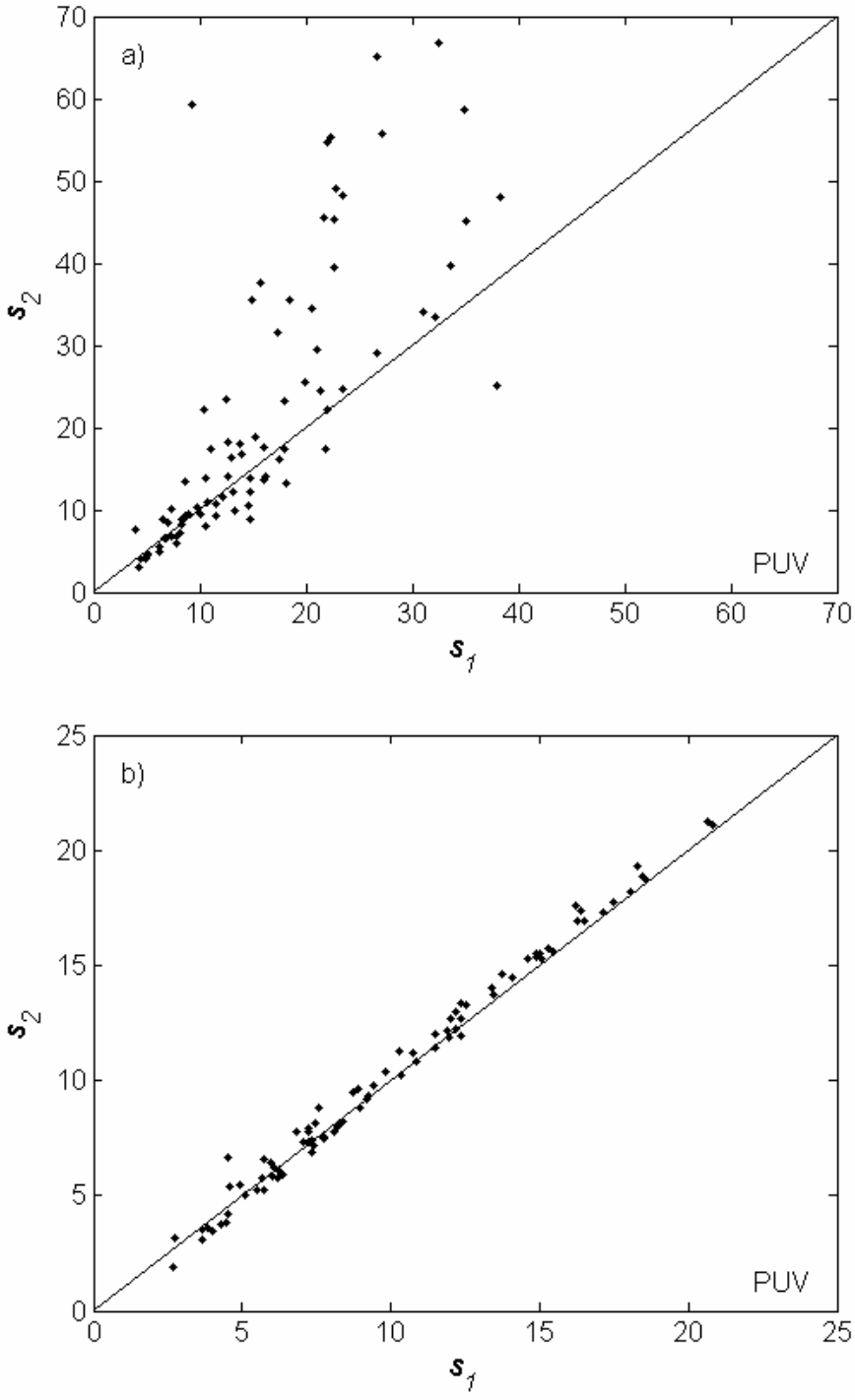

Figure 6.12: s_1 vs. s_2 estimated from PUV data.

a) using the conventional approach; and b) using the proposed approach

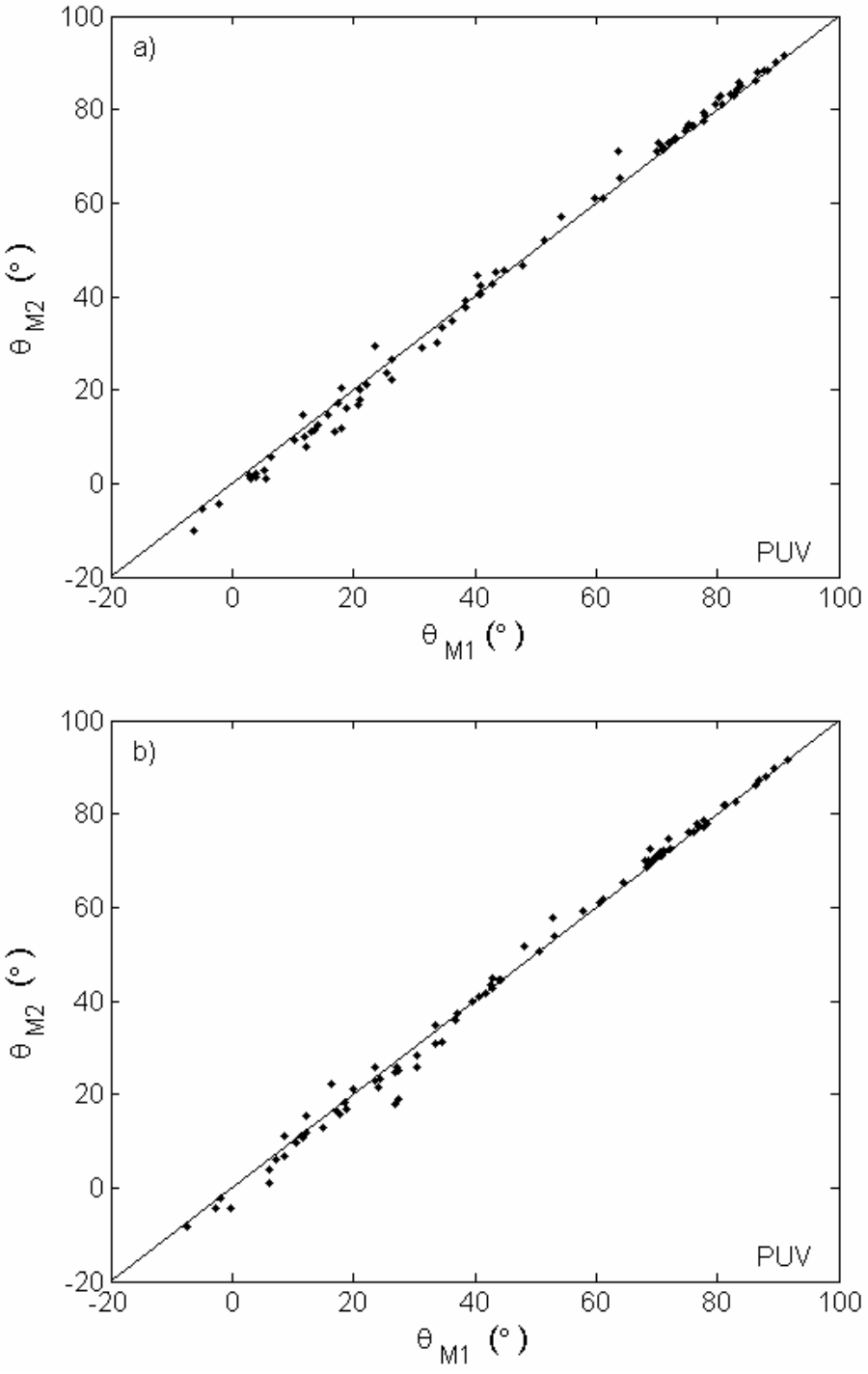

Figure 6.13: θ_{M1} vs. θ_{M2} estimated from PUV data.

a) using the conventional approach; and b) using the proposed approach

$$\begin{aligned} s_p &= 9.77 \\ \mu &= -2.33 - 1.45\left(U/c_p - 1.17\right); \end{aligned} \tag{6.20}$$

for $f < 1.05 f_p$,

$$\begin{aligned} s_p &= 6.97 \\ \mu &= 4.05 \end{aligned} \tag{6.21}$$

where, U_{10} is the wind speed and c_p the phase velocity at the peak frequency. It is better to indicate that Eqs. (6.19) – (6.21) is based on the regression analysis of the data collected by a pitch/roll buoy deployed in North Sea in a water depth of 22 m and U_{10}/c_p ranges from 1.0 to 1.8.

To show that the proposed approach can also improve the estimate of the spreading parameters at frequencies other than the peak frequency, both approaches were applied to the estimation of the spreading parameters in the entire frequency domain for five Waverider records. The five cases are named as 9802281120, 9803051100, 9803051120, 9803050500, and 9803050520. The significant wave heights, peak frequencies and ratios of wind speed to phase velocity at the peak frequency (U_{10}/c_p) of these cases are summarized in Table 6.8.

The dependence of the spreading parameter on the frequency in all five cases is similar. For brevity, only the results of estimated s_1 and s_2 for Case 9802281120 and 9803051100 are presented in Figure 6.14 and Figure 6.15, respectively depicting the estimated s_1 and s_2 using the conventional and proposed approaches as a function of the frequency normalized by the peak frequency. For the purpose of comparison, also plotted in the figures is the empirical curve given by Hasselmann et al. (1980). It is

observed that s_1 and s_2 estimated by both approaches reach the maximum near the peak frequency and decrease when the frequency moves away from the spectral peak. They are in satisfactory agreement with Hasselmann et al.'s formula. It is also observed that both s_1 and s_2 fluctuate with respect to the empirical curves. Nevertheless, the fluctuation amplitude is much smaller in using the proposed approach.

To examine the consistency between estimated s_1 and s_2, we also compare the results of five cases in Figure 6.16a for the conventional approach and Figure 6.16b for the proposed approach. The figures clearly show that the consistency of s_1 and s_2 estimated using the proposed approach is superior, similar to that observed in Sections 6.5.1. In general, the estimated s_2 is much greater than s_1 in using the conventional approach. The consistency between s_1 and s_2 estimated using the proposed approach is excellent in the entire range of the spreading parameters except for those of extremely small values ($s < 2$). The relatively large discrepancies mainly occur at very low or high frequency ranges where nonlinear second-order (difference-frequency and sum-frequency) bound waves are significant. It will be our future effort to find out whether or not the consistency can be improved after second-order bound waves are filtered from the measurements.

Table 6.8: Sea states of selected five cases.

Case	$H_{1/3}\ (m)$	$f_p\,(Hz)$	U_{10}/c_p
9802281120	3.14	0.1162	1.14
9803050500	3.39	0.1240	1.39
9803050520	3.42	0.1289	1.51
9803051100	3.42	0.1143	1.35
9803051120	3.10	0.1143	1.34

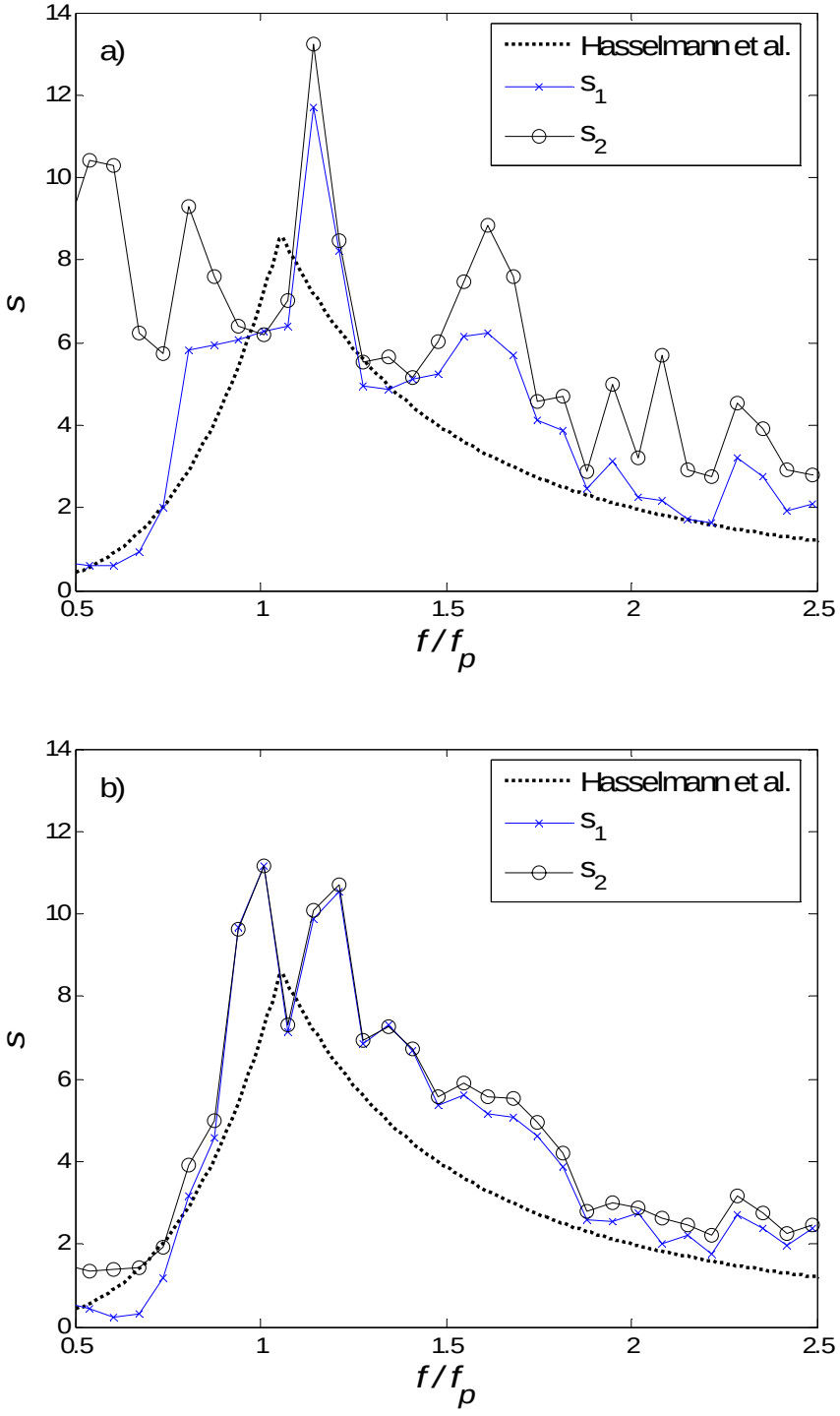

Figure 6.14: Dependence of s on f/f_p for Case 9802281120 ($U_{10}/c_p = 1.14$).

a) using the conventional approach; and b) using the proposed approach

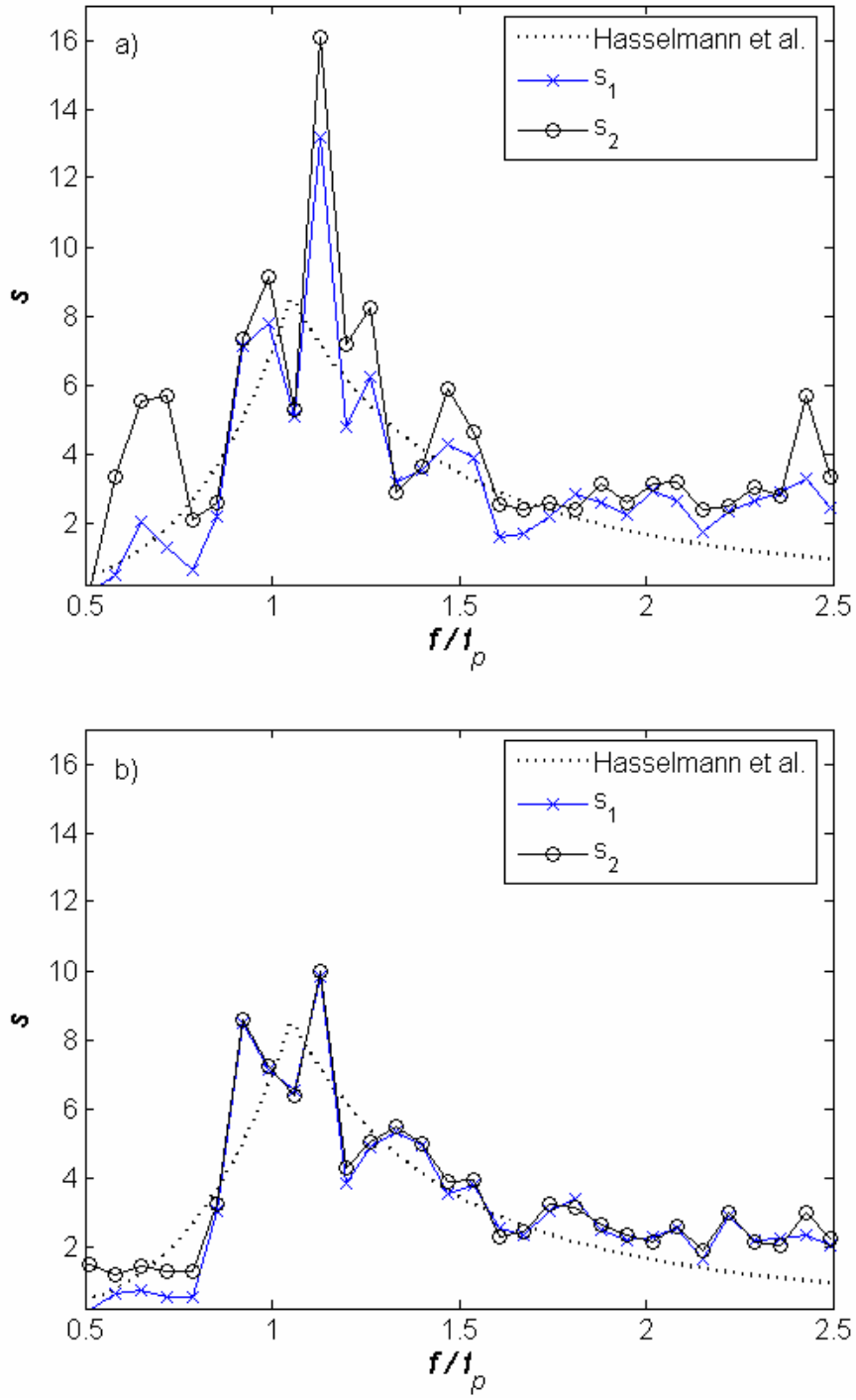

Figure 6.15: Dependence of s on f / f_p for Case 9803051100 ($U_{10} / c_p = 1.35$).

a) using the conventional approach; and b) using the proposed approach

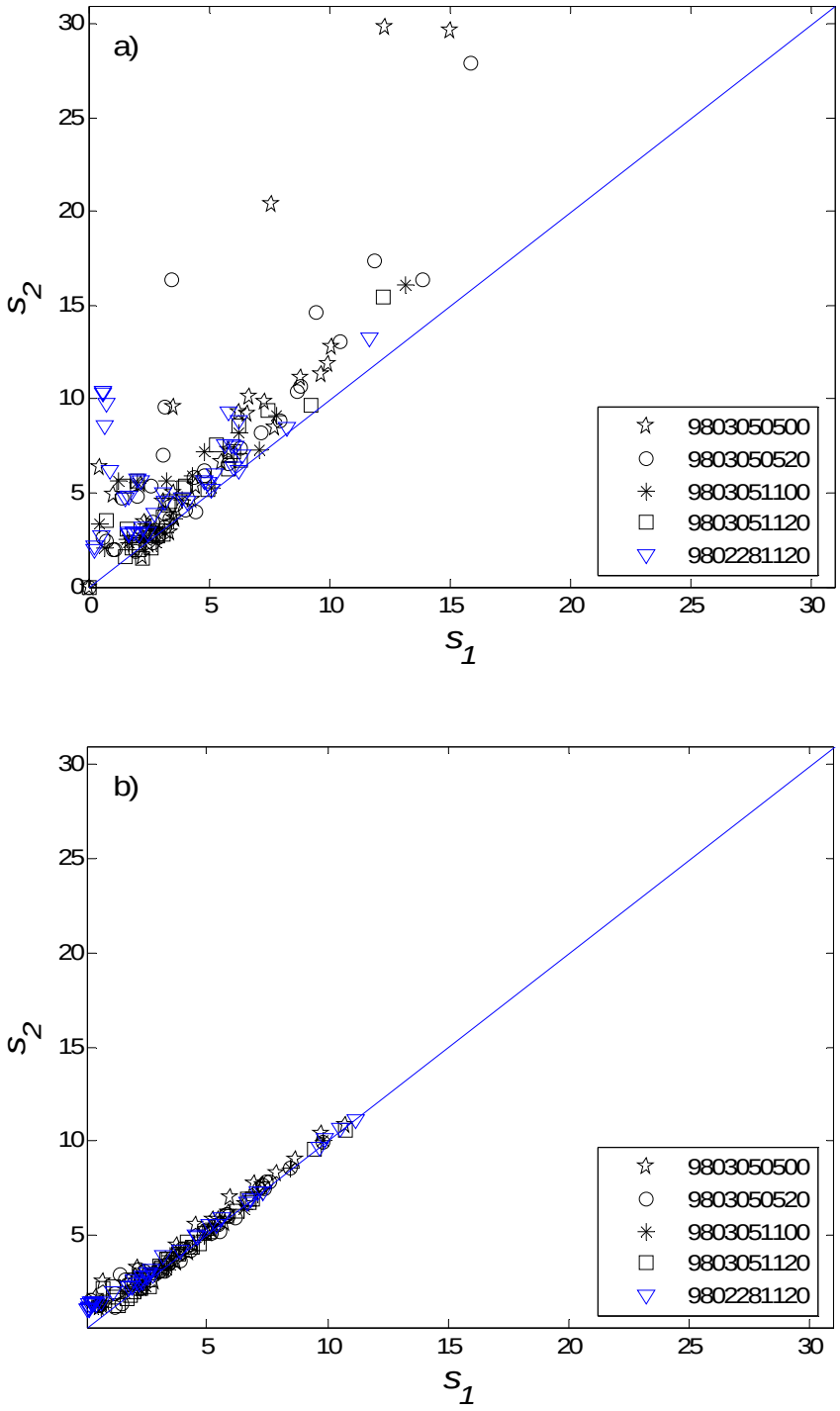

Figure 6.16: Scatter plots of s_1 and s_2 estimated in the entire frequency domain. a) using the conventional approach; and b) using the proposed approach

CHAPTER VII

CONCLUSIONS

The DHWM was applied to investigate the consistency of measurements recorded by different wave sensors likely at different locations. Three cases of relatively steep ocean waves from the WACSIS common database were selected for the analysis. The pressure head and two horizontal velocity components measured by a S4ADW were first examined for the synchronization. Then the synchronized time series were used as the input to the DHWM for the decomposition of measured wave fields into their free waves. The wave directions based on the S4ADW data set were compared with those obtained by the Directional Waverider Buoy. A 45° discrepancy between the two sets of wave directions over the entire frequency range was observed. The suspicion about the true orientation of S4ADW was substantiated through the comparison of the predicted wave directions based on the EBS data set. The concern of the true orientation of S4ADW was later relayed to the person responsible for installing the S4ADW sensor. He graciously admitted that the orientation of the S4ADW was likely wrong by about 45° due to the misunderstanding of the installation manual (Van, 2000). After the directions of free waves based on the S4 data sets were rotated 45° clockwise, the predicted wave elevations were in satisfactory agreement with the corresponding measurements by SAAB and Marex. Likewise, the predicted pressure and horizontal velocity based on the EBS data set were in excellent agreement with the measurements by S4ADW. The satisfactory comparisons also indicate that wave measurements by different sensors are consistent in the time domain, which is a more complete examination than traditional comparisons made between power spectra because the latter lacks the information of phases.

To analyze directional seas in the presence of strong currents, the original Directional Hybrid Wave Model (DHWM) was extended to allow for the presence of steady and uniform currents. Based on three or more independent wave records and the information of currents, the extended DHWM (C-DHWM) is able to decompose a directional irregular wave field into its free waves, in terms of their amplitudes, directions and initial phases as functions of the intrinsic frequency. Extensive numerical tests were conducted to examine the reliability and convergence of a C-DHWM, especially the iteration of deriving the intrinsic frequency in the presence of strong currents. It is found that the iteration for determining the intrinsic frequency is convergent when the initial guess of wave direction is within 45° of the true wave direction and the intrinsic frequency is below 0.2 Hz. If the current is smaller (say 1.0 m/s), the computation of the intrinsic frequency will be convergent even if the initial guess on the wave direction is 90° apart from the true direction. Through the comparison between the decomposition results obtained by applying a C-DHWM and DHWM respectively to numerically simulated waves as well as WACSIS field measurements, it is found that the extended wave model is reliable and convergent in the analysis of ocean waves in the presence of currents. The superiority of a C-DHWM to a DHWM mainly originates from the use of the intrinsic frequency to determining the corresponding wavenumber and transfer functions from wave pressure and velocities to elevations. Large errors resulting from neglecting currents may occur when the currents are relatively strong and in the opposite or following direction to that of waves. In using PUV records as input, depending on the opposite or following currents the wave amplitudes are under- or over- predicted using a DHWM especially in the high frequency range, in addition to energy shifts towards low or high frequencies. Significant errors in estimated wave direction as a function of the apparent frequency may appear at low and high frequencies if waves are steep. In using measured elevations as input, depending on the opposite or following currents, the wave energy predicted using a DHWM shifts towards low or high frequencies while related errors in estimated wave direction nearby the spectral peak are relatively small. When the currents are perpendicular to the main wave direction, the Doppler effects of currents

on the intrinsic frequency are negligible and consequently the use of a DHWM does not result in significant errors.

A new approach is proposed to estimate the directional spreading parameter *s* and mean wave direction θ_M of directional seas in this study. The accuracy and consistency of the proposed and conventional approaches were examined first at the spectral peak of a wave field whose wave records were either numerically generated or measured in situ. In the case of the input being numerically generated wave records, the comparison between the estimates and the related prescribed values indicates the proposed approach is statistically superior to the conventional approach, especially in estimating the directional spreading parameter *s*. Namely, the former renders almost unbiased mean and significantly smaller standard deviation in estimating the spreading parameter. When the field measurements were used as the input, the comparison between estimated s_1 and s_2 shows that the proposed approach results in substantially better consistency between them, which is consistent with the corresponding observation made in the numerical tests. Furthermore, the spreading parameters of waves at frequencies other than the peak frequency were also estimated using both approaches and are qualitatively consistent with the trend given by Hasselmann et al. (1980). The consistency between s_1 and s_2 estimated using the proposed approach at the frequencies other than the peak frequency is also found to be superior to that using the conventional approach. The consistency between estimated s_1 and s_2 is especially crucial in analyzing field measurements where the true spreading parameter of a measured wave field is not known. The employment of a data adaptive method (MLM) to estimate the directional spreading function and then its first two Fourier coefficients is the reason for the superiority of the proposed approach over the conventional approach. This is because a MLM is more tolerant of errors involved in the estimated cross spectra than the DFT used in the conventional approach. Although the average of the cross spectra may reduce errors, especially those resulting from the 'interaction' term, the reduction is limited by the duration of measured wave records and the requirements of resolution in the frequency domain. Hence, the use

of the proposed approach in estimating the directional spreading coefficients of ocean waves is strongly recommended. Because a cosine-2s model is intended to model the sea states of uni-mode directional spreading and the efficacy of the proposed approach is only examined in this scenario, it is not recommended to apply it to the sea states of bi- and multi-mode.

REFERENCES

Barstow, S. F., H. E. Krogstad, L. Lonseth, J. P. Mathisen, G. Mork, P. Schjølberg, 2004: Intercomparison of sea-state and zero-crossing parameters from the WACSIS field experiment and interpretation using video evidence, *Journal of Offshore Mechanics and Arctic Engineering*, **126**(1), 35-42.

Borgman, L.E., 1969: Ocean wave simulation for engineering design, *Journal of Waterways and Harbors Division, ASCE*, **95**, 557-583.

Cao, P. and J. Zhang, 1997: Slow motion response of compliant offshore structures. *Journal Offshore and Polar Engineering*, **7**, 119-126.

Cokelet, E.D. 1977: Step gravity waves in water of arbitrary uniform water depth. *Philosophical Transactions*, *Royal Society of London A*, **286**, 183-230.

Chen, L. & J. Zhang, 1998: On interaction between intermediate-depth long waves and deep-water short waves. *Journal of Ocean Engineering*, **25**, 395-423.

Earle, M. D., 1996: Nondirectional and directional wave data analysis procedures, *NDBC Technical Document 96-01*, 37 pp.

Ewing, J. A. and A. K. Laing, 1987: Directional spectra of seas near full development, *Journal of Physical Oceanography*, **17**, 1696-1706.

Forristall G.Z., S.F. Barstow, H.E. Krogstad, M. Prevosto, P.H. Taylor, P.S. Tromans, 2004: Wave Crest Sensor Intercomparison Study: An Overview of WACSIS, *Journal of Offshore Mechanics and Arctic Engineering*, **126**, 26-34.

———, K. C. Ewans, 1998: Worldwide measurements of directional wave spreading, *Journal of Atmospheric and Oceanic Technology*, **15**, 440-469.

———, E. G. Ward, 1978: The directional spectra and kinematics of surface gravity waves in tropical storm Delia, *Journal of Physical Oceanography*, **8**, 888-909.

Harris, F. J., 1978: On the use of windows for harmonic analysis with the discrete Fourier transform, *Proceedings of the IEEE*, **66**, 51-83.

Hashimoto, N., 1997: Analysis of the directional wave spectra from field data, *Advances in Coastal and Ocean Engineering,* Vol.3, World Scientific, Singapore, pp.103-143.

Hasselmann, K. 1962: On the nonlinear energy transfer in a gravity-wave spectrum, part 1, General theory. *Journal of Fluid Mechanics,* **12**: 481-500.

Hasselmann, D. E., M. Dunckel and J. A. Ewing, 1980: Directional wave spectra observed during JONSWAP 1973, *Journal of Physical Oceanography*, **10**, 1264-1280.

———, D. B. Ross, P. Muller and W. Sell, 1976: A parametric wave prediction model. *Journal of Physical Oceanography*, **6**, 200-228.

Hwang, P. A. and D. W. Wang, 2000: Airborne measurements of the wavenumber spectra of ocean surface waves. Part II: Directional distribution. *Journal of Physical Oceanography*, **30**, 2768-2787.

Isobe, M., K. Kondo, and K. Horikawa, 1984: Extension of MLM for estimating directional wave spectrum. *Proceeding of Symposium on Description and Modeling of Directional Seas*, Lyngby, Denmark, Danish Hydraulic Institute, A-6-1–A-6-15.

Jefferys, E. R., 1987: Directional sea should be ergodic, *Applied Ocean Research*, **9**, 186-191.

Jenkins, G. M., and D. G. Watts, 1968: *Spectra Analysis and Its Applications*. Holden Day, San Francisco, CA, 525pp.

Komen, G. J., L. Cavalieri, M. Donelan, K. Hasselmann, S. Hasselmann, and P.A.E.M. Janssen, 1994: *Dynamics and Modeling of Ocean Waves*. Cambridge University Press, New York, NY, 532pp.

Long, R. B., 1980: The statistical evaluation of directional spectrum estimates derived from pitch/roll buoy data. *Journal of Physical Oceanography*, **10**, 944-952.

Longuet-Higgins, M. S., 1987: The propagation of short surface gravity waves on longer gravity waves, *Journal of Fluid Mechanics,* **177**, 293-306.

Longuet-Higgins, M. S., D. E. Cartwright, and N. D. Smith, 1963: Observations of the directional spectrum of sea waves using the motions of a floating buoy, *Ocean Wave Spectra*, Prentice Hall, Englewood Cliffs, NJ, 111-132.

———, R. W. Stewart, 1960: Changes in the form of short gravity waves on long waves and tidal currents. *Journal of Fluid Mechanics,* **8**: 565-583.

Massel, S. R., R. M. Brinkman, 1998: On the determination of directional wave spectra for practical applications, *Applied Ocean Research*, **20**, 357-374.

Meza Conde, E., J. Zhang, and R.J. Seymour, 2000: Free-wave energy dissipation in experimental breaking waves, *Journal of Physical Oceanography*, **30**, 2404-2418.

Miles, M.D. and E.R. Funke, 1989: A comparison of methods for synthesis of directional seas, *Journal of Offshore Mechanics and Arctic Engineering*, **111**, 43-48.

Mitsuyasu, H., F. Tasai, T. Suhara, S. Mizuno, M. Ohkusu, T. Honda, and K. Rikiishi, 1975: Observation of the directional speactrum of ocean waves using a cloverleaf buoy, *Journal of Physical Oceanography*, **5**, 750-760.

Nakagawa, Y., H. Tsruuya, N. Hashimoto, 1996: The effects of currents on estimations of directional wave spectra, *Proceedings of Twenty-Fifth ICCE*, September 2-6, 1996, Orlando, Florida, Vol. **1** 30-42.

Panicker, N.N. and L.E. Borgman, 1970: Directional Spectra from Wave-gage Arrays, *Proceeding of 12th Coastal Engineering Conference*, Washington, D.C., Vol. **1**, 117-136.

Phillips, O. M. 1960: On the dynamics of unsteady gravity waves of finite amplitude, Part 1. *Journal of Fluid Mechanics,* **9**, 193-217.

———, 1979: Surface wave physics--A survey. *Flow Research Report*. **107**, 91pp.

Prevosto, M., 2002: Private communication via e-mail.

———, S.V. Iseghem, B. Moreau, and G. Z. Forristall, 2001: Wave crest sensor intercomparison study, Technique Report, Shell Global Solution, US, 139pp.

Sand, S. E., 1984: Deterministic decomposition of pitch-and-roll buoy measurements. *Coastal Engineering*, **8**, 243-263.

Sand, S. E., A. E. Mynett, 1987: Directional wave generation and analysis, *Proceedings of IAHR Seminar on Wave Analysis and Generation in Laboratory Basins*, Lausanne. Switzerland, Sep. 1-4, 1987, 209-235.

Schwartz, R.H. 1974: Computer extension and analytic continuation of Stokes' expansion for gravity waves. *Journal of Fluid Mechanics*, **62**, 553-578.

Skourup, J. and M. J. Sterndorff, 2002: Deterministic reproduction of nonlinear waves. *Proceedings of OMAE*, 28575, June 23-28, 2002, Oslo, Norway.

Spell, C. A., J. Zhang, & R. E. Randall, 1996: Hybrid wave model for uni-directional irregular waves, Part II: Comparison with laboratory measurements, *Applied Ocean Research,* **18**, 93-110.

Steele, K.E., 1997: Ocean current kinematic effects on pitch-roll buoy observations of mean wave direction and nondirectional spectra, *Journal of Atmospheric and Oceanic Technology*, **14**(2), 278-291.

Strong, B., B. Brumley, E.A. Terray, G.W. Stone, 2000: Performance of ADCP-derived directional wave spectra and comparison with other independent measurements. *Proceedings of Oceans 2000*, 1195-1203, Sep 11-14 2000, Providence, RI, USA.

Su, M. Y. & A. W. Green, 1981: Experimental studies of strong nonlinear interactions of deep-water gravity waves. *Wave Dynamics and Radio Probing of Ocean Surface*, Philips & Hasselmann Editors, Plenum, New York, 231-253.

Tucker, M. J., E. G. Pitt, 2001: *Waves in Ocean Engineering*. Elsevier Science Ltd.

Van, U., 2000, Private communication via e-mail.

Wang, H. T., C. B. Freise, 1997: Error analysis of the directional wave spectra obtained by the NDBC 3-m pitch-roll discus buoy, *IEEE Journal of Oceanic Engineering*, **22**(4), 639-648.

Welch, P. D., 1967: The use of fast Fourier transform for the estimation of power spectra, a method based on time averaging over short, modified periodgrams. *IEEE Trans. Audio Electro-acoustics*, Vol. AU-15, 70-73.

West, B.J., K.M. Watson, and A.J. Thomson, 1974: Mode coupling description of ocean wave dynamics, *Physics of Fluids*, **17**, 1059-1067.

Wheeler, J. D. 1970: Method for calculating forces produced by irregular waves, *Journal of Petroleum Technology,* **249**, 359-367.

Wyatta, L.R., J.J. Greena, K-W Gurgelb, B.J.C. Nieto, K. Reichert, et. al., 2003: Validation and inter-comparisons of wave measurements and models during the EuroROSE experiments, *Coastal Engineering*, **48**, 1 –28.

Young, I. R., 1994: On the measurement of directional wave spectra, *Applied Ocean Research,* **16,** 283–294.

Yuen, H.C. & B.M. Lake, 1982: Nonlinear dynamics of deep-water gravity waves, *Advanced Applied Mechanics,* **22**, 67-229.

Zhang, J. 1999: Hybrid wave models and their applications for steep ocean waves, *Marine Technology Society Journal*, **33**, 15-26.

———, 2005: Nonlinear wave interactions & their application to ocean science & engineering, Class Notes of OCEN 689.

———, J., L. Chen, M. Ye, and R.E. Randall, 1996: Hybrid wave model for unidirectional irregular waves, Part I: Theory and numerical scheme, *Applied Ocean Research*, **18**, 77-92.

———, K. Hong, and D.K.P. Yue, 1993: Effects of wavelength ratio on wave modeling, *Journal of Fluid Mechanics*, **248**, 107-127.

———, I. Prislin, J. Yang, and J. Wen, 1999: Deterministic wave model for short-crested ocean waves, Part II: Comparison with laboratory and field measurements, *Applied Ocean Research*, **21**, 189-206.

———, J. Yang, I. Prislin, J. Wen, and Hong, K., 1999: Deterministic wave model for short-crested ocean waves, Part I: Theory and numerical scheme, *Applied Ocean Research*, **21**, 167-188.

APPENDIX A

SOLUTIONS FOR PARTICLE VELOCITY AND DYNAMIC PRESSURE

A.1 MCM solutions

Wave induced particle velocity along *x*-axis:

$$u = u^{(1)} + u^{(2)} \tag{A.1}$$

where,

$$u^{(1)} = g\sum_{j=1}^{2}\frac{a_j}{\sigma_{I,j}}k_{x,j}\frac{\cosh\left[k_j(h+z)\right]}{\cosh(k_j h)}\cos\psi_j \tag{A.2}$$

$$\begin{aligned} u^{(2)} = {} & \frac{3}{4}\sum_{j=1}^{2}a_j^2\sigma_{I,j}k_{x,j}\frac{\cosh\left[2k_j(h+z)\right]}{\sinh^4\left(k_j h\right)}\cos 2\psi_j \\ & + \frac{a_1 a_2\sigma_{I,2}}{2}\left(k_{x,1}-k_{x,2}\right)A_{(-)}\frac{\cosh\left[\left|\overrightarrow{k_1}-\overrightarrow{k_2}\right|(h+z)\right]}{\cosh\left(\left|\overrightarrow{k_1}-\overrightarrow{k_2}\right|h\right)}\cos\left(\psi_1-\psi_2\right) \\ & + \frac{a_1 a_2\sigma_{I,2}}{2}\left(k_{x,1}-k_{x,2}\right)A_{(+)}\frac{\cosh\left[\left|\overrightarrow{k_1}+\overrightarrow{k_2}\right|(h+z)\right]}{\cosh\left(\left|\overrightarrow{k_1}+\overrightarrow{k_2}\right|h\right)}\cos\left(\psi_1+\psi_2\right) \end{aligned} \tag{A.3}$$

Wave induced particle velocity along *y*-axis:

$$v = v^{(1)} + v^{(2)} \tag{A.4}$$

where,

$$v^{(1)} = g\sum_{j=1}^{2}\frac{a_j}{\sigma_{I,j}}k_{y,j}\frac{\cosh\left[k_j(h+z)\right]}{\cosh(k_j h)}\cos\psi_j \tag{A.5}$$

$$\begin{aligned} v^{(2)} = {} & \frac{3}{4}\sum_{j=1}^{2}a_j^2\sigma_{I,j}k_{y,j}\frac{\cosh\left[2k_j(h+z)\right]}{\sinh^4\left(k_j h\right)}\cos 2\psi_j \\ & + \frac{a_1 a_2\sigma_{I,2}}{2}\left(k_{y,1}-k_{y,2}\right)A_{(-)}\frac{\cosh\left[\left|\overrightarrow{k_1}-\overrightarrow{k_2}\right|(h+z)\right]}{\cosh\left(\left|\overrightarrow{k_1}-\overrightarrow{k_2}\right|h\right)}\cos\left(\psi_1-\psi_2\right) \\ & + \frac{a_1 a_2\sigma_{I,2}}{2}\left(k_{y,1}-k_{y,2}\right)A_{(+)}\frac{\cosh\left[\left|\overrightarrow{k_1}+\overrightarrow{k_2}\right|(h+z)\right]}{\cosh\left(\left|\overrightarrow{k_1}+\overrightarrow{k_2}\right|h\right)}\cos\left(\psi_1+\psi_2\right) \end{aligned} \tag{A.6}$$

Wave induced dynamic pressure:

$$p = p^{(1)} + p^{(2)} \tag{A.7}$$

where,

$$\frac{p^{(1)}}{\rho g} = \sum_{j=1}^{2}a_j\frac{\cosh\left[k_j(h+z)\right]}{\cosh(k_j h)}\sin\psi_j \tag{A.8}$$

$$\begin{aligned} \frac{p^{(2)}}{\rho g} = {} & \frac{1}{4g}\sum_{j=1}^{2}\left[a_j^2\sigma_{I,j}^2\left(\frac{3\cosh\left[2k_j(h+z)\right]}{\sinh^4\left(k_j h\right)}-\frac{1}{\sinh^2\left(k_j h\right)}\right)\cos 2\psi_j\right] \\ & + \frac{a_1 a_2\sigma_{I,2}^2}{2g}\left(\lambda-1\right)A_{(-)}\frac{\cosh\left[\left|\overrightarrow{k_1}-\overrightarrow{k_2}\right|(h+z)\right]}{\cosh\left(\left|\overrightarrow{k_1}-\overrightarrow{k_2}\right|h\right)}\cos\left(\psi_1-\psi_2\right) \\ & + \frac{a_1 a_2\sigma_{I,2}^2}{2}\left(\lambda+1\right)A_{(+)}\frac{\cosh\left[\left|\overrightarrow{k_1}+\overrightarrow{k_2}\right|(h+z)\right]}{\cosh\left(\left|\overrightarrow{k_1}+\overrightarrow{k_2}\right|h\right)}\cos\left(\psi_1+\psi_2\right) \end{aligned} \tag{A.9}$$

A.2 PMM solutions

Wave induced particle velocity along *x*-axis:

$$u_3 = \frac{a_3 g}{\sigma_{I,3}} e^{k_3(z+f_k)} \left[\left(k_{x,3} + \mathbb{R}_{u,c} \right) \cos \widetilde{\psi}_3 + \mathbb{R}_{u,s} \sin \widetilde{\psi}_3 \right] \tag{A.10}$$

where,

$$\mathbb{R}_{u,c} = -a_1 k_{x,1} k_3 B_{esum} \cos \psi_1 \tag{A.11}$$

$$\mathbb{R}_{u,s} = -a_1 k_{x,1} k_3 B_{e\min} \sin \psi_1 \tag{A.12}$$

$$B_{esum} = B_{(-)} e^{(\left|\overline{k}_3 - \overline{k}_1\right| - k_3)z} + B_{(+)} e^{(\left|\overline{k}_3 + \overline{k}_1\right| - k_3)z} \tag{A.13}$$

$$B_{e\min} = B_{(-)} e^{(\left|\overline{k}_3 - \overline{k}_1\right| - k_3)z} - B_{(+)} e^{(\left|\overline{k}_3 + \overline{k}_1\right| - k_3)z} \tag{A.14}$$

Wave induced particle velocity along *y*-axis:

$$v_3 = \frac{a_3 g}{\sigma_{I,3}} e^{k_3(z+f_k)} \left[\left(k_{y,3} + \mathbb{R}_{v,c} \right) \cos \widetilde{\psi}_3 + \mathbb{R}_{v,s} \sin \widetilde{\psi}_3 \right] \tag{A.15}$$

where,

$$\mathbb{R}_{v,c} = -a_1 k_{y,1} k_3 B_{esum} \cos \psi_1 \tag{A.16}$$

$$\mathbb{R}_{v,s} = -a_1 k_{y,1} k_3 B_{e\min} \sin \psi_1 \tag{A.17}$$

Wave induced dynamic pressure:

$$\frac{p_3}{\rho g} = a_3 e^{k_3(z+f_k)} \left[\left(1 + \mathbb{R}_{p,c} \right) \cos \widetilde{\psi}_3 + \mathbb{R}_{p,s} \sin \widetilde{\psi}_3 \right] \tag{A.18}$$

where,

$$\mathbb{R}_{p,c} = -a_1 k_3 \lambda \left(B_{esum} + \Gamma \frac{\cosh\left[k_1(h+z)\right]}{\sinh(k_1 h)} \right) \cos\psi_1 \tag{A.19}$$

$$\mathbb{R}_{p,s} = -a_1 k_3 \lambda \left(B_{e\min} + \frac{\sinh\left[k_1(h+z)\right]}{\sinh(k_1 h)} \right) \sin\psi_1 \tag{A.20}$$

APPENDIX B

SOLUTIONS FOR A DIRECTIONAL WAVE FIELD

Depend on their locations in the frequency domain, the MCM or PMM solutions are chosen for the interaction between two free wave components. As sketched in Figure 2.1, a spectrum can be divided into six or more bands in the frequency domain. Only the wave components located in band *L1*, *L2*, *S1* and *S2* are considered. For convenient desperations, their interactions can be classified into five groups.

L1+L2: Interactions among all the components in band *L1* and *L2*;
S1+S2: Interactions among all the components in band *S1* and *S2*;
L2+S1: Interactions among all the components in band *L2* and *S1*;
L1~S1: Interactions among all the components in band *L1* and those in band *S1*;
(L1+L2)~S2: Interactions among all the components in band *L1+L2* and those in band *S2*.

The MCM solutions are chosen for the first three groups and the PMM solutions for the last two groups.

The solutions of velocity potential and elevation for the groups *(L1+L2)*, *(S1+S2)* and *(L2+S1)* are:

$$\begin{aligned}\phi = &\sum_{j=N_0}^{N_1}\left\{\frac{a_j g}{\sigma_{I,j}}\frac{\cosh\left[k_j(h+z)\right]}{\cosh\left(k_j h\right)}\sin\psi_j + \frac{3}{8}\frac{a_j^2\sigma_{I,j}\cosh\left[2k_j(h+z)\right]}{\sinh^4\left(k_j h\right)}\sin 2\psi_j\right\}\\ &+\sum_{j=N_0}^{N_1-1}\sum_{i=j+1}^{N_1}\frac{a_i a_j \sigma_{I,i}}{2}A_{j,i(-)}\frac{\cosh\left[\left|\vec{k}_j-\vec{k}_i\right|(h+z)\right]}{\cosh\left[\left|\vec{k}_j-\vec{k}_i\right|h\right]}\sin(\psi_j-\psi_i)\\ &+\sum_{j=N_0}^{N_1-1}\sum_{i=j+1}^{N_1}\frac{a_i a_j \sigma_{I,i}}{2}A_{j,i(+)}\frac{\cosh\left[\left|\vec{k}_j+\vec{k}_i\right|(h+z)\right]}{\cosh\left[\left|\vec{k}_j+\vec{k}_i\right|h\right]}\sin(\psi_j+\psi_i)\end{aligned} \qquad \text{(B.1)}$$

where,

$$A_{j,i(\mp)} = \mp \frac{k_i \left[2\lambda_{j,i} \left(1 \mp \lambda_{j,i}\right)\left(\Gamma \alpha_j \alpha_i \pm 1\right) \mp \lambda_{j,i}^3 \left(\alpha_j^2 - 1\right) + \alpha_i^2 - 1 \right]}{k_i \left(1 \mp \lambda_{j,i}\right)^2 - \alpha_2 \left| \overrightarrow{k_j} \mp \overrightarrow{k_i} \right| \tanh\left(\left| \overrightarrow{k_j} \mp \overrightarrow{k_i} \right| h \right)} \tag{B.2}$$

$$\lambda_{j,i} = \sigma_{I,j} / \sigma_{I,i} \tag{B.3}$$

$$\begin{aligned} \eta = & \sum_{j=N_0}^{N_1} \left\{ a_j \cos\theta_j + \frac{a_j^2 \sigma_j^2}{4g} \left[2 + \frac{3\cosh(2k_j h)}{\sinh^4(k_j h)} - \frac{1}{\sinh^2(k_j h)} \right] \cos 2\psi_j \right\} \\ & + \sum_{j=N_0}^{N_0-1} \sum_{i=N_0+1}^{N_0} \frac{a_i a_j k_i}{2\alpha_i} \left[-\left(1 - \lambda_{j,i}\right) A_{j,i(-)} + M_{j,i(-)} \right] \cos\left(\psi_j - \psi_i\right) \\ & + \sum_{j=N_0}^{N_0-1} \sum_{i=N_0+1}^{N_0} \frac{a_i a_j k_i}{2\alpha_i} \left[\left(1 + \lambda_{j,i}\right) A_{j,i(+)} + M_{j,i(+)} \right] \cos\left(\psi_j + \psi_i\right) \end{aligned} \tag{B.4}$$

where,

$$M_{j,i(\mp)} = \lambda_{j,i}^2 + 1 - \lambda_{j,i} \left(\Gamma_{j,i} \alpha_j \alpha_i \pm 1 \right) \tag{B.5}$$

$$\Gamma_{j,i} = \cos\left(\theta_j - \theta_i\right) \tag{B.6}$$

N_0 and N_1 are the index of the first and last free wave components in the corresponding group, respectively.

The PMM solutions of velocity potential and elevation for the groups (*L1~S2)* and *((L1+L2)~S2)* are:

$$\phi = \sum_{j=M_0}^{M_1} \frac{a_j g}{\sigma_{I,j}} e^{k_j \left(z + f_{k,j}\right)} \sin\left(\psi_j + k_j f_{\psi,\phi,j}\right) \tag{B.7}$$

$$\eta = \sum_{j=M_0}^{M_1} a_j \left(1+ f_{a,j}\right)\cos\left(\psi_j + k_j f_{\psi,\eta,j}\right) \tag{B.8}$$

where,

$$f_{k,j} = \sum_{i=N_0}^{N_1} a_i \left[B_{j,i(-)} e^{\left(\left|\bar{k}_j - \bar{k}_i\right| - k_j\right)z} - B_{j,i(+)} e^{\left(\left|\bar{k}_j + \bar{k}_i\right| - k_j\right)z} \right] \cos\psi_i \tag{B.9}$$

$$f_{\psi,\phi,j} = -\sum_{i=N_0}^{N_1} a_i \left[B_{j,i(-)} e^{\left(\left|\bar{k}_j - \bar{k}_i\right| - k_j\right)z} + B_{j,i(+)} e^{\left(\left|\bar{k}_j + \bar{k}_i\right| - k_j\right)z} \right] \sin\psi_i \tag{B.10}$$

$$f_{\psi,\eta,j} = -\sum_{i=N_0}^{N_1} a_i \left[\left(B_{j,i(-)} + B_{j,i(+)}\right) - \lambda_{i,j}\left(B_{j,i(-)} - B_{j,i(+)}\right) - \lambda_{i,j} \right] \sin\psi_i \tag{B.11}$$

$$f_{a,j} = k_j \sum_{i=N_0}^{N_1} a_i \left[\left(B_{j,i(-)} - B_{j,i(+)}\right) - \lambda_{i,j}\left(B_{j,i(-)} + B_{j,i(+)}\right) - \lambda_{i,j}\alpha_i \Gamma_{j,i} + \lambda_{i,j}^2 + 1 \right] \cos\psi_i \tag{B.12}$$

$$B_{j,i(-)} = \frac{\lambda_{i,j}\left(1-\lambda_{i,j}\right)\left(1+\alpha_i\Gamma_{i,j}\right) - \frac{\lambda_{i,j}^3}{2}\left(\alpha_i^2 - 1\right)}{\left(1-\lambda_{i,j}\right)^2 - \sqrt{1 - 2\lambda_{i,j}^2\Gamma_{i,j}\alpha_i + \lambda_{i,j}^4\alpha_i^2}} \tag{B.13}$$

$$B_{j,i(+)} = \frac{\lambda_{i,j}\left(1+\lambda_{i,j}\right)\left(1-\alpha_i\Gamma_{i,j}\right) - \frac{\lambda_{i,j}^3}{2}\left(\alpha_i^2 - 1\right)}{\left(1+\lambda_{i,j}\right)^2 - \sqrt{1 + 2\lambda_{i,j}^2\Gamma_{i,j}\alpha_i + \lambda_{i,j}^4\alpha_i^2}} \tag{B.14}$$

M_0 and M_1 are the index of the first and last free wave components in short wave band *S1* or *S2*, respectively. N_0 and N_1 are the index of the first and last free wave components in band *L1* or *L1+L2*, respectively.

Add the solutions in each group together, the solutions for a directional wave field can be obtained.

VITA

Shaosong Zhang was born in Zhenjiang, China. He received his B.S. in port, coastal and offshore engineering and engineering management from Tianjin University in 1998 and his M.S. in port, coastal and offshore engineering from Tianjin University in 2001. He entered the Ocean Engineering Program, Civil Engineering Department of Texas A&M University in September, 2001 and received his Ph.D. in Civil Engineering in December, 2005. During his PhD study, he had three journal papers published:

Zhang, J., S. Zhang, and Z. Wang, 2004: Analysis of WACSIS Data Using A Directional Hybrid Wave Model, *Journal of OMAE,* 2004, 126: 60-65

Zhang, S. and J. Zhang, 2004: Analysis of Directional Wave Fields with Strong Current, *Applied Ocean Research*, 2004, 26: 13-22

Zhang, S. and J. Zhang, 2004: A New Approach to Estimate Directional Spreading Parameters Based on a Cosine-2s Model, *Journal of Atmospheric and Oceanic Technology*, in press

He can be reached at:

Department of Civil Engineering
c/o Dr. Jun Zhang
TAMU
College Station, TX 77840